Analysing depth-dependence of cross-shore mean-flow dynamics in the surf zone

Master thesis by
Kevin C.C.J. Neessen

November 2012

University of Twente
Water Engineering & Management

Deltares

Cover picture
Plunging breaker at Waimea Bay, Hawaii
Photography by downingsf
www.downingsf.com

Analysing depth-dependence of cross-shore mean-flow dynamics in the surf zone

---

Master thesis in Civil Engineering and Management

Supervised by
Department of Water Engineering and Management
Faculty of Engineering Technology
University of Twente

Thursday, 29 November 2012

Author
K.C.C.J. (Kevin) Neessen

Exam committee

Graduation supervisor:	dr. ir. J.S. (Jan) Ribberink	University of Twente
Daily supervisor Deltares:	dr. ir. J.J. (Jebbe) van der Werf	Deltares University of Twente
Daily supervisor UT:	ir. W.M. (Wouter) Kranenburg	University of Twente

Abstract

Although wave breaking is a dominant feature along most beaches in the world, knowledge on it is far from complete. In the future, better morphological predictions are required because of an increasing amount of ever larger projects and activities in the nearshore zone. To properly predict morphological change; one needs to understand its hydrodynamics first. The undertow and turbulent kinetic energy (TKE) are important features for sediment transport. Therefore, in this thesis we considered radiation stresses, wave forces, Reynolds stresses, and TKE. Radiation stress is by definition depth-integrated, but the process under consideration in this thesis is closely related to this radiation stress and since no other term exist is named depth-dependent radiation stress.

The objective of this thesis is to increase the understanding of mean-flow dynamics in the surf zone; to assess how well the wave-averaged Delft3D-model is able to simulate mean-flow dynamics; and to suggest possible improvements. To increase the understanding an analysis was carried out on data from Boers (2005), who performed detailed velocity measurements in a small-scale wave flume with breaking waves. Two cases are taken into consideration: Boers-1B which featured spilling breakers, and Boers-1C with weakly plunging breakers. Doubtful results results above wave trough level were found and therefore, we have only considered data below wave trough level. For the modelling, Delft3D-FLOW was coupled to both a phase-averaged (roller model) and phase-resolving (TRITON) wave-driver.

Depth-dependent radiation stress profiles in the Boers (2005) data set were found to be virtually uniform on most locations. Only in the bottom boundary layer (BBL) on the breaker bar deviations from the uniform profile were seen. The horizontal derivative of the depth-dependent radiation stress – known as depth-dependent wave forces – were also found to be mainly uniform. This suggests that wave forces are not very important for the undertow profile. Depth-dependent radiation stresses were better approximated by the depth-dependent analytical equation of Mellor (2008) (M08) than the depth-integrated radiation stress from Longuet-Higgens and Stewart (1964) divided over depth (the procedure of Delft3D-FLOW). Results from M08 resulted in good approximations throughout the wave flume. Since depth-dependence of M08 was negligible, the better approximations are a result of the separate consideration of radiation stresses above wave trough level (E_D), which is applied as a shear stress rather than being distributed over the water column. Because it is modelled as a shear stress, this component is important for the undertow profile and might improve modelling results. Differences in calculated wave forces were less pronounced and it was difficult to determine which equation performed best.

Wave Reynolds stresses were found above the BBL. The forcing due to Reynolds stresses was found to be of a comparable magnitude as wave forces above BBL, but had the opposite sign – the forcings thus work against one-another. In Delft3D-FLOW, wave Reynolds stresses are only considered inside the BBL. Analytically, wave Reynolds stress above BBL were approximated well by the equation of Zou, Bowen, and Hay (2006), which shows possibilities for implementation into Delft3D-FLOW. Inside the BBL, Reynolds stresses dominate the forcing of the flow over wave forces. In this area, the wave Reynolds stress is dominant.

While comparing the results of the data analysis to other research, it became clear that bathymetry affected the vertical profiles of some hydrodynamic processes. Using

a natural profile rather than a plane sloping bottom leads to a change of sign in wave Reynolds stresses and to differing magnitudes in negative wave forces and turbulent kinetic energy. Since for a plane sloping bottom wave Reynolds stresses do not change sign, this means forcings would amplify each other after breaking, rather than work against one-another.

While considering the model output of the roller model, errors related to wave forces were found that complicated analysis of the results. From both coupled model systems, wave force magnitude was found to be considerably lower than those extracted from measurements. From these small wave forces, one would expect an underestimation of setup levels, but this was not the case. On top of that, also roller forces were significantly smaller than those found in measurements. Although to be fair, roller forces from measurements were also mostly modelled.

Turbulent kinetic energy levels were modelled well on most locations and only just before the first breaker bar levels were overestimated by both models. The vertical profile was found to be more curved than the linear profiles found in measurements. This is thought to be related to an overestimation of turbulence production near the bottom and an underestimation of turbulence mixing.

Undertow profiles are best modelled by TRITON-FLOW, where problems were only found at the breaker bar with underestimated velocities in the lower water column for Boers-1B. Roller-FLOW overestimated undertow velocities on most locations, which is thought to be a result of a too large mass flux above wave trough. The curvature of the undertow profile at the breaker bar, was not successfully reproduced by either model. This is thought to be related to the underestimation of roller forces and the absence of the surface concentrated E_D-component. Despite this deficiency, TRITON-FLOW still gives acceptable results for near bed velocities, which are important for sediment transport. All in all, we can conclude that TRITON-FLOW performs better than Roller-FLOW, although the practicality might be limited because of the huge computational times; 4-5 hours compared to 10 minutes for Roller-FLOW.

Preface and acknowledgements

This master thesis was written as the very last assignment of my master Water Engineering and Management at the University of Twente, Enschede. The research presented in this master thesis was carried out at Deltares, Delft. The subject of this thesis was mean-flow dynamics in the surf zone.

This subject turned out to be a real challenge – something which I should have known, since Christensen, Walstra, and Emerat (2002) explicitly state in their paper: "... [surf zone] hydrodynamics is very complex and, therefore, a natural challenge to any researcher in hydrodynamics or fluid mechanics.". I took me quite some time before I understood the processes that were taking place in the surf zone and to get a grip on the complex interactions between them. Since everything is related, it is almost impossible to single out a single process. And even when vertically integrated, understanding the flow equations can be difficult at times. Without the help of my supervisors Jan, Jebbe, and Wouter I am sure I would not have gained the understanding of surf zone hydrodynamics I did now. A special thanks is reserved for my daily supervisor at Deltares Jebbe, who I kept from his work on plenty occasions with my bombardment of questions and discussions about all things related to nearshore processes (and non-work related stuff). Despite this, Jebbe never lost his enthusiasm for my thesis, and I thank him for that.

This thesis can be seen as a continuation of work done by two Deltares employees: Marien Boers and Ivo Wenneker. I would like to thank Marien for sharing his wonderful data set with me and for getting me started with the data; something which turned out to be more complicated than I had envisioned. I am also grateful to Ivo Wenneker who shared his model with me and introduced me into the wonderful – but frustrating – world of numerical modelling.

Last but not least, I thank my fellow graduate students for the good times during lunch, coffee breaks, drinks, and just during working hours.

Kevin Neessen
Delft, November 2012

Contents

Chapter 1

Introduction

This research focuses on the vertical profiles of surf zone hydrodynamics, and special attention is given to breaking waves, which dominate the hydrodynamic processes in the surf zone. In section 1.1, the context of this research is explained. The objective and research questions are discussed in section 1.2 and methodology and report outline can be found in section 1.3.

1.1 Context

Walking along most beaches in the world, one would see the breaking of waves. On a windless day waves tend to break gently – some times hardly noticeable – creating the relaxing sound associated with the beach. At times of storm, visually dramatic wave breaking takes place which is a potentially dangerous phenomenon for those in the sea and for activities near the coast. Although wave breaking is present along most beaches in the world and is both visually and physically a dominant feature of the nearshore zone, our knowledge about wave breaking and the related processes is far from complete (Svendsen, 2006). With an increasing amount of ever larger projects and activities in the nearshore zone, in the future there will be a need for better short- and long-term morphological predictions.

Morphological changes depend on sediment transport gradients which in some cases can be modelled fairly well, but in others are plainly wrong (Aagaard, Black, &

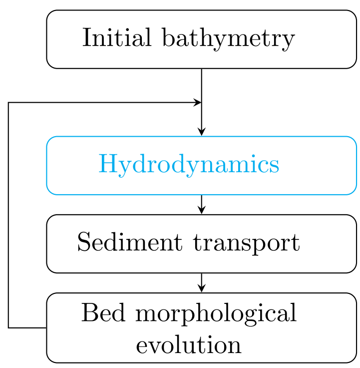

Figure 1.1: *The morphodynamic loop*

Greenwood, 2002). Sediment transport is in turn influenced by hydrodynamics which causes sediment movement in the surf zone to be "intense, chaotic and persistent combined with a delicate balance between fluid and sediment motion" (Kraus & Horikawa, 1990). Hydrodynamics are affected by bathymetry, which is changing because of morphological evolutions – and thus the morphodynamic loop is closed (figure 1.1). The initial bathymetry can be measured without too much effort after which it is vital to first properly understand hydrodynamics before one could wish to properly model other nearshore zone processes. It is these hydrodynamics – specified as the part affected or created by wave breaking – that are the subject of this thesis.

Modern coastal engineering relies heavily on the use of numerical models. One such numerical model often used by engineers is Delft3D by Deltares. Despite huge improvements over the last few decades, complex coastal environments are still difficult to model (Lesser, 2009) and especially accretive conditions remain problematic (Aagaard et al., 2002; Van Rijn, Tonnon, & Walstra, 2011). Knowledge on which these numerical models rely, is often gained from laboratory experiments in which detailed measurement data can be gathered under controlled conditions. This is especially true for surf zone hydrodynamics which are difficult to measure in the field because of fragile instruments, high-energy environment, and uncontrollable situations which lead to measurement uncertainties.

With the emergence of usable 3D-models, vertical profiles of different surf zone hydrodynamics become a point of interest and possibly model improvements. This thesis fits into the framework of SINBAD, a research project recently started by the universities of Twente, Liverpool and Aberdeen which aims to increase knowledge of the surf zone by conducting large-scale wave experiments.

1.2 Objective and research questions

Noting the above, we have formulated the objective of this thesis to be:

> *To increase the understanding of mean-flow dynamics in the surf zone and to assess how well the wave-averaged Delft3D-model is able to simulate mean-flow dynamics.*

Since in the end we are interested to not only improve hydrodynamics but also sediment transport and eventually morphodynamics, we have selected mean-flow processes that have large effects on (suspended) sediment transport; these are the undertow and turbulent kinetic energy. This thesis will look into the different components of the momentum equation (and thus those affecting the undertow profile) and determine the vertical profiles of depth-dependent radiation stress, depth-dependent wave forces, Reynolds stresses, and turbulent kinetic energy (TKE). Based on the objective, a number of research questions were formulated which will be answered in their respective chapters. They are as follows:

1. What are the physical processes governing cross-shore mean-flow dynamics in the surf zone and what are the assumed vertical profiles of the RANS-components in literature?
2. What are the vertical profiles of depth-dependent radiation stresses, wave forces, Reynolds stresses, and turbulent kinetic energy in the Boers (2005) data, and how important are the forcing components for the mean-flow?

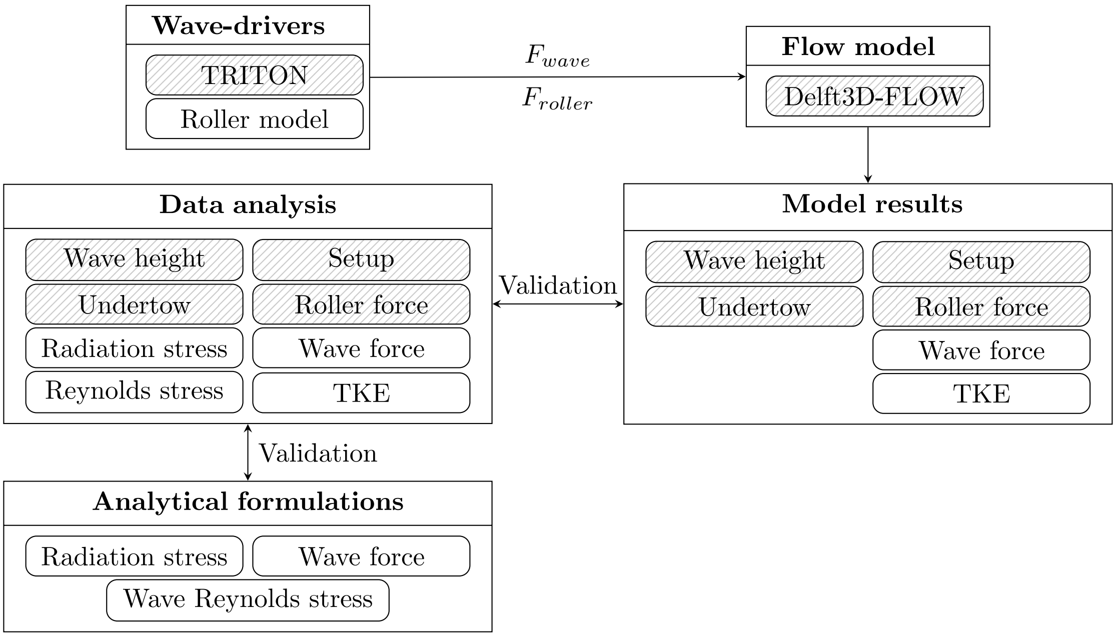

Figure 1.2: *Marked areas represent previous research carried out by Boers (2005) (data analysis) and Wenneker et al. (2011) (modelling and validation). Unmarked areas show new additions from this research.*

3. How well are depth-dependent radiation stresses, wave forces, and wave Reynolds stresses represented by analytical equations?
4. How is mean-flow dynamics in the surf zone modelled in a coupled system of wave-driver and Delft3D-FLOW?
5. How well is mean-flow dynamics in the surf zone modelled by Delft3D and what are the differences when a phase-averaged or phase-resolving wave driver is used?

1.3 Methodology and outline

This thesis continues on previous research, notably that of Boers (2005) and Wenneker et al. (2011). Increasing the understanding of mean-flow dynamics in the surf zone is achieved with an analysis of laboratory data from Boers (1996, 2005) who – among other things – carried out detailed flow velocity measurements in a wave flume. Since this wave flume data has no alongshore dimension, only the cross-shore dimension of mean-flow dynamics will be considered in this thesis. The results of the data analysis can then also be used to assess the performance of Delft3D. Wenneker et al. (2011) used Boers' data sets and compared them with the results of a coupled system of a phase-resolving Boussinesq-wave model (TRITON) and a hydrostatic flow model (Delft3D-FLOW). Since the practical use of phase-resolving wave-drivers is limited because of high computational efforts, we would like to know if for mean-flow dynamics, phase-resolving wave-drivers are necessary to properly model the undertow. Therefore, the coupled system of Delft3D-FLOW and TRITON will be compared to the phase-averaged roller model coupled to Delft3D-FLOW. Getting insight into the gain of phase-resolving wave-drivers could possibly influence their future development. Figure 1.2 shows a schematic overview of this thesis (unmarked areas) and how it fits into previous research (marked areas). The methodology per research question is defined as follows:

1. *What are the physical processes governing cross-shore mean-flow dynamics in the surf zone and what are the assumed vertical profiles of the RANS-components in literature?*

   With a literature study the physical background of surf zone hydrodynamics is investigated. This will give insight into the relevant processes of the surf zone and how they are affected by breaking waves. Since breaking waves are a complicated subject, the breaking process itself is also taken into consideration. The chapter consists thus of two parts: the first part looks into the fundamental hydrodynamics to see what forcing terms drive and affect the undertow. The second part consists of a qualitative discussion of the breaking process itself in order to increase understanding of the surf zone and its processes. The results of this literature study are the expected vertical profiles for the different forcing terms. The first research question is answered in chapter 2.

2. *What are the vertical profiles of depth-dependent radiation stresses, wave forces, Reynolds stresses, and turbulent kinetic energy in the Boers (2005) data, and how important are the forcing components for the mean-flow?*

3. *How well are depth-dependent radiation stresses, wave forces, and wave Reynolds stresses represented by analytical equations?*

   Questions 2 and 3 are closely related and are therefore considered together, in chapter 3. In order to increase the understanding of actual vertical profiles of surf zone hydrodynamics, a data analysis is carried out on the laboratory experiments by Boers (1996, 2005). For turbulence, research into its vertical distribution has been carried out before, but for radiation stress and wave forces this is a relative new area that has hardly been explored until now. This data analysis should give a better and clear insight into the vertical profiles of surf zone hydrodynamics for both spilling and plunging breakers. Since there is no literature on vertical profiles of radiation stress and wave forces, measurements will be compared to analytical radiation stress equations. This should give insight into the performance of different equations and what differences are between depth-independent and fairly new depth-dependent radiation stress equations. Measured wave Reynolds stresses will also be compared to an analytical equation to see how well it performs. Results from the data analysis will be compared to assumed profiles from literature as determined in chapter 2.

4. *How is mean-flow dynamics in the surf zone modelled in a coupled system of wave-driver and Delft3D-FLOW?*

   Knowledge about modelling procedures carried out by Delft3D-FLOW is gained with a literature study. This knowledge will help to properly assess model results and find possible areas of improvement. To improve understanding of modelling procedures, research behind them is also considered so an insight is given into the limitations of the model. The review of the modelling formulations is found in chapter 4.

5. *How well is mean-flow dynamics in the surf zone modelled by Delft3D and what are the differences when a phase-averaged or phase-resolving wave driver is used?*

   A validation will give insight into how well Delft3D can reproduce the laboratory data on different hydrodynamic processes and identify problems. Wenneker et al. (2011) used the phase-resolving wave model TRITON which gives more information to Delft3D, but it is unknown if this is actually worth the extra computational efforts when talking about radiation stress, wave forces, turbulent kinetic energy and undertow. Comparing it to the much faster phase-averaged roller model will give this insight. Model validation and assessment is found in chapter 5.

The final chapter of this thesis, chapter 6, contains the discussions, final conclusions, and recommendations for future research.

Chapter 2

Physical background of surf zone hydrodynamics

This chapter is a literature study into the physics governing surf zone hydrodynamics. The objective is to get a better insight into surf zone hydrodynamics generally, and wave breaking and mean-flow dynamics especially. The first section (2.1) gives a short introduction into the nearshore zone which will be important for terminology use in the remainder of the thesis. A detailed description of the breaking process can be found in section 2.2, which is subdivided into breaker types (2.2.2), breaking sequence (2.2.3), surface roller (2.2.4), and breaker-induced turbulence (2.2.5). Section 2.3 takes a close look into the fundamental equations that govern surfzone hydrodynamics and mean-flow dynamics. Section 2.3.2 discusses the terms of the RANS-equation one by one. Conclusions are found in the final section (2.4) of this chapter.

2.1 Nearshore zone

Before the surf zone and breaking waves are explained in detail, it is useful to give a short overview of the nearshore zone to get a better feeling of the environment all the processes occur in. The nearshore zone (figures 2.1 and 2.2) is the area between the shoreline and an offshore limit that is mostly taken at the point where water depth is so large that the bed no longer has any influence on the waves (Svendsen, 2006). The nearshore zone itself can be divided into a number of zones, of which the boundaries are dynamic and will thus change with tide, waves, wind, etc. In the direction from offshore towards the shoreline, the shoaling zone is encountered first. From the offshore limit of the shoaling zone, deep water waves become shallow-water waves as they start to get influenced by the sea bed, or from another perspective, the bed is affected by the waves. As the water becomes ever more shallow, the waves start to shoal (increase in height) and refract (change of direction) (Holthuijsen, 2007). The waves will eventually break, ending the shoaling zone and marking the offshore limit of the breaker and surf zone. The breaking of waves can be defined as the transformation of the particle motion from irrotational to rotational, generating vorticity and turbulence in the process (Basco, 1985), this transformation is irreversible.

The breaker zone is sometimes part of, sometimes separate of the surf zone. The breaker zone is defined as the area where the different waves break, so the varying breaking points define the breaker zone. The reason for this varying breaking point is

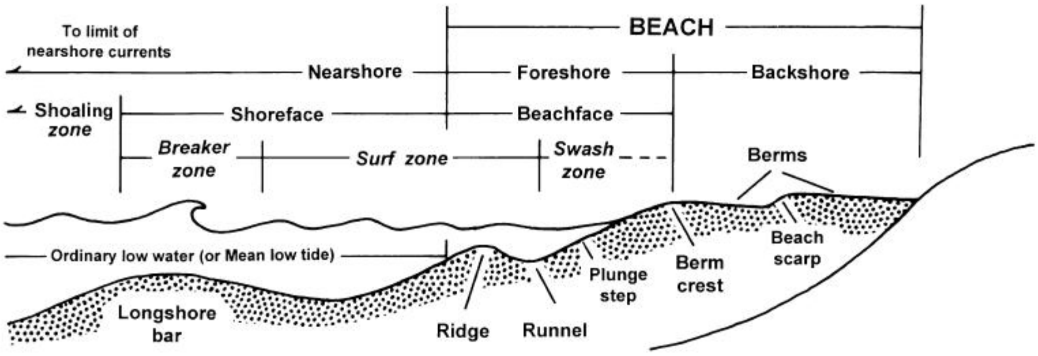

Figure 2.1: *Schematic view of nearshore zone with corresponding terminology, not to scale (Schwartz, 2005).*

that in reality there is a large spectrum of waves, that break on different locations. If all the waves are the same and conditions are static, there is one breaking point and thus a clear division between the shoaling and surf zones (Horikawa, 1988). In that case, the area of breaking can be included in the surf zone as the outer surf zone region (Svendsen, Madsen, & Buhr Hansen, 1978).

The surf zone is the region where waves break and breaking-induced processes dominate the fluid motion (Aagaard & Masselink, 1999). The surf zone is an area with dynamic and complex fluid and sediment motions because of the interactions between waves and currents. Furthermore, breaking waves cause great energy dissipation and are responsible for a number of hydrodynamic phenomena. An important one for both fluid and sediment processes is the undertow. Svendsen (1984a) defined the undertow as the net seaward oriented bottom current in the surf zone. The undertow is a reaction to the shoreward directed mass and momentum transport by breakers between wave trough and crest. The undertow is directed offshore and takes place below wave trough, the mass and momentum transport by breakers is (partly) balanced by the undertow. A distinction can be made between the inner and outer surf zone, which are defined as follows: the outer surf zone is the area where the wave shape rapidly transforms in a distance of several times the water depth (Svendsen et al., 1978). The inner surf zone is the area where the wave shape only changes slowly and a surface roller rides the front of the wave; distinctions between breaker types which are visible in the outer surf zone are no longer visible in the inner surf zone.

Shoreward of the surf zone is the swash zone. This area is relatively narrow and extends from the point of collapse of the wave or wave bore as it reaches the 'dry' beach up until the upper swash limit. The swash limit is determined not only by the wave, but also by percolation and steepness of the beach. The remaining water flows back down towards the sea, forming the backwash.

2.2 Breaking process

2.2.1 Onset of breaking

When waves enter the shoaling zone, they are affected by the bed and as a result the waves will increase in height. Because changes are slow, linear wave theory (LWT) can be applied without problems (until a certain shoreward limit and neglecting other

Figure 2.2: *Photograph of a nearshore zone with approximate boundaries between the different zones.*

processes like breaking).

During the approach of the shoreline, waves also change their shape. In deep water, waves are more or less sinusoidal, during their transformation they become ever more skewed and when the breaking point has almost been reached, vertical wave asymmetry occurs as well – this means the wave pitches forward (Grasmeijer, 2002). The breaking point is defined as the location where the wave front becomes vertical and the breaking process starts. Strictly speaking, LWT cannot be used in the surf zone since waves are no longer sinusoidal. However, approximations are still acceptable for some processes, like orbital velocities. Parametrisation and extension of LWT can increase usability even further, an example is the roller contribution as shown in Stive and Wind (1986).

2.2.2 Breaker type

Breaking waves can physically be classified into different types, something which can also be seen visually. The breaker types are part of a continuum and share a lot of the processes (see section 2.2.3), albeit on different spatial and time scales. The terminology for the classification of breakers was introduced by Galvin (1968), although the terms used had already been around for some decades. Galvin (1968) organized breakers into four different types (see figure 2.3) which for the same wave, would occur from almost flat to steep beaches in the following order: (i) spilling, (ii) plunging, (iii) collapsing, and (iv) surging. It is noted that in some sources (including recent ones, eg. Reeve, Chadwick, and Fleming (2004)), collapsing is not part of the classification, but seen as part of the continuum between plunging and surging. Collapsing and surging breakers do not develop a surface roller (Aagaard & Masselink, 1999) and hence no surf zone exists for these breaker types (Battjes, 1988). Therefore, collapsing and surging breakers are

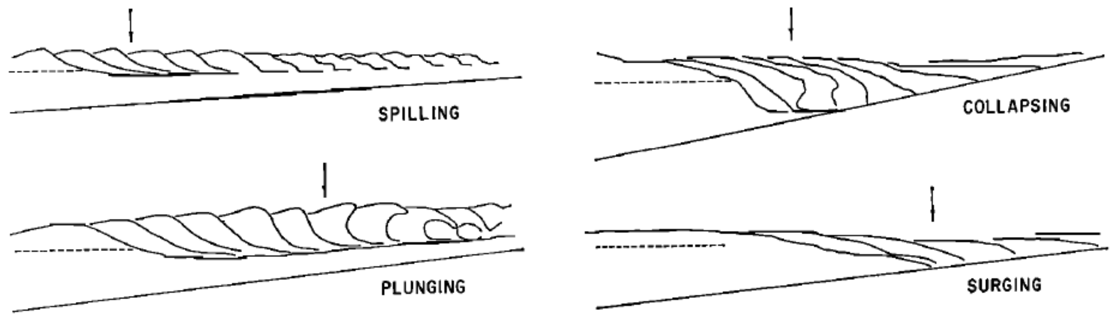

Figure 2.3: *Four breaker types by Galvin (1968)*

Table 2.1: *Surf similarity parameter for the different breaker types according to Battjes (1974)*

Type	**Surf similarity value**
Spilling	$\xi < 0.5$
Plunging	$0.5 < \xi < 3.3$
Collapsing / surging	$\xi > 3.3$

not part of this research and only spilling and plunging breakers are considered in the remainder of this thesis.

A spilling breaker develops when the wave crest becomes unstable and slides down the shoreward face of the wave. Turbulence is often confined to the upper region of the water column. Plunging breakers develop when the crest curls over the shoreward face and falls into the base of the wave, penetrating deeper into the water column than spilling breakers. Therefore, plunging breaker are more effective in suspending sediment than spilling breakers (Thornton, Galvin, Bub, & Richardson, 1976).

The type of breaker is determined by certain parameters: beach slope (β); wave height (H); and wave length (L) which have been combined into the surf similarity parameter (also known as the Iribarren number), which is shown in equation 2.1a (local) and equation 2.1b (deep water) (Battjes, 1974). Depending on which data is available, one can choose which equation to use. The classification with the surf similarity parameter is as shown in table 2.1.

$$\xi = \frac{\tan\beta}{\sqrt{H/L}} \tag{2.1a}$$

$$\xi_0 = \frac{\tan\beta}{\sqrt{H_0/L_0}} \tag{2.1b}$$

As discussed in section 2.1, the differences between spilling and plunging breakers are only seen at the breaking point and the so called outer surf zone. In the inner surf zone both types have developed into a turbulent bore and no longer show obvious differences (Battjes, 1988).

2.2.3 Breaking sequence

The breaking of a wave follows a certain sequence which is similar for both spilling and plunging breakers. In figure 2.4, ten different steps in the breaking sequence are shown for the plunger case (after Basco (1985)). The shore is located on the right and offshore is on the left. The main difference between the spilling and plunging cases is scale of the processes involved, the spilling breaker having the smallest of the two. For instance, the second image in figure 2.4 shows the overshooting of the wave top for a plunging breaker. For a spilling breaker it would not overshoot itself, but rather slide down the wave front, nevertheless the processes involved are the same. Note that this does not necessarily mean that local influences for spilling breakers are smaller. The processes for each of the images are (Basco, 1985; Battjes, 1988):

1. The wave pitches forward, becomes vertical and begins to break, the location where this occurs is known as the breaking point.
2. The wave top overshoots the wave body and plunges down, striking the preceding wave trough. The location where the jet hits the trough is known as the plunging point. From this point on, the fluid domain is doubly connected, leading to modelling difficulties.
3. The strike of the jet creates a splash.
4. The jet penetrates into the trough area and is deflected by the offshore directed flow. Combined with the forward motion of the wave crest, this creates a so called plunger vortex. The offshore directed flow is pushed upwards because of the jet and starts the development of the surface roller (section 2.2.4).
5. The air core compresses and the entrapped air mixes with the water. The air bubbles gradually rise to the surface.
6. A surface roller has developed at the front of the wave, this roller is similar to an hydraulic jump. The roller moves shoreward while the flow in the trough is still directed offshore.
7. The plunger vortex moves horizontally and pushes on the oncoming trough, creating a secondary wave disturbance. This increases the size and strength of the surface roller.
8. The toe of the roller slides down to its equilibrium position, growing in size and generating more vorticity as a result.
9. The plunger vortex loses speed and moves offshore relative to the wave.
10. The end of the outer surf zone is reached when the surface roller reaches its stable equilibrium position and the plunger vortex ceases to generate secondary disturbances. From hereon the inner surf zone is found in which the roller slowly loses energy and disappears or collapses on the beach.

2.2.4 Surface roller

Energy dissipated during the breaking process is generally assumed to be first converted into organised vortices (the surface roller) before being dissipated into small-scale, disorganised turbulent motions (Christensen et al., 2002). Taking the surface roller into consideration, leads to larger mass, momentum and energy fluxes compared to normal wave theory and leads to better predictions of nearshore zone processes (Basco, 1985). Svendsen (1984b) defines the surface roller as ‘the recirculating part of the flow above the dividing streamline (in a coordinate system following the wave)’ and is transported

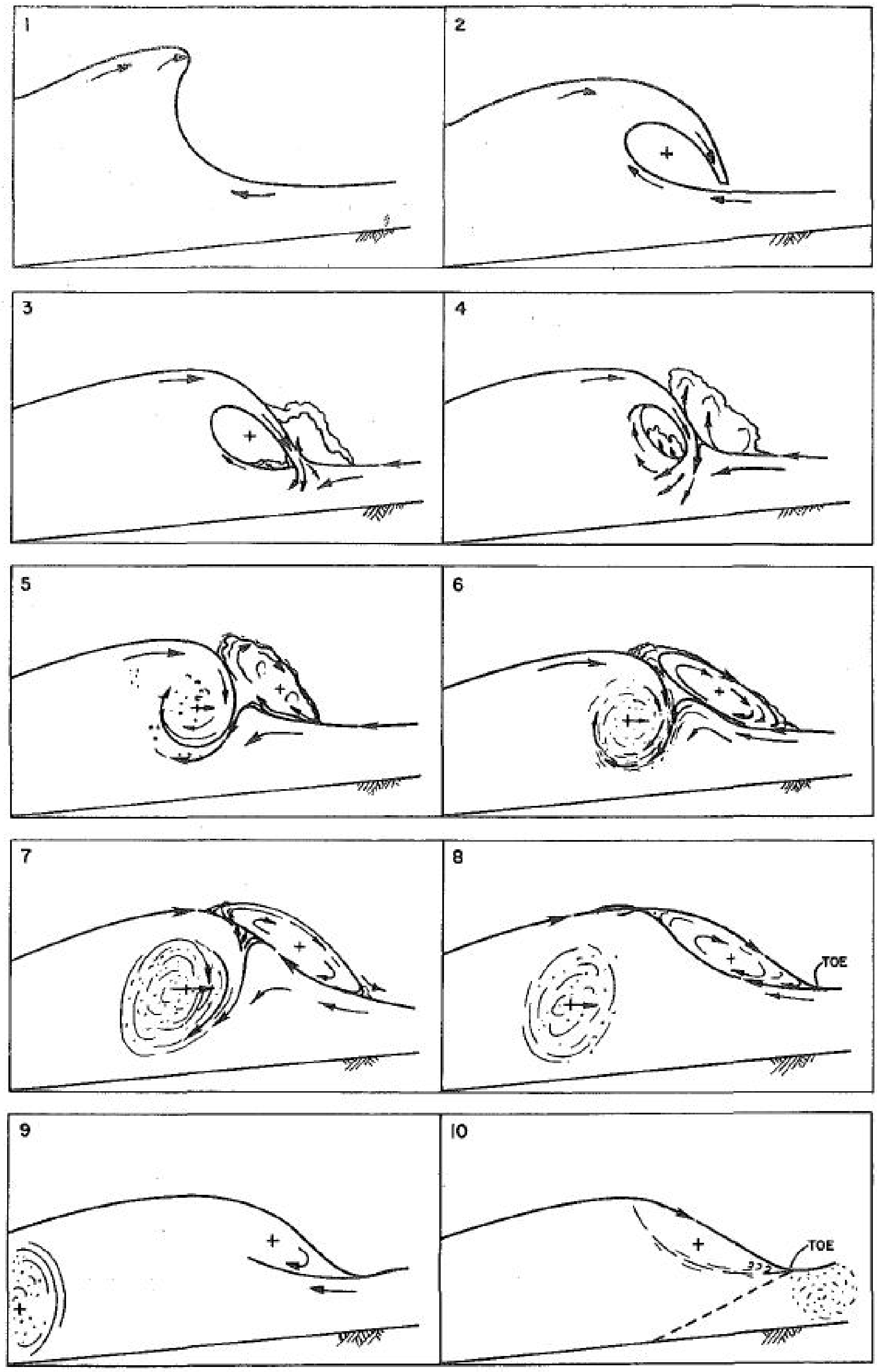

Figure 2.4: *Breaking sequence by Basco (1985)*

by the moving wave front. Theory assumes the surface roller to be comparable to a hydraulic jump.

Since extending the momentum equations to the area of the surface roller is problematic, Deigaard (1993) based the shear stress at the free water surface due to the roller (known as the roller force) on the mass and momentum balance for the surface roller. The effects of the surface roller are thus modelled, and not analytically solved. This model is included into Delft3D-FLOW as the roller model and is discussed in section 4.1.1.

2.2.5 Breaker-induced turbulence

Surf zone turbulence affects both fluid motions and sediment transport. Fluid motions like undertow are affected by turbulence through eddy viscosity (eddy viscosity is discussed in section 4.2.4). On sediment concentrations, the effect of turbulence is apparent as suspended sediment diffusivity, which increases suspended sediment concentrations in the water column (Boers, 2005). The largest contribution to turbulence in the surf zone is wave breaking (Yoon & Cox, 2010). This breaker generated turbulence is mostly located in the upper water column. Turbulence is also generated in the bottom boundary layer, but is an order of magnitude smaller than breaker generated turbulence (Svendsen, 1987). However, for sediment transport, turbulence in the lower water column could be more important since here suspended sediment concentrations are highest (Boers, 2005). Based on knowledge about turbulence production, Svendsen (1987) suggested and proved that turbulence levels decrease from the surface to the bottom, although this variation appeared to be rather small. The same conclusions were made by Ting and Kirby (1994, 1995, 1996). The limited variation is mostly the result of diffusion, as extensive tests by Ting and Kirby (1996) showed.

Ting and Kirby (1994, 1995, 1996) further proved that over a wave cycle, turbulence levels differ between spilling and plunging breakers. For spilling breakers, turbulence levels are almost constant over the wave period. For plunging breakers, high turbulence levels occur immediately after the wave breaks, at other areas turbulence production is low. This is important for suspended sediment transport that will travel with the undertow (ie. offshore) in the case of spilling breakers, and with the wave crest (ie. onshore) in case of plunging breakers (Christensen et al., 2002). In relation to orbital velocity, the timing of breaker-induced turbulence transported downwards reaching the bed, is also important. When it takes about half a wave-phase, the wave-related sediment transport will be directed offshore. If it takes one wave-phase, it will be directed onshore.

From Scott, Cox, Maddux, and Long (2005), it became clear that despite similar offshore conditions, turbulence levels for random waves are significantly lower than for regular waves. This is most likely the result of the wider breaker zone in which the random waves break. Their energy is thus dissipated over a larger volume and hence, turbulence levels are, on average, lower.

2.3 Fundamental hydrodynamics

2.3.1 Equation of motion

Hydrodynamics is based on three conservation principles: conservation of mass, momentum, and energy. Since there are more unknowns than number of equations some assumptions have to be made to find a solution (Arcilla, 1989). A fundamental assumption is that the fluid is a continuum, it can thus be divided into infinitesimally small particles. If further assumed that water is incompressible and both density and viscosity are constant – all are realistic assumptions for the nearshore zone (Svendsen, 2006) – we get the conservation of mass (also known as continuity equation) as shown in equation 2.2. The conservation of momentum – known as the momentum or Navier-Stokes equation – is based on Newton's second law. The equations are shown in equation 2.3a (x-direction), 2.3b (y-direction), and 2.3c (z-direction).

$$\frac{\partial u}{\partial x} + \frac{\partial v}{\partial y} + \frac{\partial w}{\partial z} = 0 \tag{2.2}$$

$$\overbrace{\rho\Big(\underbrace{\frac{\partial u}{\partial t}}_{\substack{\text{Unsteady}\\ \text{acceleration}}} + \underbrace{u\frac{\partial u}{\partial x} + v\frac{\partial u}{\partial y} + w\frac{\partial u}{\partial z}}_{\substack{\text{Convective}\\ \text{acceleration}}} \Big)}^{\text{Inertia (per volume)}} = \underbrace{\rho g_x}_{\substack{\text{Gravity}\\ \text{force}}} - \underbrace{\frac{\partial p}{\partial x}}_{\substack{\text{Pressure}\\ \text{gradient}}} + \underbrace{\mu \left(\frac{\partial^2 u}{\partial x^2} + \frac{\partial^2 u}{\partial y^2} + \frac{\partial^2 u}{\partial z^2} \right)}_{\text{Viscosity}} \tag{2.3a}$$

$$\rho\Big(\frac{\partial v}{\partial t} + u\frac{\partial v}{\partial x} + v\frac{\partial v}{\partial y} + w\frac{\partial v}{\partial z}\Big) = \rho g_y - \frac{\partial p}{\partial y} + \mu \left(\frac{\partial^2 v}{\partial x^2} + \frac{\partial^2 v}{\partial y^2} + \frac{\partial^2 v}{\partial z^2} \right) \tag{2.3b}$$

$$\rho\Big(\frac{\partial w}{\partial t} + u\frac{\partial w}{\partial x} + v\frac{\partial w}{\partial y} + w\frac{\partial w}{\partial z}\Big) = \rho g_z - \frac{\partial p}{\partial z} + \mu \left(\frac{\partial^2 w}{\partial x^2} + \frac{\partial^2 w}{\partial y^2} + \frac{\partial^2 w}{\partial z^2} \right) \tag{2.3c}$$

where ρ is density ($kg\ m^{-3}$); t is time (s); x is cross-shore direction (m); y is alongshore direction (m); z is vertical direction (m); u is cross-shore horizontal velocity (ms^{-1}); v is alongshore horizontal velocity (ms^{-1}); w is vertical velocity (ms^{-1}); g is gravitational acceleration (ms^{-2}); p is pressure (Nm^{-2}); and μ is dynamic viscosity (Nsm^{-2}).

To be able to describe turbulent flows, the NS-equation is combined with the continuity equation and the whole is phase-averaged (time-averaging over a wave phase, denoted by an overbar). Decomposing the flow into mean, orbital and turbulent components (a process known as Reynolds decomposition, see equation 2.4) will create the possibility of separate analysis of the components. What results, is the Reynolds-averaged Navier-Stokes (RANS) equation of which the derivation can be found in appendix A.

The mean flow ($\overline{u}$) and waves are assumed to be constant in time (ie. $\partial/\partial t = 0$) – so for instance no tide is present – and gravity is taken in the direction of the z-axis. Since this thesis considers measurements from a wave flume it can be reduced to 2DV (ie. $\partial/\partial y = 0$ and $v = 0$). This leads to the following equations, which correspond to Svendsen and Lorenz (1989):

$$(u, w, p) = (\overline{u} + \tilde{u} + u', \overline{w} + \tilde{w} + w', \overline{p} + \tilde{p} + p') \tag{2.4}$$

$$x: \frac{\partial}{\partial x}\left\{\rho\left(\overline{\overline{u}^2} + \overline{\tilde{u}^2} + \overline{u'^2}\right)\right\} + \frac{\partial}{\partial z}\left\{\rho\left(\overline{\overline{u}\overline{w}} + \overline{\tilde{u}\tilde{w}} + \overline{u'w'}\right)\right\} = -\frac{\partial \overline{p}}{\partial x} + \mu\left(\frac{\partial^2 \overline{u}}{\partial x^2} + \frac{\partial^2 \overline{u}}{\partial z^2}\right) \tag{2.5a}$$

$$z: \frac{\partial}{\partial x}\left\{\rho\left(\overline{\overline{w}\overline{u}} + \overline{\tilde{w}\tilde{u}} + \overline{w'u'}\right)\right\} + \frac{\partial}{\partial z}\left\{\rho\left(\overline{\overline{w}^2} + \overline{\tilde{w}^2} + \overline{w'^2}\right)\right\} = \rho g_z - \frac{\partial \overline{p}}{\partial z} + \mu\left(\frac{\partial^2 \overline{w}}{\partial x^2} + \frac{\partial^2 \overline{w}}{\partial z^2}\right) \tag{2.5b}$$

In equation 2.5a the x-derivatives represent the normal stresses and z-derivatives the shear stresses. Reorganizing equations 2.5a and 2.5b, results in:

$$\underbrace{\frac{\partial \rho \overline{u}^2}{\partial x}}_{(1)} + \underbrace{\frac{\partial \left(\rho \overline{\tilde{u}^2} + \rho \overline{u'^2} + \overline{p}\right)}{\partial x}}_{(2)} + \underbrace{\frac{\partial \rho \overline{u}\overline{w}}{\partial z}}_{(3)} + \underbrace{\frac{\partial \rho \overline{\tilde{u}\tilde{w}}}{\partial z}}_{(4)} + \underbrace{\frac{\partial \rho \overline{u'w'}}{\partial z}}_{(5)} = \underbrace{\mu \left(\frac{\partial^2 \overline{u}}{\partial x^2} + \frac{\partial^2 \overline{u}}{\partial z^2}\right)}_{(6)} \tag{2.6a}$$

$$\frac{\partial \rho \overline{w}^2}{\partial z} + \frac{\partial \left(\rho \overline{\tilde{w}^2} + \rho \overline{w'^2} + \overline{p}\right)}{\partial z} + \frac{\partial \rho \overline{u}\overline{w}}{\partial x} + \frac{\partial \rho \overline{\tilde{u}\tilde{w}}}{\partial x} + \frac{\partial \rho \overline{u'w'}}{\partial x} = \rho g_z + \mu \left(\frac{\partial^2 \overline{w}}{\partial x^2} + \frac{\partial^2 \overline{w}}{\partial z^2}\right) \tag{2.6b}$$

In equation 2.6a (only the x-direction is explained) some familiar components can be found, for instance: components one and two are horizontal fluxes of horizontal momentum by their respective velocity component. The inside of component two ($\rho\overline{\tilde{u}^2} + \rho\overline{u'^2} + \overline{p}$) will result in radiation stress when vertically integrated (see appendix B). Components three to five are vertical fluxes of horizontal momentum of which component five inside the derivative is known as the (turbulent) Reynolds stress ($\rho\overline{u'w'}$). Because of similarity, the third component is named mean-flow Reynolds stress ($\rho\overline{u}\overline{w}$); and fourth component is called the wave Reynolds stress ($\rho\overline{\tilde{u}\tilde{w}}$). These Reynolds stresses cause mixing of momentum. Component six represents viscosity. When gravitational acceleration is the most important vertical acceleration – which is the case with the shallow-water approximation – equation 2.6b changes to hydrostatic pressure.

2.3.2 RANS-components

Integrating equations 2.6a and 2.6b twice, leads to mean currents profiles for the surf zone. Since this integration will create new constants – which need new assumptions – this is not carried out in this thesis. Instead, the more generally applicable RANS-equation is considered directly and the terms two to five in equation 2.6a are researched in detail in the data analysis (chapter 3). The mean-flow (or current) terms can be seen as a result of the forcing by waves and to a lesser degree turbulence, one such wave-induced current is the undertow.

The vertical undertow profile is determined by gradients of radiation stress, pressure from the sloping mean water surface (setup/setdown, pressure term, equation 2.6a), vertical mixing (Reynolds stresses, equation 2.6a), and bottom friction. Bottom shear stress is not visible in the above equations. It originates as a boundary condition when equation 2.6a is vertically integrated (see appendix B).

Radiation stress and wave forcing

The second term in equation 2.6a is the forcing of the current by both wave and turbulent velocities. Combined with pressure this leads to wave forces. Wave forces are the derivatives of a concept known as radiation stress which is often used to determine wave-current interaction. Other concepts besides radiation stress exist (ie. vortex force), but these are not considered in this thesis.

The concept of radiation stress was introduced and expanded by Longuet-Higgens and Stewart (1960, 1961, 1962, 1964) and they defined it as “the excess flow of momentum due to the presence of the waves”. It should be noted that the term radiation

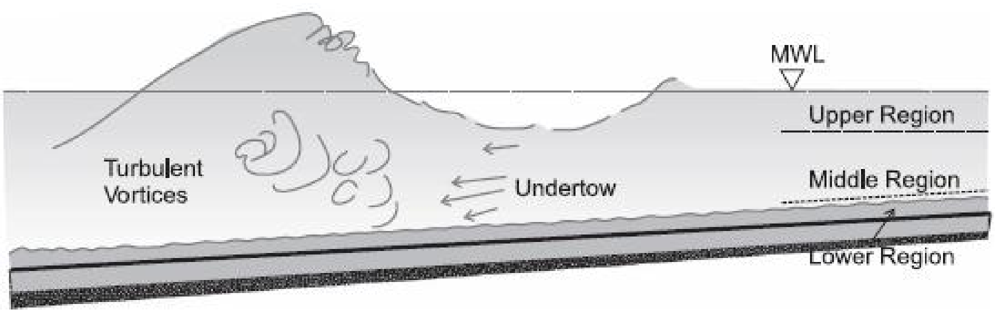

Figure 2.5: *Undertow and the vertical zones in cross-shore flow (Davidson-Arnott, 2010)*

stress is somewhat misleading since in reality it is not a stress (Nm^{-2}) but rather a stress times length (Nm^{-1}) (Sobey & Thieke, 1989). By definition radiation stress is depth-integrated, however, in this thesis we are interested in the vertical profile of this phenomenon. Since no specific definition exists for this depth-dependent phenomenon, we will name it depth-dependent radiation stress to signify the relationship between the concept as defined by Longuet-Higgens and Stewart (1960, 1961, 1962, 1964) and the phenomenon that will be studied in this thesis. This is in line with terminology used in, for instance, Kumar, Voulgaris, and Warner (2011) and Mellor (2012). Furthermore, in equations a capital S will be used to define depth-integrated radiation stress and a small case s is used to express depth-dependent radiation stress. This should avoid the confusion about the meaning of radiation stress that is present in other research.

The background of radiation stress lies in the depth-integrated and phase-averaged momentum equation. Understanding depth-integrated radiation stress helps with understanding depth-dependent radiation stress and therefore depth-integrated radiation stress is explained here. For clarity, only the horizontal momentum equation is considered. When equation 2.3a is vertically integrated (the procedure is shown in appendix B) we see the following result:

$$\begin{aligned}\rho\frac{\partial\overline{Q_x}}{\partial t}+\rho\frac{\partial}{\partial x}\left(\int_{-h_0}^{\zeta}\overline{u}^2\,\mathrm{d}z\right)+\frac{\partial S_{xx}}{\partial x}-\frac{\partial}{\partial x}\overline{\int_{-h_0}^{\zeta}\tau_{xx}\,\mathrm{d}z}+\rho\frac{\partial}{\partial x}\overline{\int_{\zeta_t}^{\zeta}2\overline{u}\tilde{u}\,\mathrm{d}z}=\\ -\rho gh\frac{\partial\overline{\zeta}}{\partial x}+\overline{R_x^s}-\overline{\tau_{b,x}}\end{aligned}\tag{2.7}$$

where Q_x is horizontal volume flux (m^3s^{-1}); h_0 is bed level (m); ζ is water level (m), where $\partial\overline{\zeta}/\partial x$ represents the change in mean water level (MWL) which is known as setup and setdown. Setup is defined as the increased MWL compared to still water level (SWL) which occurs inside the surf zone and setdown is the lowering of the mean water level and occurs outside the surf zone. τ_{xx} are the viscous stresses (Nm^{-2}); R_x^s are all the stresses at the free surface level, collectively defined as the free surface stress (Nm^{-2}); and $\tau_{b,x}$ is bottom shear stress (Nm^{-2}). S_{xx} is radiation stress (Nm^{-1}), which is defined as:

$$S_{xx}=\overline{\int_{-h_0}^{\zeta}\left(\rho\tilde{u}^2+p\right)\,\mathrm{d}z}-\frac{1}{2}\rho gh^2\tag{2.8}$$

Radiation stress thus consists of a pressure (p and $\frac{1}{2}\rho gh^2$) and wave component ($\rho\tilde{u}^2$) (Longuet-Higgens & Stewart, 1964).

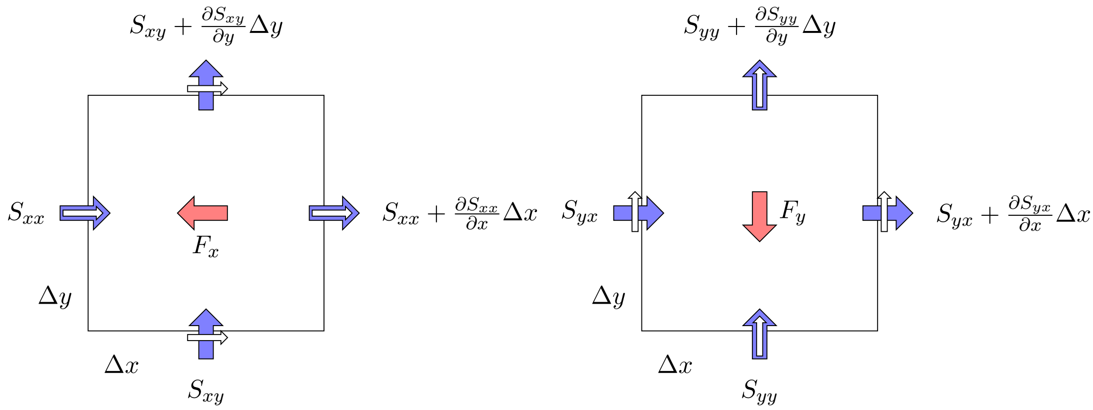

Figure 2.6: *Gradients of wave-induced x- (left) and y- (right) momentum transport S_{xx} and S_{yy} and resulting wave forces F_{xx} and F_{yy} (note the opposite sign of the wave forces compared to radiation stress). Blue arrows represent transport and white arrow represent wave-induced momentum (Holthuijsen, 2007).*

Radiation stress proved successful in explaining setdown, setup, longshore currents, and infragravity waves (Smith, 2006). However, radiation stress itself does not lead to a net force, for in a steady, uniform wave field with a horizontal bed, acting forces cancel each other out (figure 2.6). A net wave force only appears in spatially non-uniform situations with varying wave characteristics and/or water depth (Holthuijsen, 2007). It is thus the change of radiation stress that drives the flow and is of interest, this is already visible in equation 2.6a where the horizontal derivative of radiation stress appears. This radiation stress divergence is called wave force and is mathematically represented by equation 2.9 (cross-shore, horizontal direction only). It is important to note the minus sign, meaning that an increasing radiation stress (ie. positive gradient) in wave propagation direction leads to a negative wave force (ie. directed offshore) and vice versa.

$$F_{wave,xx} = -\frac{\partial S_{xx}}{\partial x} \tag{2.9}$$

When equation 2.7 is simplified for sake of clarity and understanding – net volume fluxes are zero; there is a steady state; wind stresses are assumed to be zero; the only shear stress at the surface is considered to be the roller force (as explained in section 2.2.4), so $\overline{R_x^s} = F_{roller,xx}$; and viscous stresses are assumed to be small – the equation simplifies to:

$$F_{wave,xx} + F_{roller,xx} = \rho g h \frac{\partial \overline{\zeta}}{\partial x} + \overline{\tau_{b,x}} \tag{2.10}$$

Equation 2.10 gives an understanding between the depth-integrated relationship of wave and roller forces on the one hand, and wave setup/setdown and bottom shear stress on the other. Note that the wave force can be both negative and positive, where the roller force is always positive (where positive means: directed shoreward). The bottom shear stress is often neglected since most of the times it is less than 5% of the wave force (Svendsen, 2006). The wave and roller forces are thus mainly compensated by the setup of the water level. This equilibrium between setup/setdown and wave/roller forces is visualised in figure 2.7, note that roller force and bed shear stress are not explicitly

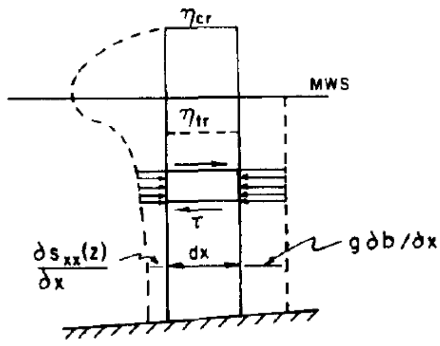

Figure 2.7: *Vertical distribution of radiation stresses and pressure gradients (Svendsen, 2006)*

visible. The roller force in the figure is the divergence of radiation stress above wave trough level and is applied on MWL (Svendsen, 2006), this is explained in section 4.2.3. Although an equilibrium exists on a depth-averaged basis, in figure 2.7 it can be seen there is a depth-dependent deviation for radiation stress, where pressure is uniform, this is an important source of the undertow (Nielsen, 1992).

Even though the depth-integrated equations by Longuet-Higgens and Stewart (1964) have been used successfully for almost five decades, recently with the development of 3D circulation models the interest in depth-dependent radiation stress has increased. A few examples of recent research include Xia, Xia, and Zhu (2004) and Mellor (2003, 2008). That this work is far from finished becomes clear when the results of these equations for certain conditions are reviewed as was done by Sheng and Liu (2011) and Bennis, Ardhuin, and Dumas (2011). Equations from Xia et al. (2004) show completely wrong results, where for Mellor (2008), Bennis et al. (2011) mainly reduced the problems to the poor approximation of the vertical flux of wave momentum. Problems seem to be less pronounced in the surf zone because of dominant dissipative processes (Bennis et al., 2011; Kumar et al., 2011). And despite the ongoing scientific debate, the equations by Mellor (2008) – and subsequently Mellor (2011) – have been successfully implemented in a number of numerical models (Haas & Warner, 2009; Wang & Shen, 2010; Kumar et al., 2011) and showed improvements over depth-integrated radiation stress (Sheng & Liu, 2011).

Despite the depth-dependent radiation stress formulation by Mellor (2008), in the surf zone the vertical profile of cross-shore radiation stress beneath wave trough level is still assumed to be virtually uniform over depth. It should however be noted that the equations by Mellor (2003, 2008) were formulated for ocean research and thus used linear wave theory. Depth-induced wave breaking is therefore not (fully) taken into consideration, and wave forces from measurements could show different vertical profiles. Although for other hydrodynamics, wave breaking tends to make vertical profiles more uniform because of heavy mixing.

Equation 2.4 separated the flow into three different components and in the process introduced turbulence. Real flows are almost always turbulent and this is especially true for the surf zone. Turbulence can be seen as the distortion round orbital flow, where orbital flow itself could be seen as an (organized) distortion around the mean flow. Turbulence is not always included in radiation stress, following Stive and Wind (1982), we consider turbulence to be part of radiation stress. Equation 2.8 will therefore be changed into:

$$S_{xx} = \overline{\int_{-h_0}^{\zeta} (\rho\tilde{u}^2 + \rho u'^2 + p)\ \mathrm{d}z} - \frac{1}{2}\rho g h^2 \tag{2.11}$$

Reynolds stresses

Components three to five in equation 2.6a showed the Reynolds stress, which transport horizontal momentum in the vertical and are therefore important for the undertow profile (Dyhr-Nielsen & Sørensen, 1970). Stive and Wind (1986) showed that the vertical profile of the combined shear stresses below wave trough is practically uniform. However, De Vriend and Kitou (1990) argued that the uw-terms have the largest impact between wave trough and crest, an area not measured by Stive and Wind (1986). The same will be true for this thesis, where data from the wave trough-crest area are disregarded, see section 3.2 for a full explanation.

With the decomposition of the flow, the Reynolds stress was also decomposed into three different stresses. These are the mean-flow, wave, and turbulence Reynolds stresses. From theory it is to be expected that $\bar{w} = 0$, otherwise water would leave or enter the system (field measurements could also be affected by partial tidal cycles etc. for which a non-zero $\bar{w}$ would appear). This also means the mean flow Reynolds stress ($\rho\overline{\bar{u}\bar{w}}$) should be zero.

For the wave Reynolds stress ($\rho\overline{\tilde{u}\tilde{w}}$), it used to be assumed that the terms $\tilde{u}$ and $\tilde{w}$ would be 90°out-of-phase, and hence wave Reynolds stresses would be zero (with the bottom boundary layer as an exception). This is true for periodic waves of permanent form, but Deigaard and Fredsøe (1989) and Rivero and Arcilla (1995) argued there are four different sources that lead to non-zero wave Reynolds stresses outside the bottom boundary layer: (i) sloping bottom; (ii) wave amplitude gradient; (iii) vorticity effects induced by viscosity near solid boundaries; and (iv) vorticity effects induced by depth-varying currents. All these features are important in the surf zone. This was later backed-up by field research (Zou et al., 2006). Equations formulated by Zou et al. (2006) for sloping-bottom, bottom-friction, and dissipation suggest wave Reynolds stresses to have a more or less uniform profile.

The turbulent Reynolds stress ($\rho\overline{u'w'}$) together with $\rho\overline{u'^2}$ and $\rho\overline{w'^2}$ cause the turbulence closure problem of the Navier-Stokes equation because there are always more unknowns than equations. In order to find an answer nonetheless, a closure model is needed (Svendsen, 2006), see section 2.3.2. However, from measurement data turbulent Reynolds stresses can be shown and are expected to have maximum values at water level because of wave breaking and then decrease towards the bottom (Ruessink, 2010), values are thought to increase again in the bottom boundary layer.

Viscosity

Component six in equation 2.6a is the viscosity term. Viscosity is the measure of internal fluid friction or, easily put: the resistance to deformation. In equation 2.6a, μ is the dynamic (molecular) viscosity, when divided by density (ρ), the result is kinematic viscosity (ν). In order to take the effects of turbulence into account, the concept of eddy viscosity (ν_t) is used (see section 4.2.4), thus solving the turbulence closure problem.

The resulting viscosity term becomes:

$$\frac{\partial}{\partial z}\left[(\nu+\nu_{t,v})\frac{\partial \bar{u}}{\partial z}\right]+\frac{\partial}{\partial x}\left[(\nu+\nu_{t,h})\frac{\partial \bar{u}}{\partial x}\right] \tag{2.12}$$

The order of magnitude for ν is about 10^{-6} and ν_t about 10^{-3}. Therefore, the molecular viscosity term is often neglected. Note that ν is a parameter linked to the fluid and is therefore the same everywhere, ν_t is dependent on the processes taking place at that location and therefore varies in both horizontal and vertical direction. Since eddy viscosity is anisotropic, a distinction is made between horizontal and vertical eddy viscosity (also see section 4.2.4).

2.4 Conclusions

This chapter looked into the physical background of surf zone hydrodynamics and, in the process, defined important terminology for use in the remainder of the thesis. The nearshore zone and its divisions were discussed briefly, in order to get a better feeling of the whole area. The nearshore zone can be split into a number of different sections, for which the boundaries are far from static and change in time and even from wave-to-wave. Moving from offshore towards the beach, the shoaling zone is encountered first, then the outer surf zone, inner surf zone and lastly the swash zone.

The breaking processes were discussed in detail, which showed that the division in different breaker types is somewhat arbitrary – but nevertheless useful for discussion purposes. Breaker types can be determined with the surf similarity parameter. The breaking sequence is qualitatively understood, although quantitatively this is not entirely the case. Surface rollers are an important feature of the surf zone and cause increased mass, momentum, and energy fluxes. Moreover, wave energy is first transferred to the surface roller, before it is dissipated into disorganized turbulent motions. Turbulence was discussed, and from previous research turbulent kinetic energy is thought to have a linear profile with a maximum at water level. Two areas of turbulence production can be distinguished: (i) the main producer is wave breaking, at water level; and (ii) bottom friction at the bottom of the water column.

The Navier-Stokes equation was phase-averaged and the terms in the resulting Reynolds-averaged Navier-Stokes equation form the basis of this thesis. The different terms in this equation that force the wave-induced current were explained one by one as previous research was discussed. Cross-shore wave and turbulence forcing – captured in the radiation stress concept – is expected to show a more or less vertical profile in the surf zone. However, research into its 3D nature is still ongoing and is far from complete. The decomposed Reynolds stresses are assumed to have different profiles, in shallow water above the bottom boundary layer they are thought to be: mean-flow Reynolds stress is assumed to be zero; the wave Reynolds stress is thought to have a more or less uniform profile; and turbulent Reynolds stresses are expected to have a linearly decreasing profile with its maximum at water level, decreasing while approaching the bed where values increase again due to bottom turbulence production. Also, for Reynolds stresses there is plenty to improve.

Chapter 3

Data analysis

This chapter describes the analysis that is carried out on the measurement data from the experiments of Boers (1996, 2005). The objectives of this chapter are:

1. to find out what the vertical profiles of depth-dependent radiation stresses, wave forces, Reynolds stresses, and turbulent kinetic energy are in the surf zone and what can be learned from them;

2. to assess how well depth-dependent radiation stresses, wave forces, and wave Reynolds stresses can be represented by analytical equations for possible model improvements.

The results of this chapter will also be used for the validation of Delft3D in chapter 5. It is noted that only wave-averaged values are considered, since Delft3D only uses wave-averaged quantities. First, the experimental equipment and set-up are briefly discussed in section 3.1, for full details please consult Boers (1996, 2005). Second, the data preparation for the analysis can be found in section 3.2. The data analysis starts with depth-dependent radiation stresses (section 3.3) and because depth-dependent radiation stresses are fairly new and research is still ongoing, measured depth-dependent radiation stress (section 3.3.1) will be compared to analytical formulations to see if they give better approximations (section 3.3.2). Wave forces are discussed in section 3.4 and Reynolds stresses in section 3.5. After all the components of the RANS-equation have been analysed, the importance of the different components is discussed in section 3.6. Turbulent kinetic energy profiles are discussed in 3.7. The chapter concludes with a summary of the conclusions in section 3.8.

3.1 Experimental equipment and set-up

The experiments were carried out in the Large Wave Flume of the Fluid Mechanics laboratory of the Delft University of Technology from March until October 1995 and were a scaled-down version of the LIP 11D-experiments from spring 1993. The wave flume was 40 m long, 0.80 m wide and 1.05 m deep. A fixed bottom profile was used, based on a profile present during LIP 11D-experiment 1B (Boers, 1996). LIP 11D-experiments used a mobile bed instead, and also featured sediment transport and morphodynamic data. The profile for Boers' measurements was made out of concrete and smoothed to reduce bed roughness. Since the bottom was fixed, the same profile was used for test Boers-1C which means the profile is not natural to the conditions of Boers-1C. Because

Table 3.1: *Differences between the three cases of Boers (2005)*

Case	Measured H_{m0} (m)	Measured T_p (s)	Surf similarity parameter (ξ)	Breaker type
1A	0.157	2.05	0.35	spilling
1B	0.206	2.03	0.31	spilling
1C	0.103	3.33	0.71	weakly plunging

of wave generation problems, the wave height for Boers-1B was scaled down an extra 8%, and are thus not a perfect representation of LIP 11D, either. The profile was based on a natural beach and included two breaker bars (the first around $x = 21\ m$ and the second around $x = 25\ m$) with a surf zone trough in between them (see figure D.1). The water level was 0.75 m above the wave flume bottom and water temperature varied between 20–23°C. Three cases were run with different wave parameter settings, which are shown in table 3.1. An irregular wave series was used, which was repeated eleven times so orbital and turbulent velocities could be extracted.

Measurements were carried out by several different instruments: wave gauges measured surface elevation (sampling frequency 20 Hz); laser-Doppler velocimeters measured flow velocities (100 Hz); shear stress plates measured bed shear stresses (20 Hz); electromagnetic flow meters measured flow velocities above the stress plates (20 Hz); and video cameras were used for analysis of roller formation etc. Measurement locations of the laser-Doppler velocimeters are shown in figure D.1.

For this thesis only Boers-1B and Boers-1C are considered, these are the same as used in Wenneker et al. (2011). Boers-1B has spilling breakers and is an erosive case where Boers-1C has weakly plunging breakers and features accretive wave conditions.

3.2 Data preparation

In accordance with section 2.3 and Boers (2005), the flow velocities are separated into three components: mean ($\bar{u}$), orbital ($\tilde{u}$) and turbulent (u'). The mean velocity is the time-averaged value of all the measurements (equation 3.1a), orbital velocity is the ensemble average, with the mean value subtracted (equation 3.1b) and the part that remains is classified as the turbulent velocity (equation 3.1c).

$$\bar{u} = \frac{\sum_{j=1}^{M} \sum_{i=1}^{N} u_{ij}}{MN} \tag{3.1a}$$

$$\tilde{u_i} = \frac{\sum_{j=1}^{M} u_{ij}}{M} - \bar{u} \tag{3.1b}$$

$$u'_{ij} = u_{ij} - \tilde{u_i} - \bar{u} \tag{3.1c}$$

where u is flow velocity (ms^{-1}); i is velocity measurement counter (-); j is wave series counter (-); M is the number of wave series in an experiment run (-); and N is the number of velocity measurements in a wave series (-). Besides ensemble averaging there are various other methods to determine orbital and turbulent velocities, however, according to Scott, Cox, Shin, and Clayton (2004) they give answers of the same order and, perhaps

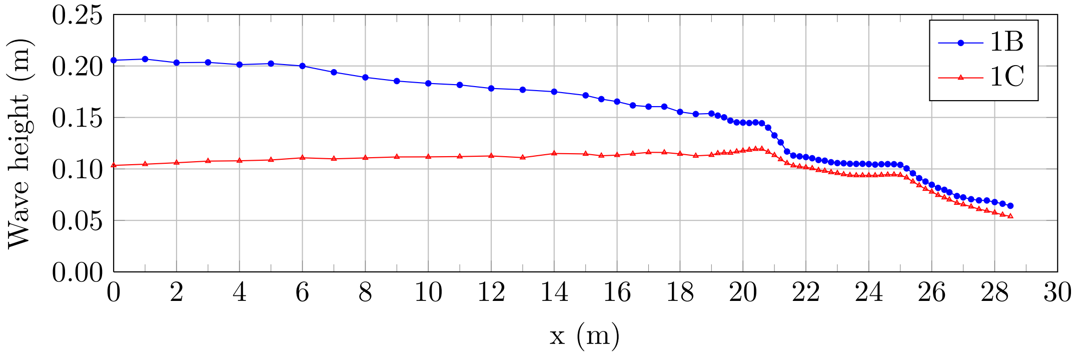

Figure 3.1: *Wave heights*

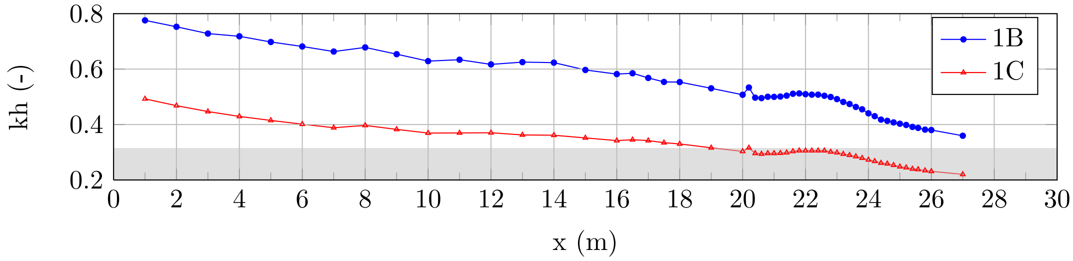

Figure 3.2: *Relative depth (kh) along the wave flume, shaded area represents locations where shallow water approximation is valid.*

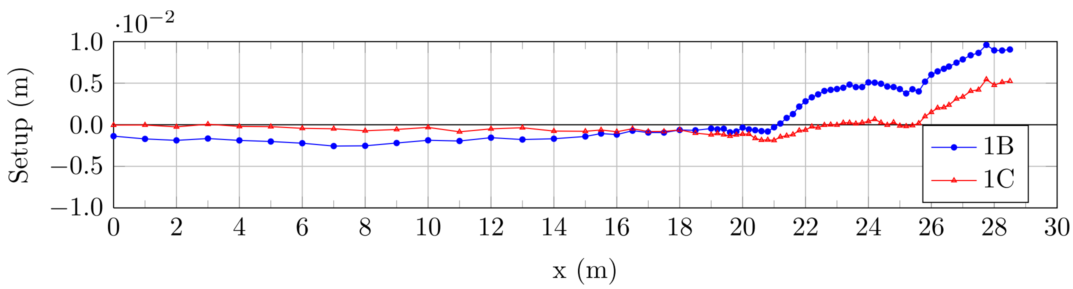

Figure 3.3: *Wave setup along the wave flume*

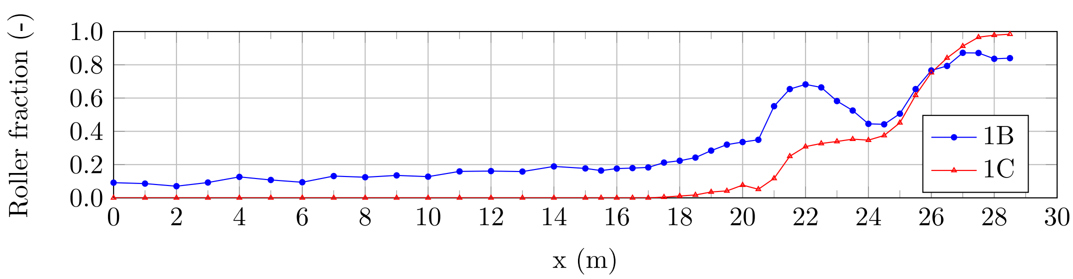

Figure 3.4: *Fraction of waves with roller*

more importantly for this thesis, the vertical profile is independent from the method used. We therefore stick with ensemble averaging as carried out by Boers (2005).

Ensemble averaging is only possible in laboratory environments and very useful for regular waves (Svendsen, 2006), Boers (2005) and Ting (2001) used it for irregular waves by repeating the exact same wave series multiple times. This is very time consuming and therefore the amount of wave series is rather small in Boers (2005), with a maximum of eleven, but because of measurement errors this is sometimes reduced to seven or eight. Govender, Mocke, and Alport (2002) showed that the computed velocity fluctuates significantly depending on the ensemble size, this is especially true for the higher regions of the water column. Ideally, a minimum of 20 series is used for the mean velocity and around 40 for turbulent velocities, similar values were found by Ting and Kirby (1994). The calculated ensemble averaged values are however in the right order of magnitude, but one needs to be aware of the larger margin of error.

To be able to compare results between different cases and locations and also other research, normalized depth (ξ) is used. Normalized depth is defined as $\xi = z/h$ in which z is real vertical position and h is mean water depth. This means that $\xi = 0$ at the bottom and $\xi = 1$ at the still water surface. Also the relative depth (kh) is calculated for all locations along the wave flume. This is done with the phase velocity as calculated by Boers (2005) and rewriting it with an adaptation of the dispersion relation:

$$kh = \tanh^{-1}\left(\frac{2\pi c}{gT}\right) \tag{3.2}$$

where c is measured phase velocity (ms^{-1}); g is gravitational acceleration (ms^{-2}); and T is wave period (s) for which the representative value is taken as measured by Boers (2005). Results are shown in figure 3.2 in which the shade represents the area for which the shallow water approximation is valid ($kh < 0.1\pi$). When for calculations specific values cannot be found in the figure, they are linearly interpolated.

During the measurements, some instruments were in between wave trough and crest or were greatly influenced by air bubbles generated by wave breaking. This led to questionable results for these areas high in the water column. To reduce the risk of dealing with corrupt data, only data below wave trough level is used; this was also concluded by Boers (2005). Because of irregular waves, this is done with the significant wave height from the spectrum (H_{m0}), which was calculated by Boers (1996). Half of this value is deduced from the mean water level to give the uppermost boundary for acceptable results. In figure D.1, measurement points above wave trough are disregarded.

3.3 Depth-dependent radiation stress

Both radiation stress and wave forces cannot be measured directly with existing techniques, but have to be deduced from other measurement data. Another difficulty arises because of the lack of good measurement data of wave-induced velocities between wave trough and crest, this has been discussed in the previous section.

There are roughly three different ways radiation stress can be calculated from measurement data (Torres-Freyermuth, Losada, & Lara, 2007): (i) use analytical and/or parametric results from constant-depth-wave theories; (ii) make estimations based on mean sea level spatial measurements; or (iii) make use of detailed velocity and free surface measurements. Only the third option gives insight into the vertical profile of radiation stress and since detailed measurements are available from Boers (2005) and the problem that arises – no measurements in the trough-crest area – is irrelevant since we are content with the vertical profile below trough level, this is the option used in this thesis. We opt for the procedure of Stive and Wind (1982), who rewrote the momentum balance (equation 2.3a) to calculate radiation stress from experimental data. We continue from equation 2.11, which is shown here again for clarity. The derivation of radiation stress itself is shown in appendix B:

$$S_{xx} = \overline{\int_{-h_0}^{\zeta} \left(\rho\tilde{u}^2 + \rho u'^2 + p\right) \mathrm{d}z} - \frac{1}{2}\rho g h^2 \tag{3.3}$$

First, the order of integration is interchanged to be able to use mean-flow properties and eventually discard the integral, leading for any flow property q to:

$$\overline{\int_{-h_0}^{\zeta} q \, \mathrm{d}z} = \int_{-h_0}^{\zeta_c} \overline{q} \, \mathrm{d}z \tag{3.4}$$

where ζ_c is the wave crest level (m); and the overbar denotes wave-averaging in time. Second, the terms denoting pressure in equation 3.4 are rewritten according to Svendsen (2006), which results in:

$$\int_{-h_0}^{\zeta_c} \overline{p} \, \mathrm{d}z - \frac{1}{2}\rho g h^2 = -\int_{-h_0}^{\zeta_c} \left(\rho\overline{\tilde{w}^2} + \rho\overline{w'^2}\right) \mathrm{d}z + \frac{1}{2}\rho g \overline{\left(\zeta - \overline{\zeta}\right)^2} \tag{3.5}$$

Next, we apply equations 3.4 and 3.5 to equation 3.3 and noting that the last term in equation 3.5 is the contribution due to wave setup; we get the following result (the radiation stress is named S_{xx}^{SW} after Stive and Wind (1982) in order to distinguish it from other types in the remainder of this thesis):

$$S_{xx}^{SW} = \int_{-h_0}^{\zeta_c} \left(\rho\overline{\tilde{u}^2} - \rho\overline{\tilde{w}^2} + \rho\overline{u'^2} - \rho\overline{w'^2}\right) \mathrm{d}z + \frac{1}{2}\rho g \overline{\eta^2} \tag{3.6}$$

where $\tilde{u}$ is horizontal orbital velocity (ms^{-1}); $\tilde{w}$ is vertical orbital velocity (ms^{-1}); u' is horizontal turbulent velocity (ms^{-1}); w' is vertical turbulent velocity (ms^{-1}); and ζ is water level (m). As discussed before, only the depth-dependent radiation stress below wave trough is considered. To determine the depth-dependent radiation stress below wave trough, one would simply ignore the integral in equation 3.6 and since the pressure due to setup is (nearly) uniform over depth (Nielsen, 1992), it is divided by the water depth. This leads to the following equation for depth-dependent radiation stress that is used for the analysis:

$$s_{xx}^{SW} = \underbrace{\rho\overline{\tilde{u}^2} - \rho\overline{\tilde{w}^2}}_{\textit{wave part}} + \underbrace{\rho\overline{u'^2} - \rho\overline{w'^2}}_{\textit{turbulence part}} + \underbrace{\frac{1}{2h}\rho g \overline{\eta^2}}_{\textit{setup part}} \tag{3.7}$$

In equation 3.7 a lower case s is used to make a distinction between the depth-integrated radiation stress S_{xx} in equation 3.6 and the depth-dependent one s_{xx}, this was discussed in section 2.3.2. Furthermore, it is repeated from section 2.3.2 that the unit of depth-integrated radiation stress is Nm^{-1} and of depth-dependent radiation stress Nm^{-2}. From equation 3.7 it becomes obvious that when $\tilde{u} = \tilde{w}$ – which is the case in deep water (sinusoidal waves) where no breaking/whitecapping occurs – the wave part of depth-dependent radiation stress would be zero below wave trough. Turbulence and wave setup levels for non-breaking waves are also small or non-existent and thus radiation stresses would be zero. However, in shallow water where orbital motions no longer form a circular path but are elongated in the horizontal direction, and wave breaking produces large amounts of turbulence and an increasing mean water level: depth-dependent radiation stresses appear over the whole vertical.

Since the experiment used irregular waves, the determination of radiation stress is carried out over the whole wave series. It would in theory be possible to calculate radiation stress for every single wave in the series – a process which is also carried out by TRITON – but this would unnecessarily complicate matters since Delft3D would also only produce radiation stress over the whole series.

3.3.1 Measured depth-dependent radiation stress and analysis

In figures 3.5 and 3.6 depth-dependent radiation stresses below wave trough (s_{xx}) are shown for both Boers-1B (spilling) and Boers-1C (weakly plunging). Details in the bottom boundary layer can be seen in figure D.2 and D.3. For most locations, depth-dependent radiation stress profiles are fairly uniform, although for Boers-1B close to the first breaker bar ($x = 20 - 22\ m$) a 'belly-profile' can be seen. The magnitude increases in the shoaling zone and is largest around the first breaker bar and decreases again in the surf zone trough; towards the second breaker bar it increases once more. The increase is mostly due to the horizontal wave component (figures 3.7 and 3.8). This pattern is in line with linear wave theory in which the orbital velocity amplitude increases with increasing wave amplitude (shoaling) and decreasing relative depth (kh) (Svendsen, 2006), both of which occur near the breaker bars.

Figures 3.7 and 3.8 show the contributions of the different velocity components, the setup component is not shown since we have assumed it to be depth-uniform. In both the spilling and the plunging cases, the horizontal wave component ($\rho\overline{\tilde{u}^2}$) is dominant on all locations. The vertical wave component ($\rho\overline{\tilde{w}^2}$) increases in significance in the higher water column, which is to be expected as close to the bed $\tilde{w}$ needs to be zero and increases as it gets closer to the surface. For discussion about turbulence, please see section 3.7. The order of magnitude for the different components is the same as in Stive and Wind (1982), who analyse laboratory experiments with similar wave conditions as Boers (2005).

In figures 3.9 and 3.10 the relative sizes of three components to the horizontal wave contribution are shown for all locations (so, ie. $\rho\overline{u'^2}\left(\rho\overline{\tilde{u}^2}\right)^{-1} \cdot 100\%$). The maximum relative size for Boers-1B is around 30% and is reached by the vertical wave component, although most of the times this value is significantly lower than that. From this we can conclude that the horizontal wave component ($\rho\overline{\tilde{u}^2}$) is dominant on all locations. The turbulence components increase in significance just after the first breaker bar in the higher part of the water column but because of the correlation between the horizontal and vertical turbulence terms (see figures 3.7b and 3.7d) and the fact that they have opposite signs (equation 3.7) causes them to largely cancel each other out. In Boers-1C (figure 3.10) the maximum relative size of the components is around 20%. As for Boers-1B, the relative size of turbulent components increases after the first breaker bar, but now also at the second, although this is difficult to see in the figure. The horizontal turbulence is also about twice the size of the vertical turbulence. This however does not

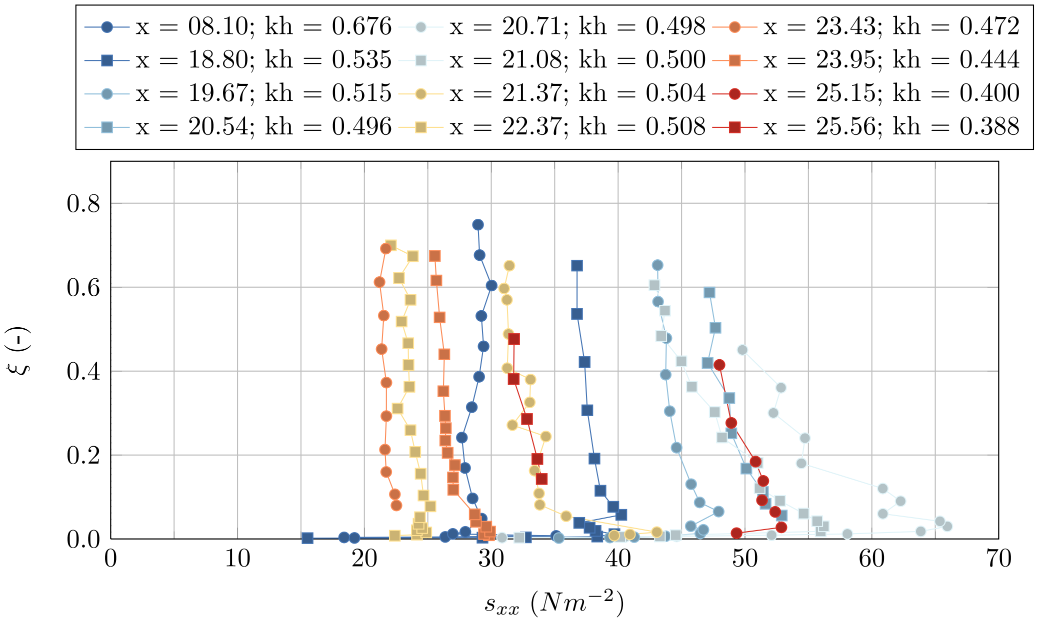

Figure 3.5: *Vertical radiation stress profiles for Boers-1B, spilling breakers*

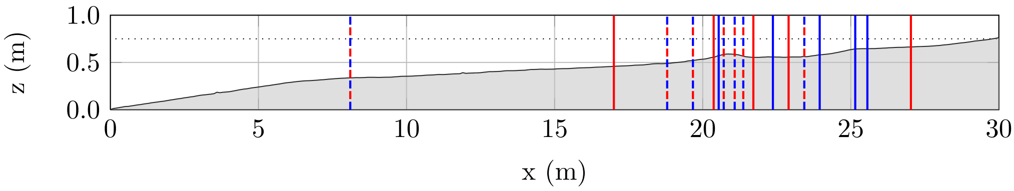

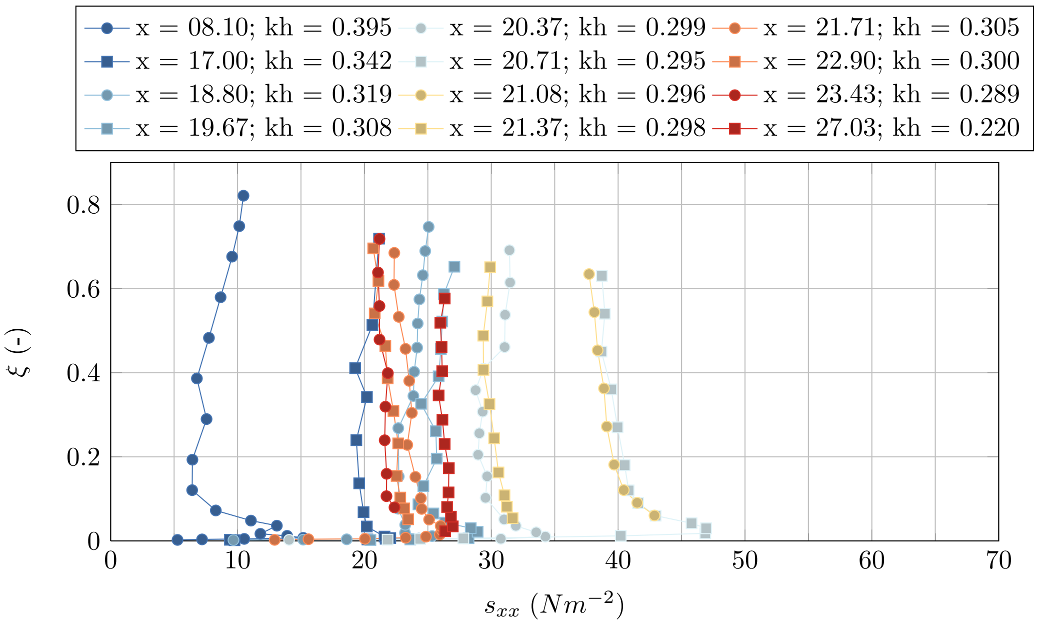

Figure 3.6: *Vertical radiation stress profiles for Boers-1C, weakly plunging breakers*

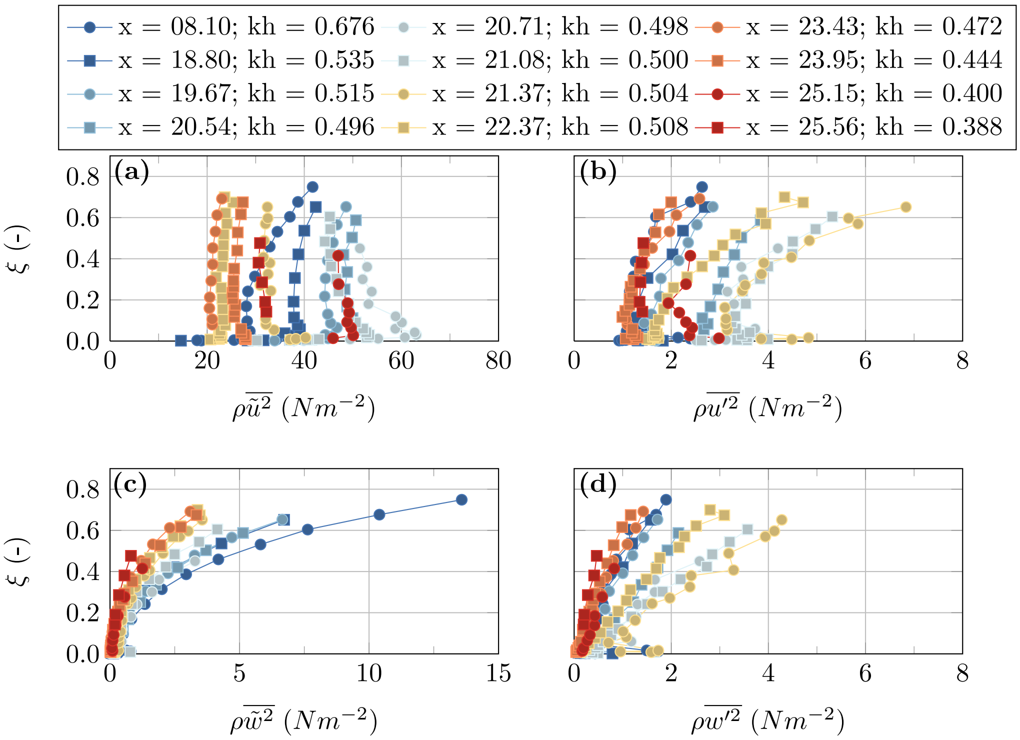

Figure 3.7: *Contributions to total depth-dependent radiation stress for (a) $\rho\overline{\tilde{u}^2}$, (b) $\rho\overline{u'^2}$, (c) $\rho\overline{\tilde{w}^2}$, (d) $\rho\overline{w'^2}$ for Boers-1B*

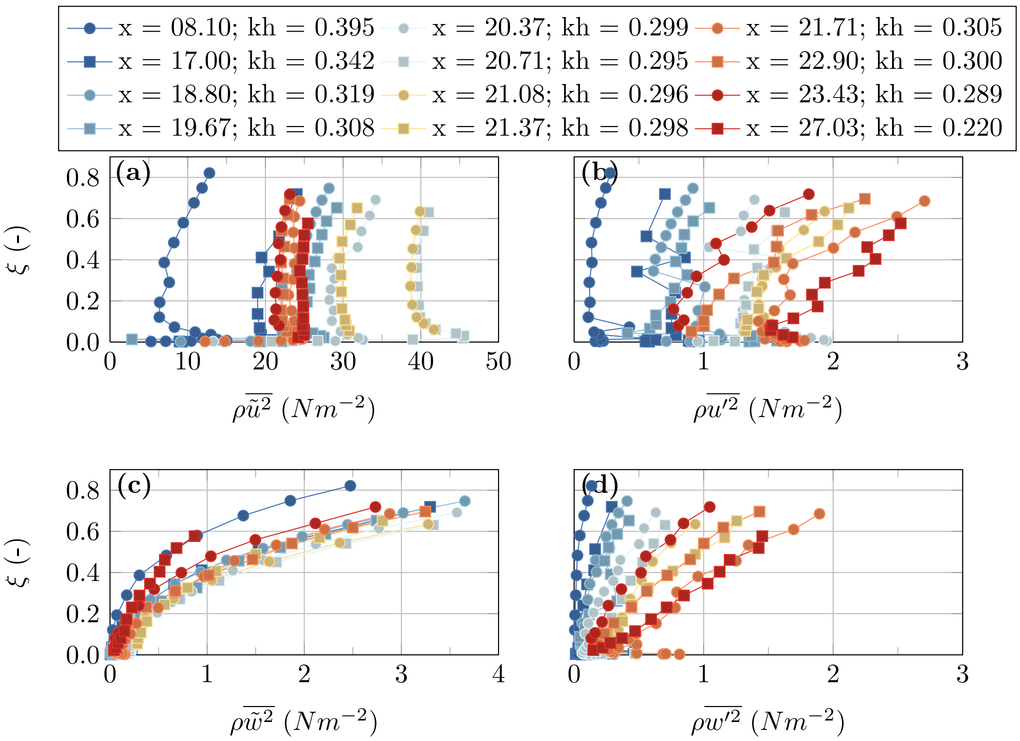

Figure 3.8: *Contributions to total depth-dependent radiation stress for (a) $\rho\overline{\tilde{u}^2}$, (b) $\rho\overline{u'^2}$, (c) $\rho\overline{\tilde{w}^2}$, (d) $\rho\overline{w'^2}$ for Boers-1C*

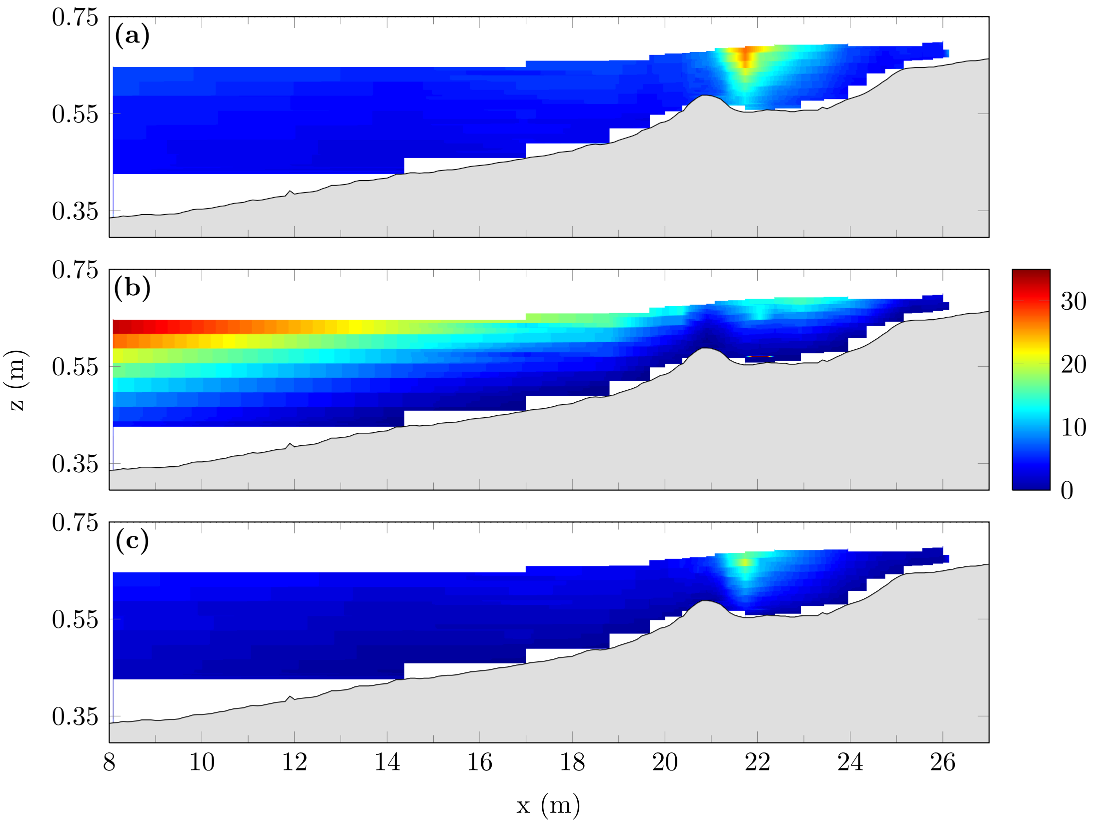

Figure 3.9: *Interpolated procentual size of different contributions compared to $\rho\overline{\tilde{u}^2}$, (a) $\rho\overline{u'^2}$, (b) $\rho\overline{\tilde{w}^2}$, (c) $\rho\overline{w'^2}$ for Boers-1B.*

lead to an increased importance of the turbulence part because of the smaller turbulence production for Boers-1C. For Boers-1B, the contribution of turbulence to radiation stress ($\rho\overline{u'^2} - \rho\overline{w'^2}$) is largest right after the first breaker bar at around 8% of the size of the wave part. In the remainder of the wave flume this is lower at 1–3% (figure D.4a). For Boers-1C, the spread is more evenly and maxima also occur around the breaker bars and in the lower water column with magnitudes of about 6% (figure D.4b). This leads to the conclusion that the contribution of turbulence to radiation stress is minor, even around the breaking areas. This is in agreement with Stive and Wind (1982) who found similar values of around 5% for a plane sloping beach with spilling and plunging breakers of the same order of magnitude as carried out by Boers (1996).

Comparing results between spilling and weakly plunging breakers is difficult because the waves used for plunging were only half the size and would thus create less intensive breaking which results in a lower turbulence production (compare figures 3.23 and 3.24). However, it is clear that the vertical radiation stress profiles for Boers-1C are more uniform. Looking at the different contributions, this is mostly a result of the greater uniformity of the horizontal wave component. This is related to a smaller relative depth (figure 3.2) and not breaker type.

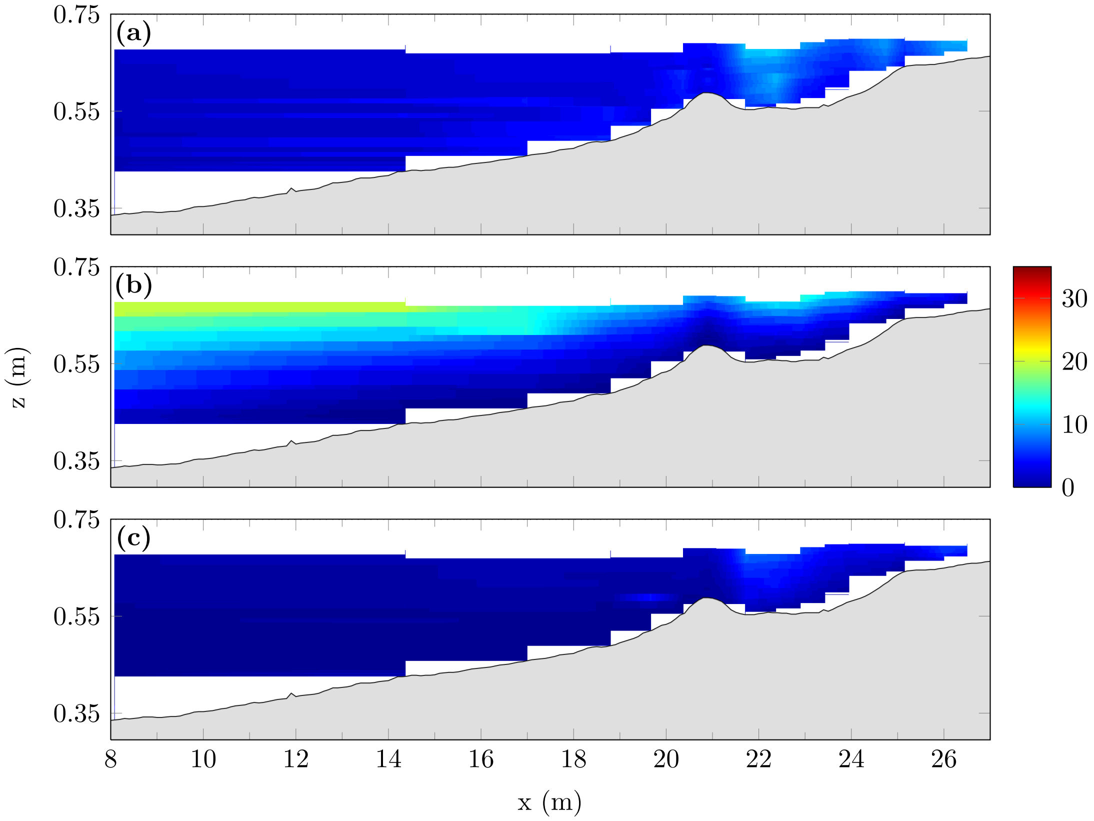

Figure 3.10: *Interpolated procentual size of different contributions compared to* $\rho\overline{\tilde{u}^2}$, *(a)* $\rho\overline{u'^2}$, *(b)* $\rho\overline{\tilde{w}^2}$, *(c)* $\rho\overline{w'^2}$ *for Boers-1C.*

3.3.2 Comparison to analytical radiation stress formulations

To see how well different theories match the profiles found in figures 3.5 and 3.6, they are compared to two different analytical radiation stress formulations. The first formulation is the depth-integrated radiation stress by Longuet-Higgens and Stewart (1964) (LHS) which is based on small wave amplitudes and linear wave theory. This equation has been widely used in wave-driven models, like the roller model (see section 4.1.1). To see if new developments have improved calculations, a depth-dependent radiation stress is also considered. In Kumar et al. (2011) and Sheng and Liu (2011) radiation stress as formulated by Mellor (2008) (M08) showed promise and is therefore the second equation taken into consideration.

Longuet-Higgens and Stewart (1964)

The pioneering work of Longuet-Higgens and Stewart in the 1960s led to a physical explanation for a number of hydrodynamic processes in the nearshore zone. With their concept of radiation stress they successfully explained setdown, setup, longshore currents, undertow, and infragravity waves. The concept of radiation stress is still used around the world in many numerical models. Their equation for radiation stress is based on small amplitude, linear wave theory and is shown in equation 3.8 (Longuet-Higgens

& Stewart, 1964).

$$S_{xx}^{LHS} = E\left(n(\cos^2\theta + 1) - \frac{1}{2}\right) \tag{3.8}$$

where E is wave energy (Nm^{-1}); $n = \frac{1}{2}\left(1 + \frac{2kh}{\sinh 2kh}\right)$ (-); kh is relative depth (-) (figure 3.2); and θ is the wave angle (rad), which in our case is zero. Boers (2005) calculated wave energy for the irregular waves and this data together with the local relative depth is inserted into the equation.

To be able to compare results from measurement data to depth-integrated radiation stress by Longuet-Higgens and Stewart (1964), there are two options: (i) integrate measurement data and compare depth-integrated values or (ii) allocate depth-integrated values over depth and compare depth-dependent values. For the first option one would need all the velocity measurements from bed to wave crest, which are not available for the measurements since we discarded all data above wave trough level. The second option is actually the same procedure as carried out by numerical models in 3D-mode when different layers are forced separately. Because the total depth-integrated radiation stress and water depth are known, the depth-dependent value (which is assumed to be uniform over depth, just as in Delft3D, see section 4.1) is easily calculated by dividing the depth-integrated value with water depth. So equation 3.8 is divided by the water depth and taking $\theta = 0$, leading to:

$$s_{xx}^{LHS} = \frac{E}{h}\left(2n - \frac{1}{2}\right) \tag{3.9}$$

Mellor (2008)

In an effort to combine the mostly separate fields of ocean surface waves modelling and ocean circulation modelling, Mellor (2003) formulated a depth-dependent radiation stress equation. As with Longuet-Higgens and Stewart (1964), Mellor (2003) assumed linear wave theory as a starting point. After comments by Ardhuin, Jenkins, and Belibassakis (2008) and on further investigation, unacceptable errors were found that were solved in Mellor (2008) (M08). The main difference between LHS and M08 – apart from vertical dependence of course – is the fact that the radiation stress between crest and trough (E_D) is concentrated at the surface instead of being distributed over depth as in equation 3.9. When vertically integrated, M08 gives the same result as LHS. To see the effects of rollers on radiation stress, we will also take M08 with a roller contribution into account. We follow Kumar et al. (2011) for this roller contribution:

$$s_{\alpha\beta}^{M08} = \underbrace{kE\left(\frac{k_\alpha k_\beta}{k^2}F_{CS}F_{CC} - \delta_{\alpha\beta}F_{SC}F_{SS}\right) + \delta_{\alpha\beta}E_D}_{\substack{\text{Equation by} \\ \text{Mellor (2008)}}} + \underbrace{\frac{k_\alpha k_\beta}{k^2}R_z E_r}_{\substack{\text{Addition by} \\ \text{Kumar et al. (2011)}}} \tag{3.10}$$

where α and β are horizontal coordinates which could be x and y depending on the direction of interest; k is wave number (m^{-1}); F are form functions shown in equation 3.11; $\delta_{\alpha\beta}$ is given in equation 3.12; E_D represents radiation stress between wave trough and crest; R_z is a vertical distribution equation shown in equation 3.13; and E_r is roller energy (Nm^{-1}) estimated from mass flux (Boers, 2005). E_D can be seen mathematically to be a Dirac delta function with a value of $\frac{E}{2}$ (Mellor, 2012). Simply put, a Dirac delta function has no width, but does have an area. Note that this

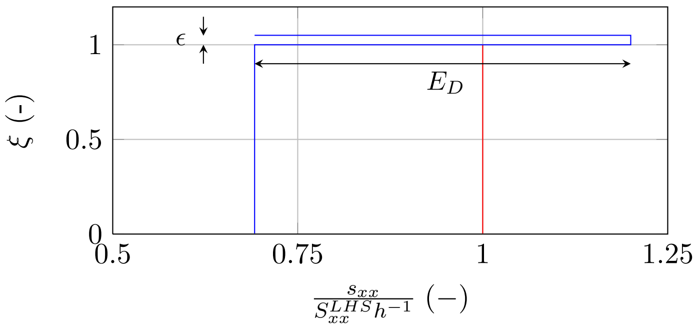

Figure 3.11: *Differences between shallow water radiation stress profiles for LHS (——) and Mellor (——), normalized by LHS. Where ϵ is an infinitesimally small distance (Sheng & Liu, 2011).*

component is the same as the $S_{xx}^{(3)}$ component in Longuet-Higgens and Stewart (1964) and is thus also included in equation 3.8. Since E_D is only applied at the top layer or as a shear stress (see Mellor (2008) and figure 3.11) it is decided to ignore it for now and put it at zero since we will be looking below wave trough level only. For obvious reasons, E_D cannot be ignored when using M08 for flow calculations.

$$\begin{aligned} F_{CC} &= \tfrac{\cosh k(z+h)}{\cosh kD}; \qquad & F_{CS} &= \tfrac{\cosh k(z+h)}{\sinh kD} \\ F_{SC} &= \tfrac{\sinh k(z+h)}{\cosh kD}; \qquad & F_{SS} &= \tfrac{\sinh k(z+h)}{\sinh kD} \end{aligned} \tag{3.11}$$

$$\delta_{\alpha\beta} = \begin{pmatrix} 1 & if & \alpha = \beta \\ 0 & if & \alpha \neq \beta \end{pmatrix} \tag{3.12}$$

With a depth-dependent radiation stress, there is also a need for depth-dependent roller contribution. This depth-dependence is created by the form-function R_z, for which Warner, Sherwood, Signell, Harris, and Arango (2008) is followed. Although Warner et al. (2008) used Mellor (2003, 2005) in their calculations, this has no consequences for the use of R_z. The equation following Warner et al. (2008):

$$R_z = 1 - \tanh^4\left(\frac{2\sigma}{\gamma}\right) \tag{3.13}$$

where σ is the normalized depth with -1 at the bed and 0 at the mean water level; and γ is the ratio of wave height to water depth ($\gamma = H_{rms}h^{-1}$). However, the integral of R_z over depth gives varying values depending on γ, this is not something we want for a form function. Moreover, we would like the roller addition to be the same as the roller model (section 4.1.1) and therefore the vertical integral of R_z needs to be 2. Looking into the integral of R_z leads to the conclusion that rescaling it with $3/\gamma$ gives a good approximation for the range of γ in our case ($\gamma = 0.2 - 0.65$). The integrated equation 3.14 gives values of $2 - 1.987$, respectively. We are content with this approximation. Therefore, to approximate the roller model, we redefine R_z as:

$$R_z = \frac{3}{\gamma}\left(1 - \tanh^4\left(\frac{2\sigma}{\gamma}\right)\right) \tag{3.14}$$

Comparison

Results over the whole wave flume are shown in figures 3.12 and 3.13; and results per location are shown in figures 3.14 and 3.15. It should be noted that these calculations of radiation stress (and later also for wave forces) are based on local conditions only. Advective and diffusive processes are not taken into account and at specific locations where for instance the bottom suddenly changes more extreme values are expected than would be the case in reality or in numerical models. The assumption is that this mainly affects wave force patterns, because of the derivative.

Although radiation stress magnitudes differ between LHS and M08, the pattern is similar, a logical result since both use linear wave theory. M08, although depth-dependent, shows almost no vertical deviations and is virtually uniform because of the shallow water depth. Sheng and Liu (2011) shows the effects of relative water depth on the vertical profile of M08. For larger relative water depths, M08 does show significant depth-dependence. The inclusion of the roller with the vertical distribution profile (R_z) creates vertical variation but this is focused above wave trough level, the dashed lines in figures 3.12 and 3.13. For Boers-1B a significant roller contribution can be seen with increases up to about 100%, compared to no roller. For Boers-1C the increase is considerably less with a maximum of about 50%. The effects of the roller does sometimes reach below wave trough level, but this is not visible in the measurements. The use of R_z as form function is therefore questionable.

Figures 3.14 and 3.15 show that M08 is the most successful in recreating depth-dependent radiation stress. In the bottom boundary layer we see that the analytical equations do not reproduce measurements well, this is because the formulations are not developed for use in this area, but rather the centre region of the water column. For Boers-1B, M08 overestimates depth-dependent radiation stress in the shoaling zone; produces good results near the breaker bar and in the surf zone trough; and underestimates it briefly at $x = 25.15\ m$. For Boers-1C, M08 also shows the best results, but with the exception of $x = 27.03\ m$ slightly overestimates the radiation stress on all locations. LHS overestimates depth-dependent radiation stress on every location by sometimes as much as 100%.

Since integrated both LHS and M08 (without roller contribution) give the same results, it can be concluded that this is because of the use of E_D in M08. For LHS, E_D is not considered separatly and is therefore distributed over the whole water column resulting in an overestimation of depth-dependent radiation stresses below wave trough (figure 3.11). Figures 3.14 and 3.15 seem to support this, since values calculated by M08 are always smaller than those by LHS. This E_D is not specific for M08 but is also included in LHS. And since in the surf zone M08 is (nearly) depth-uniform, a simple separation of LHS-components could give the same results as implementing M08 in a numerical model. The new equation would then become:

$$s_{xx}^{LHS} = \underbrace{\frac{E}{h}(2n-1)}_{\text{Depth-dependent part}} + \underbrace{\frac{E}{2}}_{\text{Shear stress}} \tag{3.15}$$

3.4 Wave forces

As discussed in section 2.3.2, it is not radiation stress that drives the flow, but its derivative: the wave force. To calculate depth-dependent wave forces (note the small case

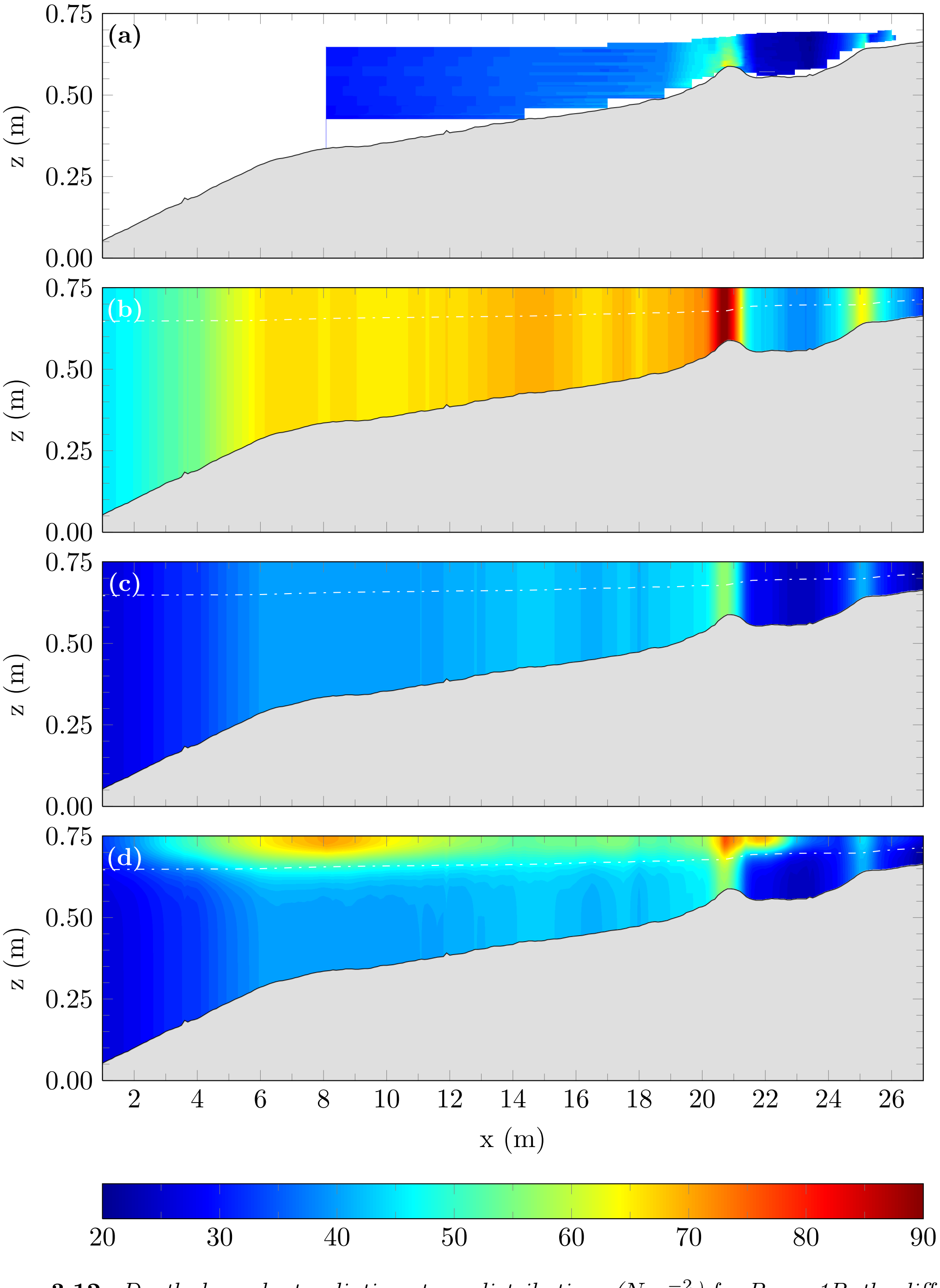

Figure 3.12: *Depth-dependent radiation stress distributions (Nm^{-2}) for Boers-1B, the different graphs show: (a) interpolated measurements; (b) Longuet-Higgens and Stewart; (c) Mellor without roller; and (d) Mellor including roller. The dashed lines show the position of wave trough level.*

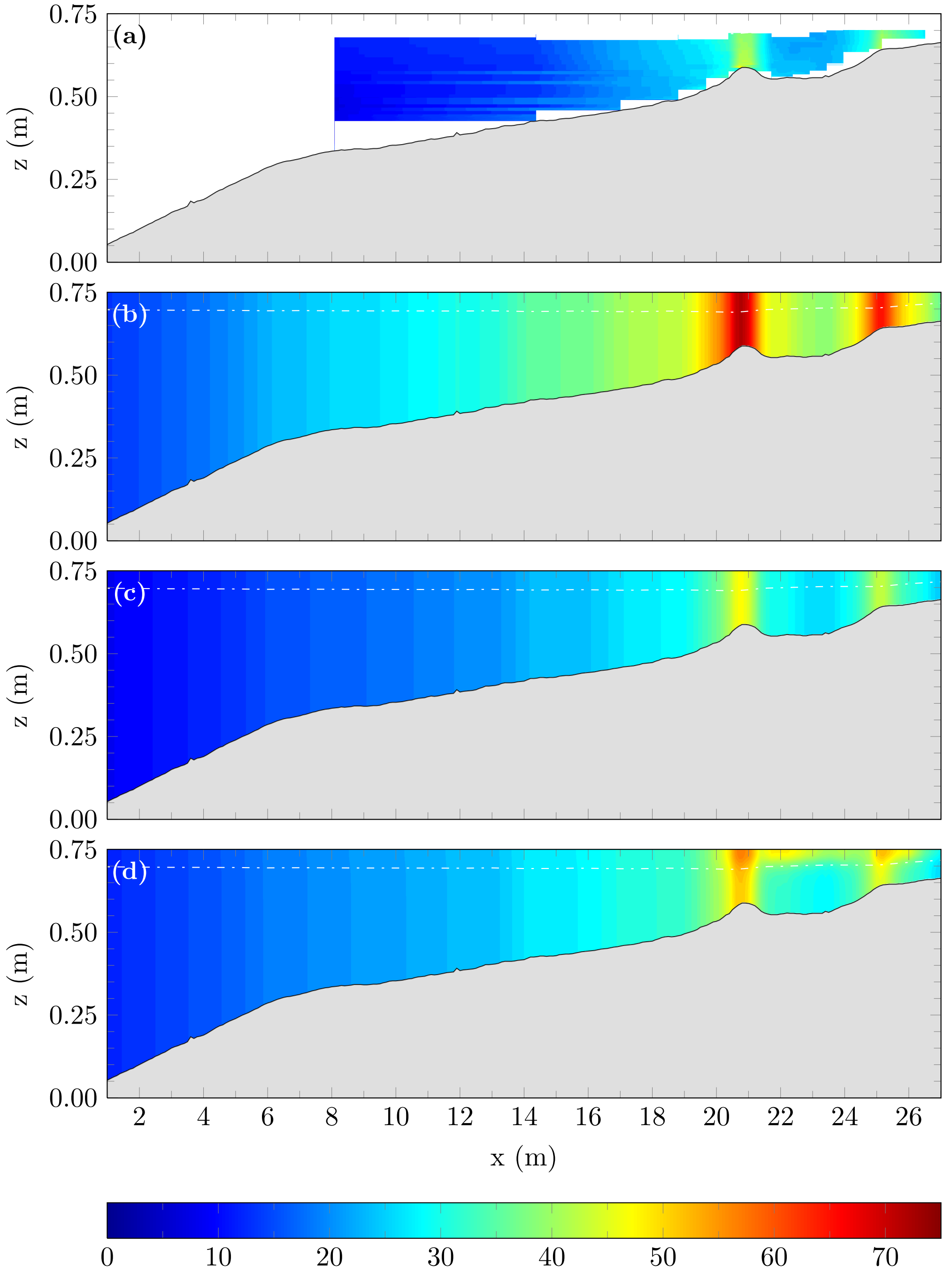

Figure 3.13: *Depth-dependent radiation stress distributions (Nm^{-2}) for Boers-1C, the different graphs show: (a) interpolated measurements; (b) Longuet-Higgens and Stewart; (c) Mellor without roller; and (d) Mellor including roller. The dashed lines show the position of wave trough level.*

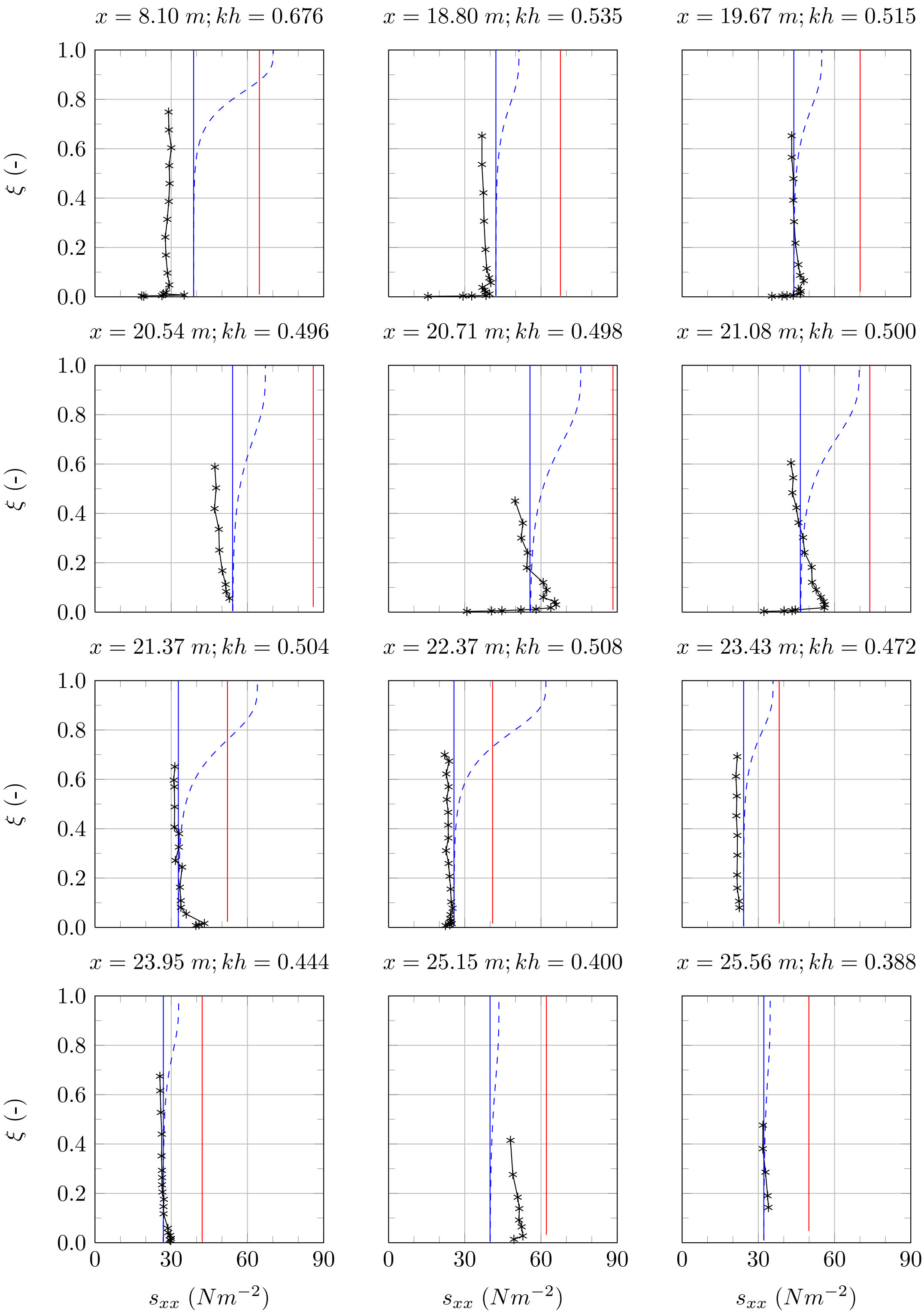

Figure 3.14: *Depth-dependent radiation stress distributions (Nm^{-2}) for Boers-1B, with measurements (—∗—); Longuet-Higgens and Stewart (1964) (——); Mellor (2008) without roller (——); and Mellor (2008) with roller (- - -).*

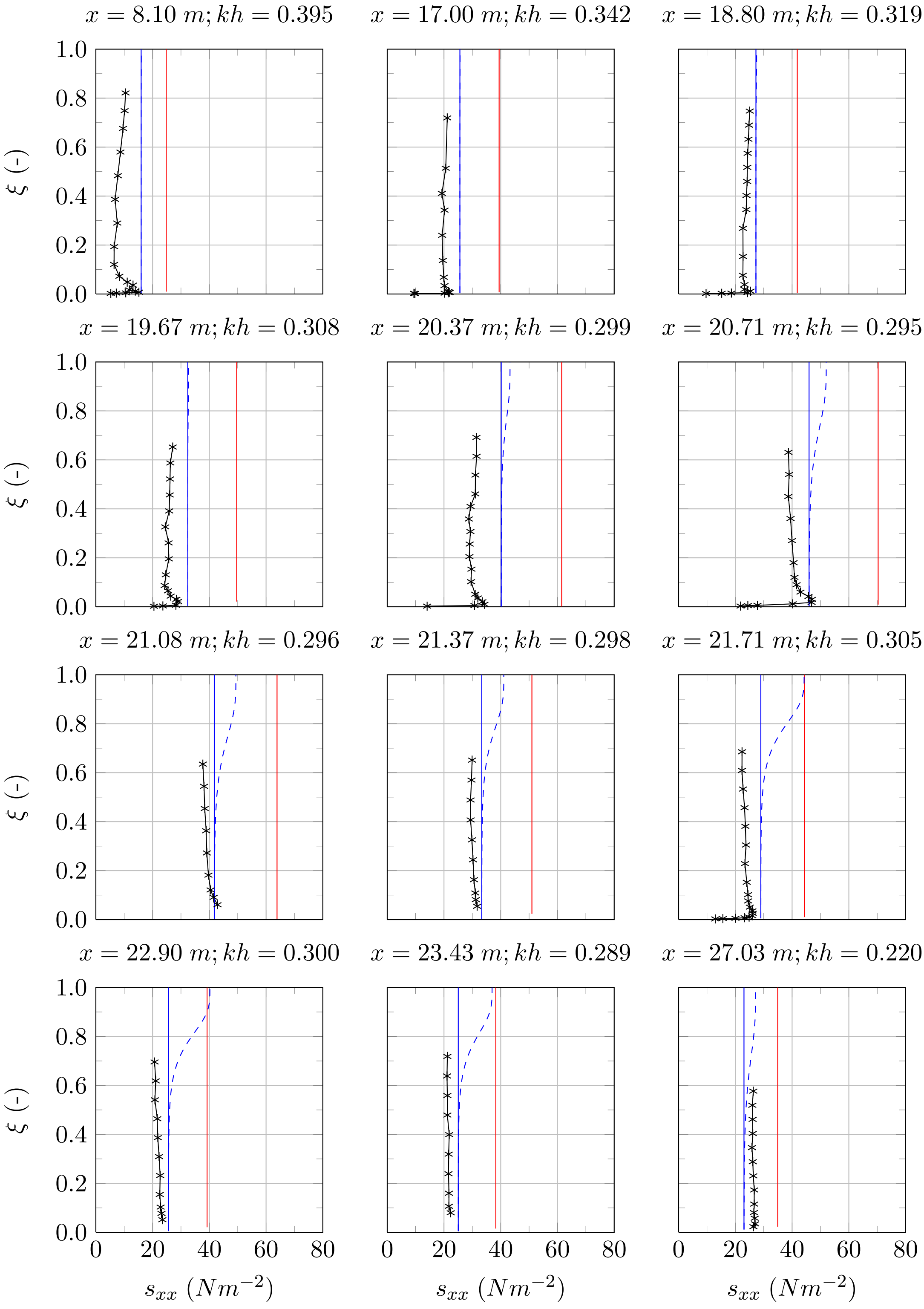

Figure 3.15: *Depth-dependent radiation stress distributions (Nm^{-2}) for Boers-1C, with measurements (—∗—); Longuet-Higgens and Stewart (1964) (——); Mellor (2008) without roller (——); and Mellor (2008) with roller (- - -).*

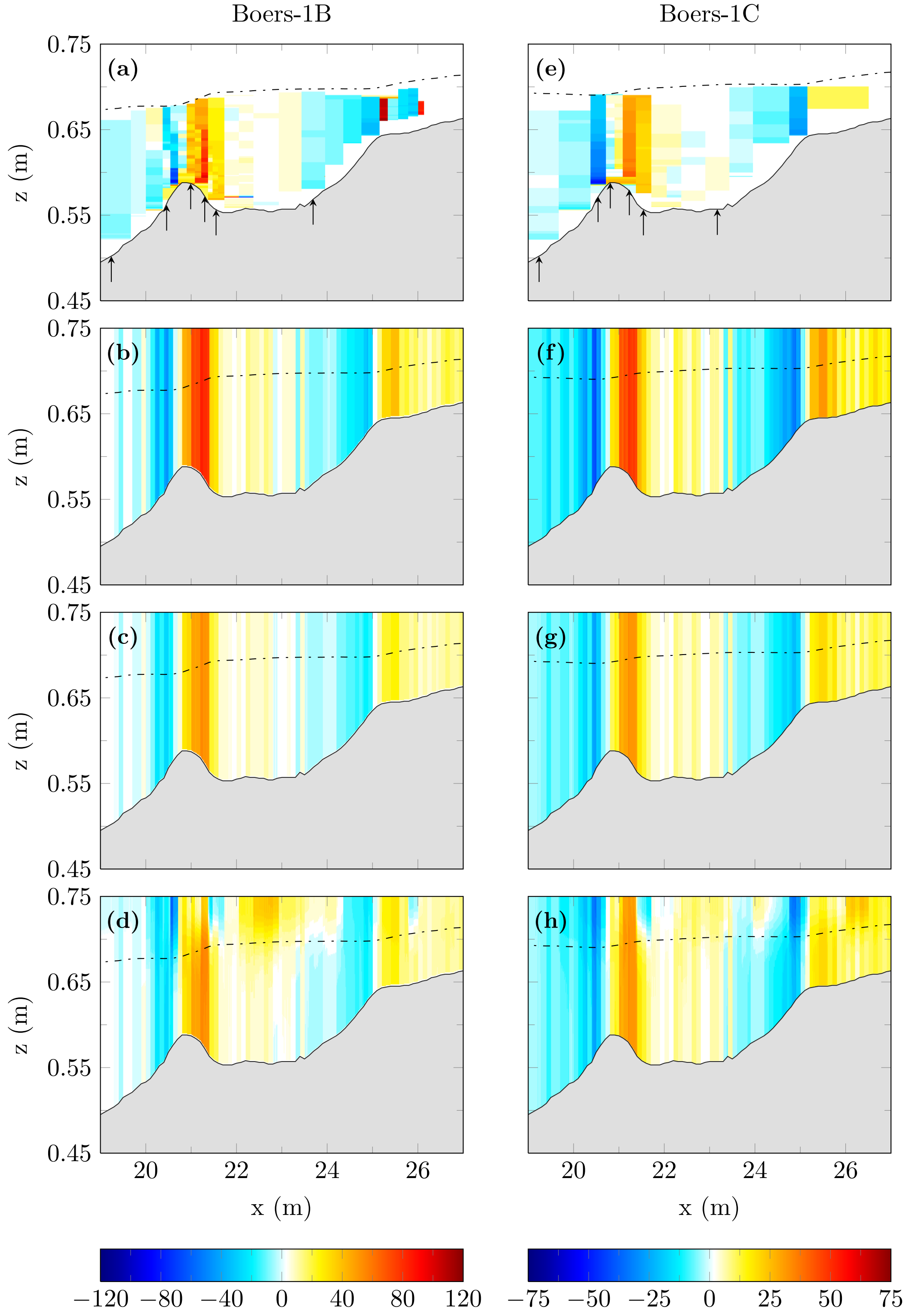

Figure 3.16: *Wave force distributions (Nm^{-3}) for Boers-1B (a-d) and Boers-1C (e-h), the different graphs show: (a,e) measured; (b,f) Longuet-Higgens and Stewart; (c,g) Mellor without roller; and (d,h) Mellor including roller. Dashed lines show the location of wave trough level and arrows show the x-locations of the profiles in figure 3.17.*

f), the derivative of depth-dependent radiation stress is taken following equation 3.16:

$$f_{wave,xx}(z) = -\frac{\partial s_{xx}(z)}{\partial x} \tag{3.16}$$

Calculating depth-dependent wave forces from measurements leads to problems because some areas lack high density experimental data. For this reason, only the area around the breaker bar is considered where measurement density is higher. This is also the most important area for the wave forces since they are small in the remainder of the wave flume. Furthermore, measurement points are required to be at the same height in order to use the x-derivative. Since this is not the case for all locations, radiation stresses were first linearly interpolated over the vertical, before the derivative was taken.

3.4.1 Measured wave forces and analysis

Figure 3.16 shows the resulting wave force distributions for the measurements and analytical formulations for both Boers-1B and Boers-1C. In figures 3.16a and 3.16e it can be seen that for both Boers-1B and Boers-1C, negative wave forces (ie. directed offshore) are found on the offshore side of the breaker bar (left side in the figure). As explained in section 2.3.2, this is (mainly) compensated by an onshore directed pressure force. This means that $\partial p/\partial x$ is negative and thus setdown occurs, this is in line with theory and results found by Boers (2005) (figure 3.3). At around $x = 20.7$ m – just before the crest of the breaker bar – the wave forces switch sign and become positive, leading to setup (in accordance with Boers (2005)). The maximum wave forces occur around $x = 21.3$ m, after which wave forces decrease in magnitude in the surf zone trough. For the weakly plunging breakers (Boers-1C) they seem to become negative in the surf zone trough, which suggests that shoaling takes place. However, this cannot be seen in wave heights (figure 3.1) and looking at figure 3.6, locations $x = 22.90$ m and $x = 23.43$ m, the differences are very small and are well within uncertainty ranges for the measurements. Approaching the second breaker bar, the wave forces become negative again: which causes setup levels to decrease (figure 3.3). At the crest of the second breaker bar, the wave forces switch to positive values once more. For Boers-1B, wave forces quickly switch to negative again on the second breaker bar, results from this point are however doubtful since mean water depth is less than 10 cm and below wave trough only 5 cm. As with radiation stress profiles, a slight vertical profile can be seen in the measured wave forces, especially on the breaker bar. But on other locations this is negligible.

A striking difference between the results presented here and in Stive and Wind (1982) are the negative wave forces just before the breaking point. In Stive and Wind (1982) they are very small, nowhere near the same magnitude as is found in the data from Boers (2005). Although in the Boers (2005) data the negative wave forces do not reach the same magnitude as the positive ones, they are close. The difference can possibly be explained by the difference in bed profile. Stive and Wind (1982) used a slopping bottom where Boers (2005) included breaker bars. These bars have an increasing gradient (up to a maximum of 7°) which causes a rapid increase in radiation stress (mostly through the horizontal wave component, as shown in section 3.3) which leads to large negative wave forces. In Stive and Wind (1982) the change is more gradual (slope angle is a constant 1.4°) and the large negative wave forces do not occur. The decrease in radiation stress (and thus positive values of wave forces) occurs in both cases because of the breaking of waves (ie. energy dissipation) in which mostly the horizontal wave component decreases, where the turbulence contribution remains minor. We can thus conclude that the bottom slope is important for the magnitude of negative wave forces.

The depth-dependent wave force profiles as shown in figure 3.17, are set at x-locations that are in the middle two measurement locations. Because of the x-derivative used to calculate wave forces, the assumption is that the best approximation is given in the middle. Therefore, it is seen fair to compare wave forces at these locations. Values close to the bottom, should be considered with care since during the interpolation process some values were interpolated over the breaker bar. Meaning that values left and right of the crest were interpolated despite the fact that the bottom was in between them (the values inside the profile were removed afterwards). One thing is certain, at the bed the wave and turbulent parts of equation 3.7 go towards zero and only the setup part remains (see figures D.2 and D.3). Change in setup is small and thus also wave forces will be small.

The measured depth-dependent wave force profiles can be seen to fluctuate quite heavily, this is a result of the necessary vertical interpolation of depth-dependent radiation stresses. Depth-dependent wave force profiles are found to be mostly uniform with the exception of wave forces low in the water column at the breaker bar.

3.4.2 Comparison to analytical formulations

As with depth-dependent radiation stress distributions, also for wave forces there are no large differences between patterns calculated by LHS and M08 (figure 3.16). Because advective and diffusive processes are neglected, quick responses to (small) bathymetry changes can be seen and the calculated wave forces show rapidly change values. These should be ignored for analysis and only the overall look of the patterns should be taken into account. The main difference between measurements and analytical formulations is the switch from negative to positive which seems to occur slightly further on the breaker bar for the analytical formulations, although this could be related to the relatively low resolution. Despite the fact that measurements were very detailed compared to other laboratory or field research, wave forces may still miss subtleties because of the derivative. It also means that the wave forces are an average of the area between the two measurement x-locations it is derived from, in contrast to velocity measurements which are from that exact location.

It is difficult to say if M08 or LHS performs better (figure 3.17). Differences between the two methods are not very large and due to the fluctuating measured wave forces, no clear answer can be given. Where depth-dependent radiation stress for M08 were always smaller than LHS, also depth-dependent wave forces for M08 are always closer to zero (so less negative and less positive) than LHS. The influence of the roller is obvious above wave trough level which at certain locations even leads to the opposite sign compared to the wave force below wave trough level. Below wave trough level, the roller contribution is very small. Near the second breaker bar for Boers-1B, differences can be seen between measurements and calculations. But as discussed before, the validity of the measurements is questioned in this case because of the extremely shallow water depth. For Boers-1C patterns are similar between calculations and measurements.

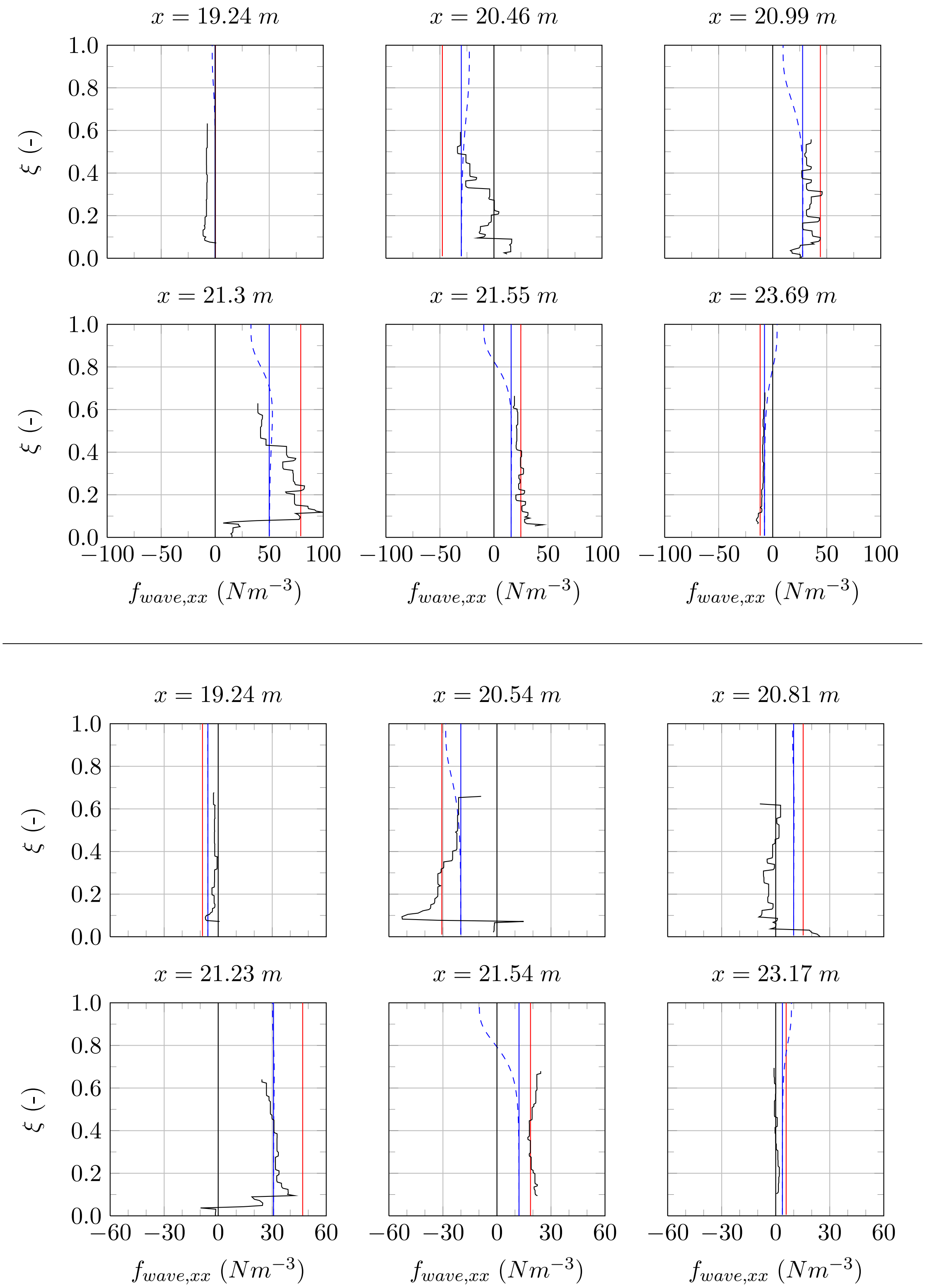

Figure 3.17: *Depth-dependent wave force distributions (Nm^{-3}) for Boers-1B (top) and Boers-1C (bottom), with interpolated measurements (——); Longuet-Higgens and Stewart (1964) (——); Mellor (2008) without roller (——); and Mellor (2008) with roller (- - -).*

3.5 Reynolds stresses

Boers (2005) showed wave Reynolds stress for locations onshore of the first breaker bar, which were used as input for an undertow model. Reynolds stresses were, however, not analysed in Boers (2005) which will be carried out in this section. Figures 3.18 and 3.19 show the extracted Reynolds stresses, figures D.5 and D.6 shown details in the bottom boundary layer.

3.5.1 Mean flow Reynolds stress

In section 2.3.2 it was discussed that $\rho\overline{\bar{u}\bar{w}}$ should be zero. This is however not the case from the measurement data (figures 3.18a and 3.19a), which show a tendency towards negative vertical velocities. Since the magnitude of most of the velocities is around 10^{-3} ms^{-1}, it is expected to be a result of measurement, device calibration or decomposing errors. Higher values ($10^{-2} - 10^{-1}$ ms^{-1}) are found on a couple of locations, but these are all high in the water column and were already disregarded when the choice was made to only look below wave trough.

3.5.2 Wave Reynolds stress

In section 2.3.2 it became clear that the last few decades, the non-zero nature of the wave Reynolds stress has been accepted and was proven by field measurements. Also, for Boers (2005) measurements non-zero values are found throughout the water column (figures 3.18b and 3.19b). Comparing results to laboratory measurement from De Serio and Mossa (2006) we see similarities between results in the shoaling zone. Both see positive values and the vertical trend to be more or less linear. Near the breaker zone, wave Reynolds stresses from measurements switch to negative. This is at odds with De Serio and Mossa (2006) where the sign remains positive throughout the wave flume, this is related to the difference in bathymetry. Between the different tests carried out by De Serio and Mossa (2006) – different breaker types and varying wave heights – large differences can be seen in magnitude and profile. Results from Boers-1B and Boers-1C are however remarkably similar in profile. It is therefore uncertain if the differences seen in De Serio and Mossa (2006) are caused by breaker type, wave height or something else.

The shape of the vertical profile close to the breaker bar from data is best represented by the equation from Zou et al. (2006) for non-dissipative waves propagating over a sloping bottom (equation 3.17), this equation is based on Stokes waves. This is surprising since this is the location where most wave breaking occurs. It should be said, however, that the effects of breaking are to be calibrated in this equation. The same was seen by Zou et al. (2006) comparing measurement data with their model. They give flow blocking by the instrument packages as possible reason. It is unknown if this also occurred with

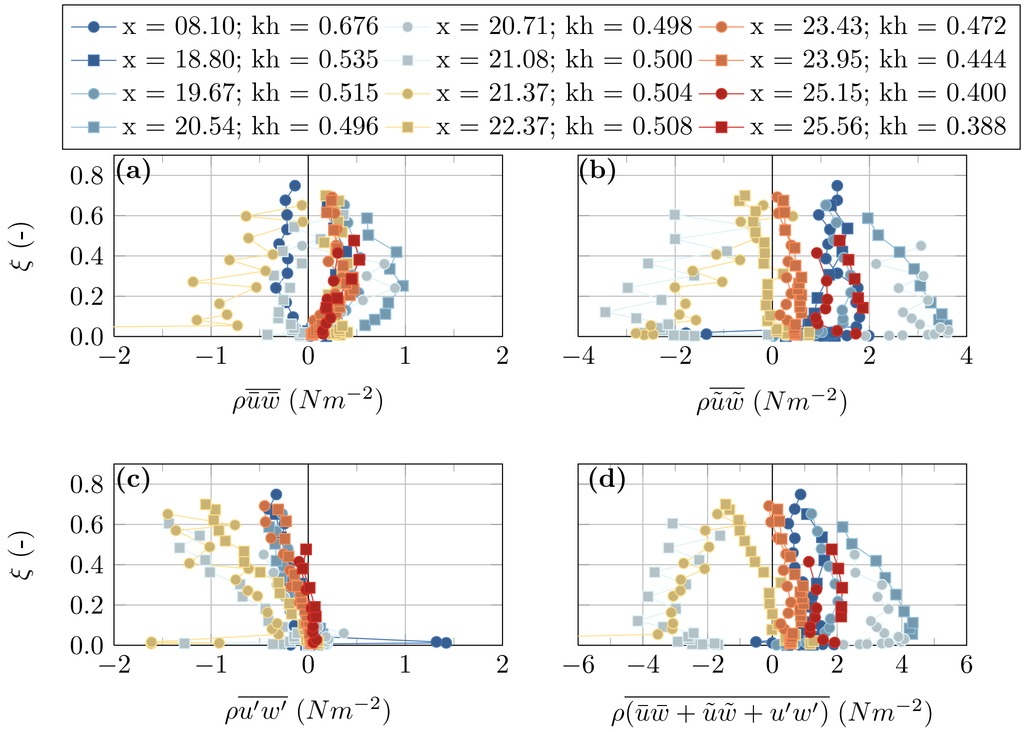

Figure 3.18: *Vertical fluxes of horizontal momentum by (a) $\rho\overline{\bar{u}\bar{w}}$, (b) $\rho\overline{\tilde{u}\tilde{w}}$, (c) $\rho\overline{u'w'}$, (d) sum of previous three components for Boers-1B*

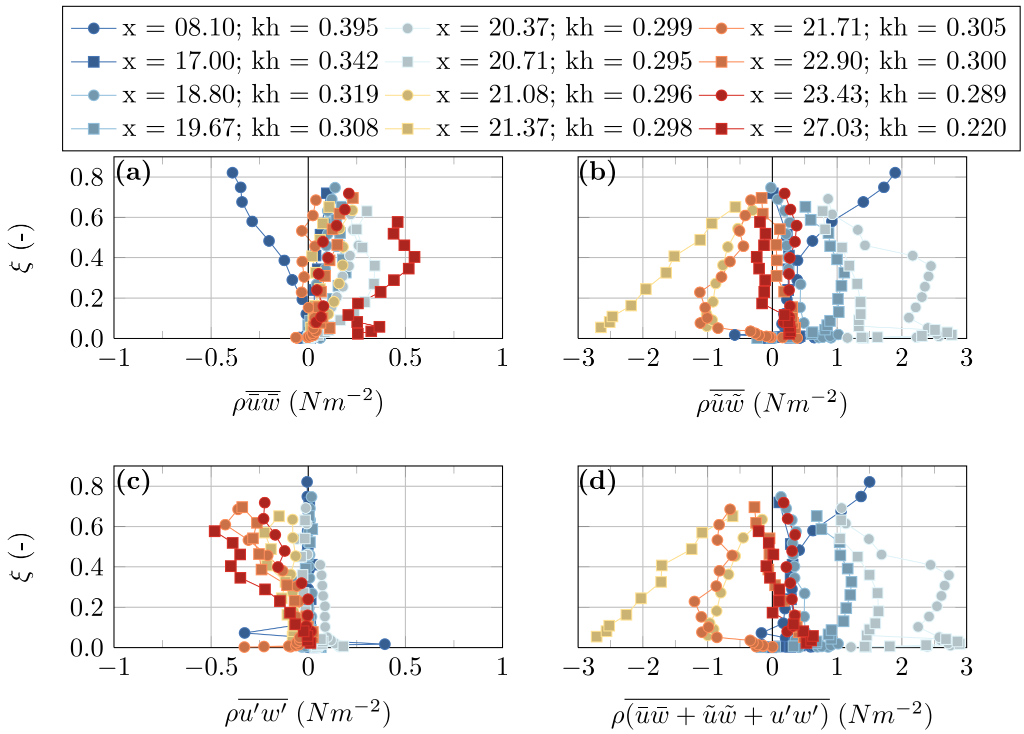

Figure 3.19: *Vertical fluxes of horizontal momentum by (a) $\rho\overline{\bar{u}\bar{w}}$, (b) $\rho\overline{\tilde{u}\tilde{w}}$, (c) $\rho\overline{u'w'}$, (d) sum of previous three components for Boers-1C*

Boers (2005) data.

$$\rho\overline{\tilde{u}\tilde{w}} = -G\frac{E}{h}\Bigg\{\overbrace{h_x\left[1-\frac{1}{1+G}\frac{kh}{\tanh kh}\frac{z+h}{h}-\frac{G}{(1+G)^2}(1-kh\tanh kh)\frac{z+h}{h}\right]}^{Bottom\ slope}+$$
$$\underbrace{\frac{f_w|U_b^{(1)}|}{2c}\left[\cosh k(z+h)-\frac{ck(z+h)}{c_g\sinh 2kh}\right]}_{Bottom\ friction}-\underbrace{\frac{1}{2\pi}B^3kH\frac{z+h}{z}}_{Breaking\ waves}\Bigg\} \tag{3.17}$$

$$f_w = \exp\left(-6+5.2\left(\frac{a}{k_s}\right)^{-0.19}\right) \tag{3.18}$$

where G is $\frac{2kh}{\sinh 2kh}$; E is wave energy; h is water depth; h_x is the change in water depth, note that this is opposite of the change in slope; f_w is friction factor, which is calculated with equation 3.18, setting k_s at 0.002 (smoothed concrete) and where a is amplitude of horizontal oscillatory water displacement near the bed; $U_b^{(1)}$ is wave bottom velocity amplitude, which does not change much and since effects of bottom friction are small is set to 0.4; c is phase velocity; c_g is group velocity; B is an empirical breaker coefficient, set to 1 as in Zou et al. (2006); and H is wave height. Note that this equation assumes that $z = 0$ at water level and $z = -h$ at bed level.

The sloping bottom in the equation gives an explanation for the changing sign. Positive at an upward sloping bottom, negative at a downward sloping bottom, and zero at a horizontal bottom. Before the crest of the first bar at $x = 20.9$ m the slope is positive, after that until about $x = 21.9$ m the slope is negative and thus also $\rho\overline{\tilde{u}\tilde{w}}$. This is visible for both Boers-1B and Boers-1C.

Comparison wave Reynolds stress

The measured wave Reynolds stresses are compared to the equation formulated by Zou et al. (2006) for wave Reynolds stresses by bottom slope, bottom friction, and wave breaking. The equation presented here (equation 3.17) is only for flow above bottom boundary layer (BBL), the equation for inside the BBL is not considered (see Zou et al. (2006) for the equation).

In figures 3.20 and 3.21, the resulting wave Reynolds stresses are presented for twelve locations in the wave flume. It becomes obvious that breaker-generated wave Reynolds stresses only have a minor influence with $B = 1$. Looking at the results, it is clear that changing this parameter will not improve results for most locations, since problems are related to the bottom value being wrong – something that is not fixed by changing B. The change of sign is modelled well: positive values appear in sync with measurements, as are negative ones and even where no slope is present ($x = 22.37$ m for Boers-1B) wave Reynolds stresses are zero, as to be expected. The only problem occurs at $x = 23.43$ m, which is the location where a small bump in the bottom profile occurs (something similar occurs for Boers-1C at $x = 21.71$ m. As with analytical wave forces, the analytical equation reacts heavily on small changes and thus results are different from measurements. The magnitude of modelled wave Reynolds stresses is acceptable on most locations, which is to be expected since it depends on measured wave energies. Some problems occur on the breaker bar, where values are slightly off, although for

Boers-1B and Boers-1C $x = 21.37$ m, this could be fixed by calibrating B. All in all, the equation by Zou et al. (2006) performs quite well above BBL.

3.5.3 Turbulent Reynolds stress

Figures 3.18c and 3.19c show the turbulent Reynolds stress, which are on average smaller than wave Reynolds stresses, but its maximum is high in the water column where wave Reynolds stresses are maximum in the lower water column. Offshore turbulent Reynolds stresses are (close to) zero and increase in magnitude when wave breaking occurs. The fact that the highest values occur at the water surface, suggests the main turbulence production comes from wave breaking, as is to be expected. Results are similar to those found in laboratory tests by De Serio and Mossa (2006) and field observations by Ruessink (2010). There is a tendency to negative turbulent Reynolds stresses, which means downward transport of cross-shore turbulence (Ruessink, 2010).

Comparing results to Umeyama (2005), the profiles are completely different and largest values are mostly found at the bottom. No breaking waves are present in Umeyama (2005), which could explain this difference. Also the sign is opposite of what found in data, suggesting that wave breaking causes the sign of turbulent Reynolds stresses to switch.

Stive and Wind (1986) assumed $\rho\overline{\tilde{u}\tilde{w}} \ll \rho\overline{u'w'}$ while deriving an equation for horizontal mean flow. From the data we see rather different results: the wave Reynolds stress is the largest of the two on a lot of locations. Even when it is smaller, it is not negligible compared to turbulent Reynolds stresses.

3.5.4 Summed Reynolds stresses

Stive and Wind (1986) showed that the vertical profile of the combined shear stresses below wave trough is practically uniform, from Boers (2005) data we see something similar. From the data analysis it becomes clear that this is a result of the opposing profiles of the wave and turbulent Reynolds stresses. However, since the smaller magnitude for turbulent Reynolds stresses, the summed Reynolds stresses are not completely uniform over depth.

3.6 Size comparison of RANS-components

Components two to five of equation 2.6a have now been analysed. To see how important the components are, the different derivatives will be calculated and compared. Component two has already been calculated and resulted in wave forces (section 3.4, note that in equation 2.6a component two is the negative wave force). The Reynolds stresses (components three to five) were analysed in section 3.5, but no derivatives have been calculated yet. Components one and six have not been analysed, component one will be calculated here as well and component six is assumed to be negligible because the surf zone considered here is assumed to be highly turbulent. For clarity, the RANS-equation is repeated here, with the assumption of component six being negligible:

$$\underbrace{\frac{\partial \rho \overline{\bar{u}^2}}{\partial x}}_{(1)} + \underbrace{\frac{\partial S_{xx}}{\partial x}}_{(2)} + \underbrace{\frac{\partial}{\partial z}\left[\rho\left(\overline{\bar{u}\bar{w}} + \overline{\tilde{u}\tilde{w}} + \overline{u'w'}\right)\right]}_{(3-5)} = 0 \tag{3.19}$$

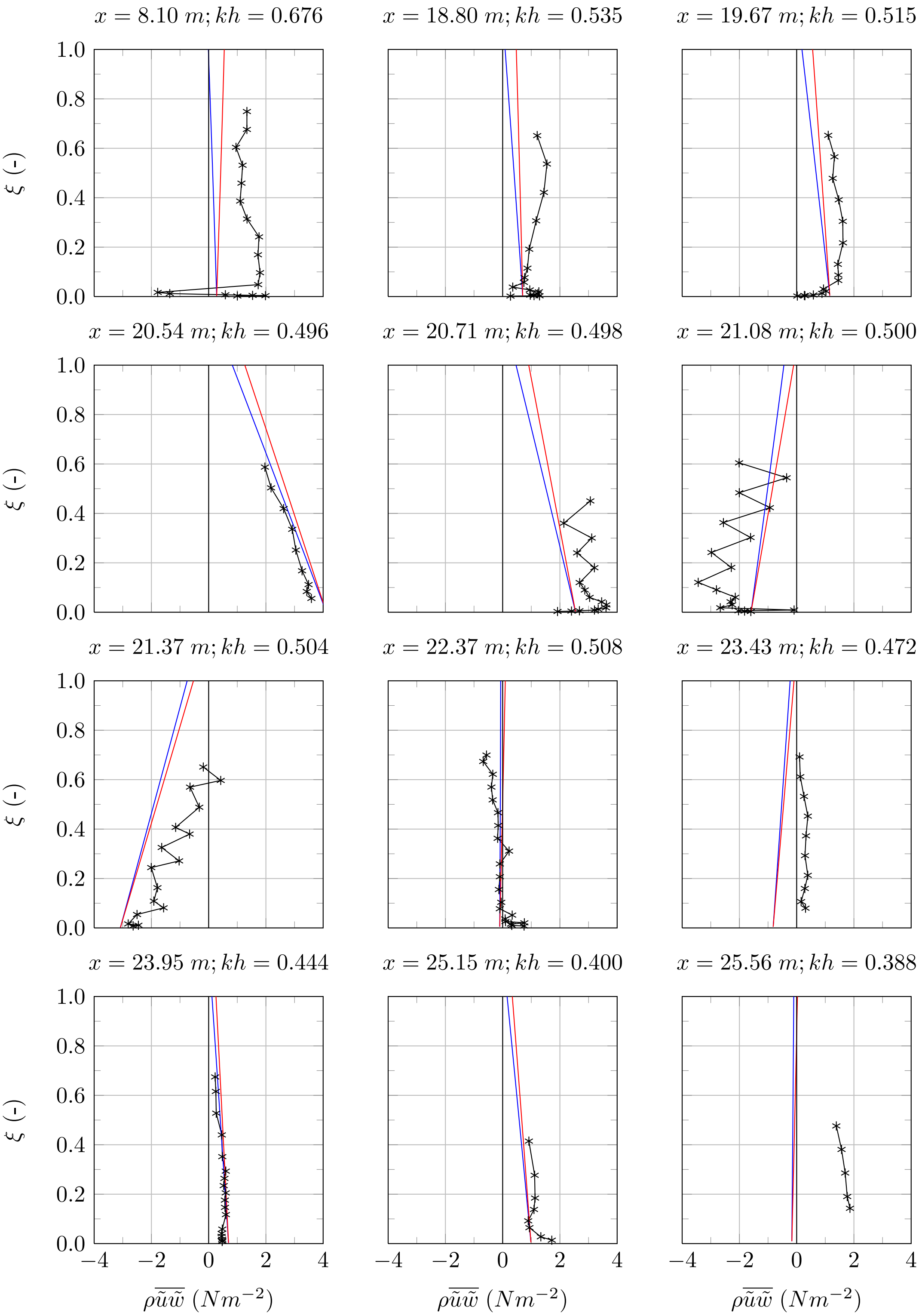

Figure 3.20: *Comparison of measured to calculated wave Reynolds stresses by the equation of Zou et al. (2006) for Boers-1B. Blue is bottom slope and bottom friction; red also includes wave breaking.*

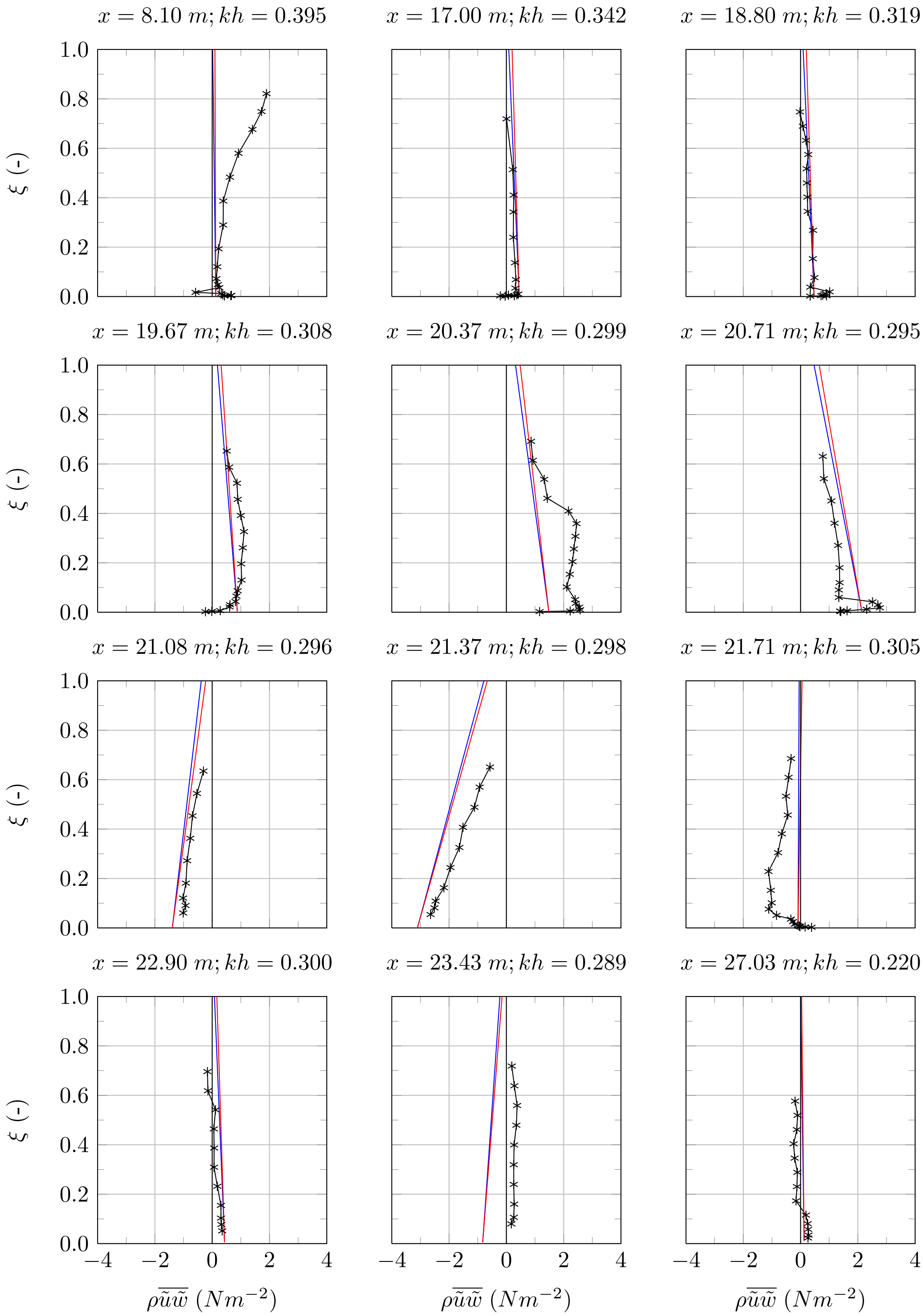

Figure 3.21: *Comparison of measured to calculated wave Reynolds stresses by the equation of Zou et al. (2006) for Boers-1C. Blue is bottom slope and bottom friction; red also includes wave breaking.*

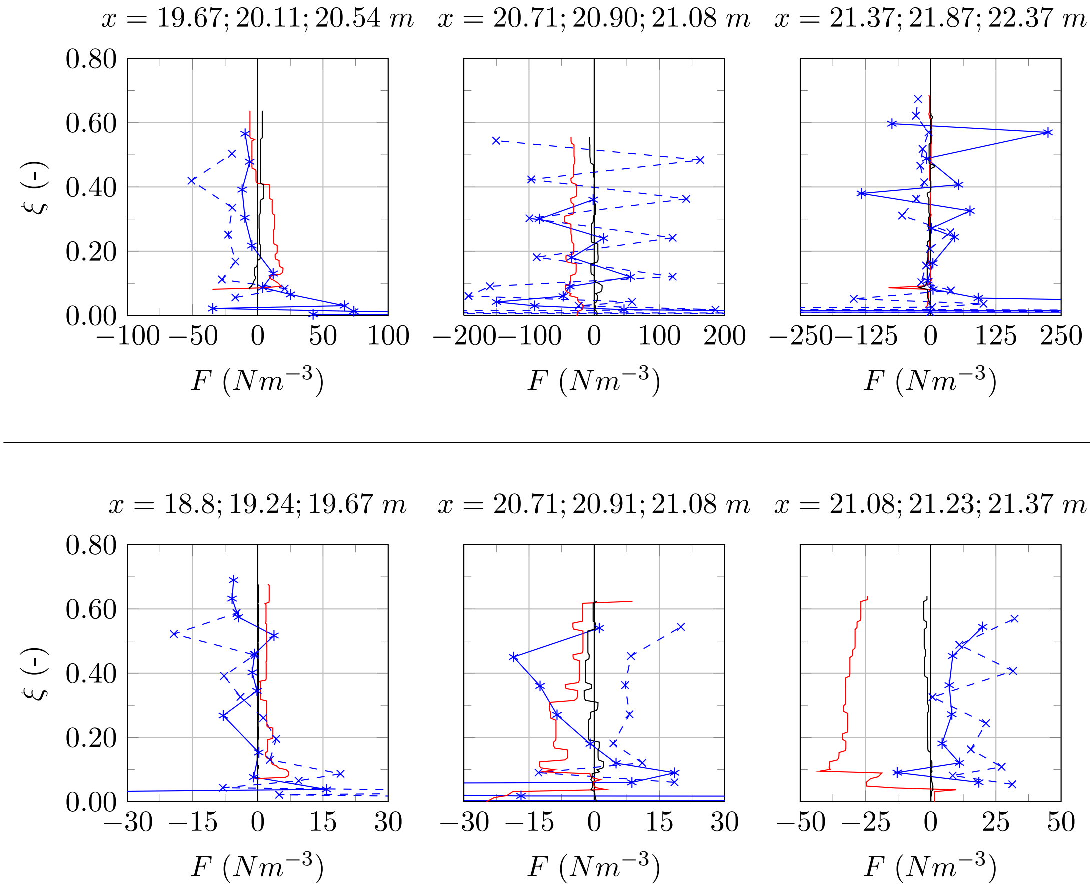

Figure 3.22: *Comparison of RANS-components for Boers-1B (top) and Boers-1C (bottom). Presented are the x-derivative of the mean-flow components, component 1 (——); x-derivative of depth-dependent radiation stress, component 2 (——); and z-derivative of the summed Reynolds stresses, components 3 to 5 for offshore-side (—∗—) and onshore-side (- × -) compared to location of wave forces.*

Since there are two different derivatives (x-derivative for mean-flow and depth-dependent radiation stress; and z-derivative for Reynolds stresses) the magnitudes of the different components are not known at the same location. For the x-derivatives we assume the best approximation is given halfway the two measurement locations; for the z-derivative the x-location stays the same, obviously. For this reason, we have plotted the Reynolds stresses of the two closest x-locations together with the mean-flow and depth-dependent radiation stress. In figure 3.22 the outermost x-locations are the locations for the Reynolds stresses, the x-location in the middle shows the location of the wave forces. However, this also means that the components are compared at different water depths and slopes. Furthermore, the z-derivative is sensitive to small measurement inaccuracies which could lead to derivatives having the wrong sign and/or too large value. All in all, the following results should be considered with care.

In figure 3.22 it can be seen that the Reynolds stresses and wave forces above bottom boundary layer work against each other, and they have more or less the same magnitude (although this is not clearly visible at all locations). On the offshore side of the breaker bar ($x < 20.85\ m$) depth-dependent radiation stresses increase because of shoaling (positive gradient). Reynolds stresses are positive and getting smaller higher in the water column mainly because of the wave Reynolds stress and thus the positive bottom slope (leading to a negative gradient). On the onshore side of the breaker bar ($x > 20.85\ m$) depth-dependent radiation stresses decrease because of breaking (negative gradient) and Reynolds stresses switch to negative, increasing higher in the water column mainly because of the wave Reynolds stress and thus the negative slope (leading to a positive gradient). Note that for Boers-1C, $x = 20.91m$, the offshore Reynolds stress is offshore of the crest of the breaker bar and the onshore Reynolds stress is onshore of the crest. In other words, the slope for both Reynolds stresses is different. From this we can conclude that when a plane slopping bottom is used in measurements the forcings due to depth-dependent radiation and Reynolds stresses would amplify one-another. Breaking would still occur – causing a change of sign for the depth-dependent radiation stress gradient; but the sign of Reynolds stresses would not change since the bottom slope remains positive. Therefore, just after breaking both the radiation stress and Reynolds stresses would show negative gradients.

Component one ($\rho\overline{u}^2$, equation 3.19) can be seen as a reactionary component and consists of the difference between the gradients of depth-dependent radiation and Reynolds stresses. Because they largely cancel each other out, this component is small. This is also what we would expect, since undertow velocities are only minor.

The flow in the bottom boundary layer is mostly driven by the Reynolds stresses, which have much larger derivatives than radiation stress has. This is because in this area the z-derivative is much larger than the x-derivative. Of the Reynolds stresses, the wave Reynolds stress is the largest contributor, although above the bottom boundary layer for Boers-1B the order of magnitude of the turbulent and wave Reynolds stresses is comparable. Inside the bottom boundary layer, wave Reynolds stresses clearly dominate the forcing.

3.7 Turbulent kinetic energy

Section 2.2.5 discussed breaker-induced turbulence. A common measure for turbulence is turbulent kinetic energy (TKE). Since only the cross-shore horizontal (u) and vertical velocities (w) were measured, the alongshore horizontal velocity (v) needs to be approximated. After Svendsen (1987), TKE is calculated with:

$$k = \frac{1.33}{2}\left(\overline{u'^2} + \overline{w'^2}\right) \tag{3.20}$$

According to Svendsen (1987) this assumption should not give errors larger than $\pm 10\%$. Note that k here stands for TKE and k in for instance equation 3.2 stands for wave number, these are in no way related.

3.7.1 Magnitude, structure and pattern

In figures 3.23 and 3.24 the normalized TKE ($\sqrt{\frac{k}{gh}}$) is shown for Boers-1B and Boers-1C, respectively. The results of Boers-1B are of the same order of magnitude as values found by Ting (2001), who used irregular waves with $\xi_0 \approx 0.16$ on a plane sloping beach and research presented in Mocke (2001). Also, the vertical profile shows the same structure: largest near the surface and decreasing more or less linearly downwards. The TKE increases with decreasing water depth and increasing percentage of breaking waves –

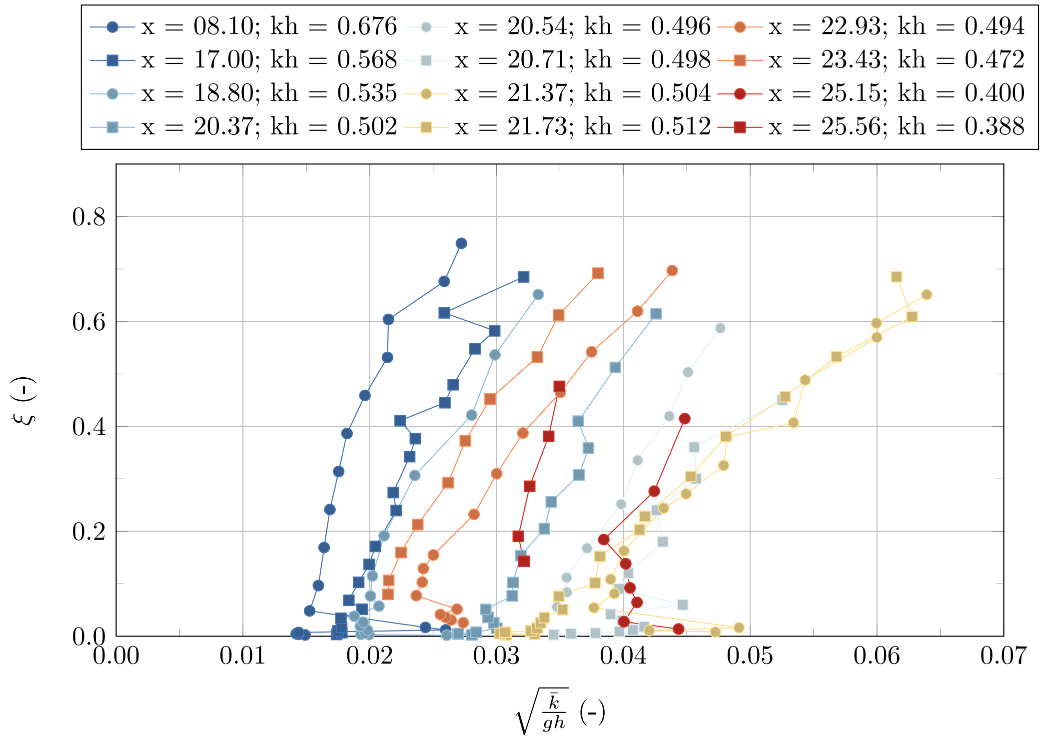

Figure 3.23: *Vertical distribution of turbulent kinetic energy for Boers-1B, spilling breakers*

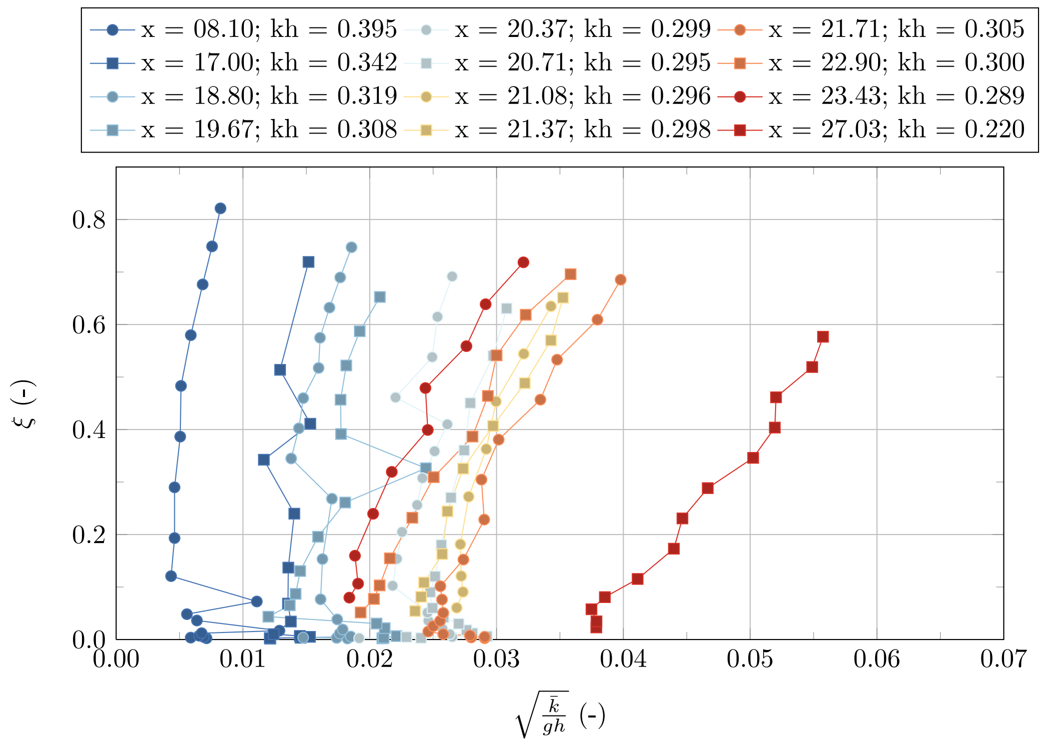

Figure 3.24: *Vertical distribution of turbulent kinetic energy for Boers-1C, weakly plunging breakers*

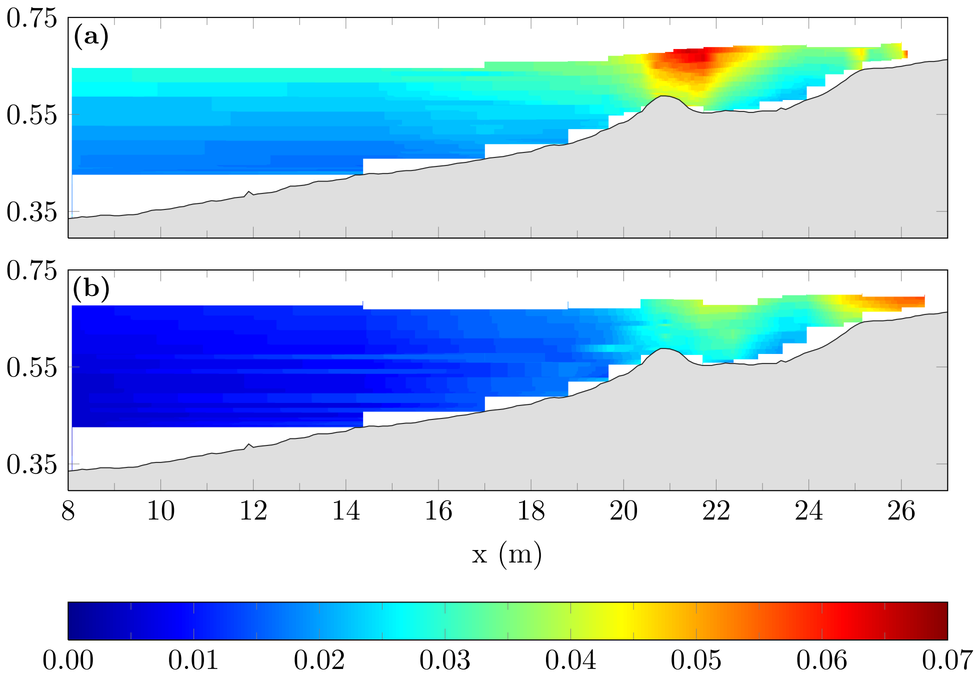

Figure 3.25: *Normalized turbulent kinetic energy ($\sqrt{\frac{k}{gh}}$) levels throughout the wave flume for (a) Boers-1B and (b) Boers-1C*

as found in Ting (2001) – until $x = 21.73\ m$. After that, different behaviour is found with respect to Ting (2001), the reason being the different bathymetry (plane slope vs. barred beach). Instead of continually increasing, TKE decreases in magnitude in the surf zone trough until $x = 23.95 - 24.35\ m$. From hereon shorewards, TKE increases again as the waves hit the second breaker bar. This pattern corresponds to the fraction of waves with a roller (figure 3.4), something which is to be expected since the rollers are the main producer of TKE. The highest values are therefore found in the higher water column. Since wave-induced turbulence is small (Ting & Kirby, 1994), turbulence levels decrease towards the bottom and are an effect of breaker-induced turbulence transported downwards.

The second turbulence producer is bottom friction, which becomes obvious through the higher turbulences levels at the bottom of the water column. This production is most obvious at locations were less wave breaking occurs, at breaker locations it seems to be dwarfed by turbulence transported down the water column from wave breaking. The only place this also seems to occur is with Govender (1999) as presented in Mocke (2001), most probably other research data is not detailed enough at the bottom.

Comparing figures 3.23 and 3.24 leads to the conclusion that plunging breakers (Boers-1C) show less vertical variation than spilling breakers (Boers-1B), which is in accordance with Ting and Kirby (1994). Turbulence levels for Boers-1C seem to be lower than for Boers-1B which is counter-intuitive since normally plunging breakers show heavier breaking and larger scale breaking processes. It is also different from findings by Ting and Kirby (1994). It should however be noted that relatively, the difference in wave height for the plunging breaker compared to spilling, is smaller for Ting and Kirby (1994) than Boers (2005). Which could possible explain the differences.

Table 3.2: *Comparison of Boers (2005) and Scott et al. (2005) research*

Parameter	Boers-1B	Scott et al. (2005)
ξ	0.31	0.35
kh	0.40 - 0.68	0.06 - 0.17

Table 3.3: *Comparison of Boers (2005) and Ting and Kirby (1996) research*

Parameter	Boers (2005)		Ting and Kirby (1996)	
Case	1B	1C	A	B
ξ	0.31	0.71	0.20	0.60

Scott et al. (2005) carried out turbulence measurements in a large-scale wave flume. Although the surf similarity parameter is of the same order as Boers-1B, the relative depths are completely different, see table 3.2. Thus, the case by Scott et al. (2005) is well into shallow water. There are some peculiar differences between the results. For instance, in the results of Scott et al. (2005) turbulence only penetrates to the bottom near the breaker bar. Both on- and offshore of this location turbulence levels at the bottom are negligible. For Boers-1B and Boers-1C turbulence levels at the bottom are, although lower than high in the water column, still considerable. Looking at Boers-1C, $x = 8.10$ m normalized TKE levels are around 0.1, even though no breaking is present at that location (this can also be seen by the uniform profile: no peak magnitude at water level which points to wave breaking). For this, two reasons can be given: (i) the presence of considerable background turbulence that could have affected the measurements; and (ii) the decomposing of turbulence from the main data, which could have lead to wrong turbulence levels, perhaps a result of the low amount of runs used for ensemble averaging or ensemble averaging itself, in which wave velocities are partly recorded as turbulence (Svendsen, 1987). The vertical profile shapes are also different with Scott et al. (2005) showing exponential profiles on- and offshore of the breaker bar where Boers (2005) shows linear ones over the whole wave flume. This is most probably an effect of small-scale measurements by Boers (2005).

3.7.2 Local anisotropy

The anisotropy of the turbulence was briefly considered by Boers (2005). Since then, some new research was published and therefore the conclusions of Boers (2005) are expanded. As stated before, equation 3.20 is based on research by Svendsen (1987) which assumes the flow acts like a plane wake in which the relative magnitudes relate to one another as $(\overline{u'^2} : \overline{w'^2} : \overline{v'^2})$ stands to $(0.42 : 0.32 : 0.26)$. Since $\overline{v'^2}$ is not known, only $\overline{u'^2}$ and $\overline{w'^2}$ can be compared. From the data above it is calculated that $\overline{w'^2}/\overline{u'^2} = 0.76$.

Figures 3.26 and 3.27 show the ratio between vertical and horizontal turbulence. Also the line $\overline{w'^2}/\overline{u'^2} = 0.76$ is plotted, from which the conclusion can be drawn that only the upper half of the water column is close to this value. The lower part shows considerably lower ratios ($\approx$0.2 at the bottom), which means that the vertical turbulence loses in importance compared to horizontal turbulence, thus turbulence becomes more anisotropic. The relative magnitudes become closer to that of the boundary layer (Svendsen, 1987), which clearly shows the influence of the bed on the flow. Similar

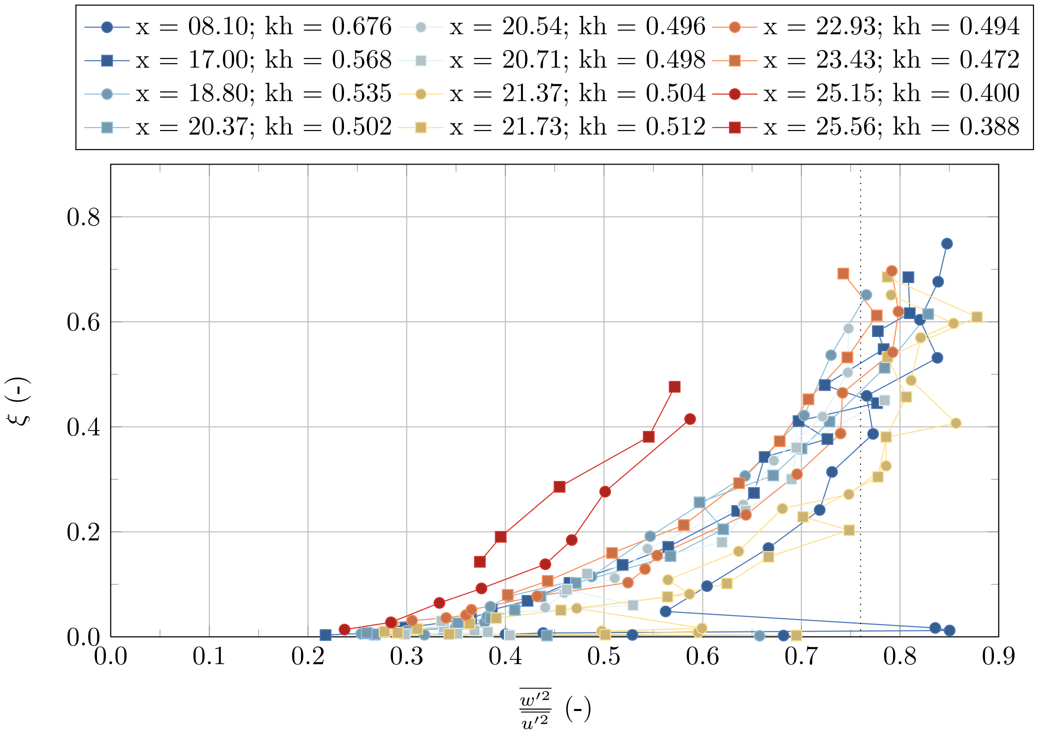

Figure 3.26: *Ratio between vertical and horizontal turbulence for Boers-1B*

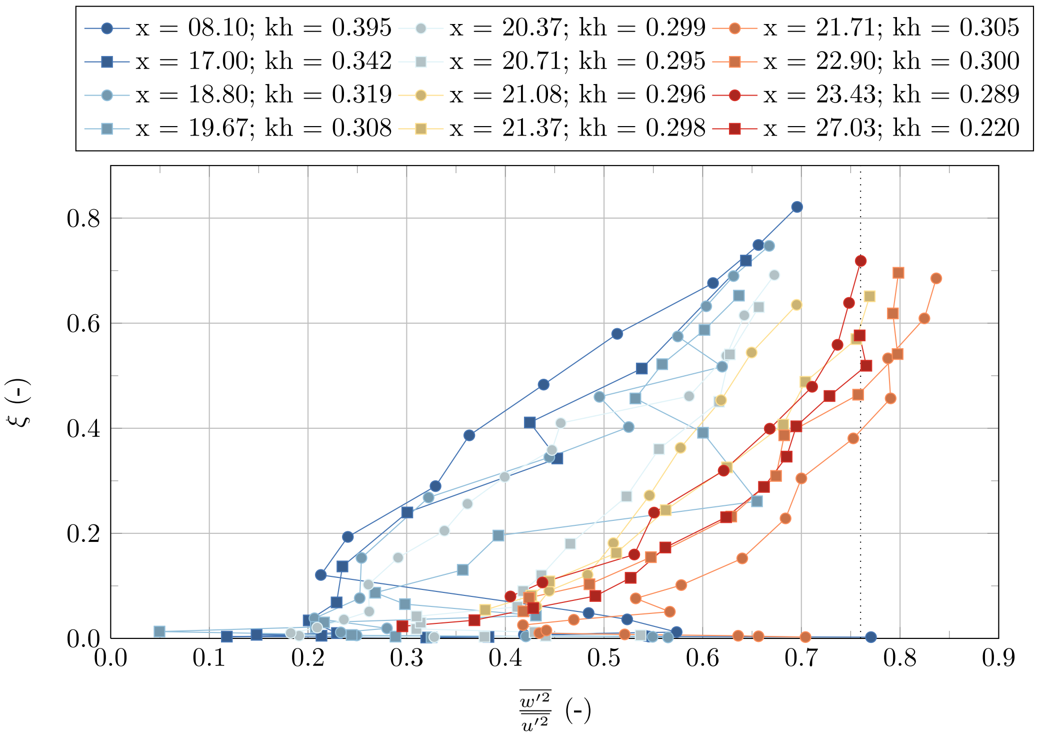

Figure 3.27: *Ratio between vertical and horizontal turbulence for Boers-1C*

results were also found by Scott et al. (2005) and Yoon and Cox (2010). Looking back at figures 3.7d and 3.8d one can see that vertical turbulence greatly decreases in magnitude towards the bottom where horizontal turbulence remains more stable through the water column. This results in a decreasing ratio as can be seen in both figures. Since the decrease of horizontal turbulence from the high water column towards the bottom is more extreme for Boers-1B than Boers-1C, the ratio remains higher in the upper water column for Boers-1B.

Comparing these figures to results by Ting and Kirby (1996) it is clear that both figures resemble the plunging case by Ting and Kirby (1996) (named TK96-B for convenience). This is odd, since Boers-1B is spilling and Boers-1C is only weakly plunging. Both TK96 cases are placed closer to spilling on the breaker type spectrum than Boers' cases, see table 3.3. However, even though TK96-A (spilling breaker) and Boers-1B are of a similar breaker type, the ratio looks completely different with a constant, uniform ratio and exponentially decreasing ratio, respectively. The uniform ratio suggests the breaker-produced vortex-like eddies are hardly affected by the bottom, where eddies produced in Boers-1B are broken down quickly because of the bottom influences (Ting & Kirby, 1996). Comparing TK96-B and Boers-1C differences are less pronounced but the ratio seems to decrease in a more linear fashion instead of an exponential one. Although it should be noted that this is less pronounced after the breaker bar, which is the only area plotted in Ting and Kirby (1996).

3.8 Conclusions

Useful data have been extracted from Boers (2005) measurements by means of Reynolds decomposition and ensemble averaging. Since data gathered above wave trough showed doubtful results, this part of the water column was disregarded. Depth-dependent radiation stress profiles between bed and wave trough were calculated by a method presented in Stive and Wind (1982).

The profiles below wave trough can be considered to be fairly uniform on most locations, with the exception of the bottom boundary layer (BBL) near the breaker bar. Profiles for Boers-1C (weakly plunging breakers) are more uniform than Boers-1B (spilling breakers), but this was found to be related to a shallower relative depth and is not considered an explicit effect of breaker type. Horizontal wave contribution ($\rho\overline{\tilde{u}^2}$) for depth-dependent radiation stress is dominant on all locations, and turbulent contribution ($\rho\overline{u'^2} - \rho\overline{w'^2}$) remains below 10%, even near the breaker bars. Although measurements were relatively detailed, wave force patterns are still crude because of the derivative that is involved. Therefore, only the area near the breaker bar is considered where measurement density is highest. Wave force profiles were mostly uniform over depth, with the exception of the BBL at the breaker bar.

Mean-flow Reynolds stresses were found, although this is impossible in a wave flume since $\bar{w}$ needs to be zero as expected from literature and theory. Therefore, it is assumed that they are the result of measurement, device calibration, or decomposing errors. Non-zero values for the wave Reynolds stress were found throughout the water column. The vertical profile of wave Reynolds stresses can best be described as a trapezium, with largest values near the bottom and zero at the bed. This is not what was expected from chapter 2. Turbulent Reynolds stresses show a triangular shape with the maximum values at the water surface and zero or near zero at the bottom. This is in agreement with both laboratory and field observations, and is what was expected from literature.

Reynolds stresses were found to produce a comparable, but opposite, forcing as depth-dependent radiation stress above the BBL. Thus, they mostly cancel each other out. Inside the BBL Reynolds stresses dominated the forcing, where the wave Reynolds stress was found to be the dominant component.

Turbulent kinetic energy shows a linear profile with a maximum at water level where wave breaking is the main turbulence producer. Also for TKE, plunging breakers show greater uniformity over water depth. This corresponds to other research, notably Ting and Kirby (1994, 1995, 1996) where also similar magnitudes were found. Differences found can be explained by the use of a barred beach and irregular waves. Between the small-scale Boers (2005) and large-scale Scott et al. (2005) measurements differences are found in turbulence penetration and thus the vertical profile of TKE. Possible explanations are difference in scale and problems with determining turbulence for Boers (2005). Furthermore, it became clear turbulence is highly anisotropic in the lower half of the water column. Expected differences between spilling and plunging breakers are not obvious when considering anisotropy of turbulence.

Also other differences between breaker types are not clear from this data analysis. Lower values for pretty much any hydrodynamic property seem to be related to wave height rather than breaker type. One would expect an increasing importance of turbulence for plunging breakers (Boers-1C), but the opposite is true for this data analysis. Looking at wave height it becomes clear that energy dissipation by wave breaking after the first breaker bar is significantly larger for Boers-1B than Boers-1C where the drop in wave height is only minor. From thereon wave heights are close to one-another and breaking has the same intensity and hence, hydrodynamic properties are more similar.

From the data analysis it became clear Boers' data shows good agreement with previous research, but that there are also some differences to be found. For instance, some differences can be explained by bathymetry: using a plane sloping or natural profile seems to affect quite some hydrodynamic processes, this could be related to change of sign (wave Reynolds stress) or difference in magnitude (wave forces, turbulence). It seems therefore important to use a natural profile and irregular waves in laboratory environments to achieve a good representation of reality.

Measured depth-dependent radiation stress and wave force profiles were compared to analytical formulations. M08 gives better results than LHS for depth-dependent radiation stresses below wave trough in the surf zone. For wave forces it was not possible to determine which formulation gave the best results. Since depth-dependence of radiation stresses in the surf zone is negligible, the improvements are considered to be a result of the E_D term, representing the radiation stress above wave trough level. With M08 this component is considered separately, where for LHS it is divided over depth. Since this E_D is not specific for M08 but is also included in LHS, a simple separation of LHS-components could give the same results as implementing M08 in a numerical model, when considering modelling the surf zone.

Measured wave Reynolds stresses were compared to an analytical equation by Zou et al. (2006). Above the BBL this equation approximated measurement well for both Boers-1B and Boers-1C.

Chapter 4

Review of modelling formulations

For coastal processes, the mean-flow is often the most important parameter for mid- and long-term calculations. For this reason, coastal models solve the time-averaged Navier-Stokes equation as shown in section 2.3. One of the most common coastal flow models is Delft3D, which is used in both engineering applications and scientific research. This thesis will also make use of Delft3D.

This chapter presents a literature study into the modelling formulations of Delft3D. The objective is thus to get an understanding of the modelling capabilities of Delft3D when it comes to modelling mean-flow dynamics. Furthermore, understanding modelling formulations will help with the analysis of its output in chapter 5. First, wave-drivers are discussed in section 4.1, Delft3D-FLOW in section 4.2 and conclusions can be found in section 4.3.

4.1 Wave-drivers

Delft3D is organized in two parts: a wave-driver and the flow calculation part. In section 2.3, it also became clear that this mean-flow is forced by both waves and turbulence, which need to be known before any meaningful calculation can be made. Coastal flow models do not have the capability to calculate wave parameters like radiation stress, since short-wave motions are not included in the models. Therefore, wave-drivers are used to calculate wave forcing.

Roelvink and Reniers (2012) give three different types of wave-drivers: (i) wave-averaged; (ii) short wave-averaged; and (iii) short wave-resolving. Wave-averaged models average over both short waves and wave groups – if wave groups are considered at all; short wave-averaged only average over short waves, but are wave group resolving; and short wave resolving do not average at all, and can also calculate wave properties like wave skewness and asymmetry. Obviously, the more information that is calculated, the more computational power that is required.

4.1.1 Roller model

The roller model (included in Delft3D-FLOW) is a limited wave-driver that is used to calculate the effects of short waves on long waves and is thus short wave-averaged. Furthermore, the roller model can only be used for narrow-banded wave spectra for both direction and frequency. The roller model adds the surface roller as discussed in section 2.2.4 to Delft3D-FLOW by incorporating it in the energy balance and radiation stress following Nairn, Roelvink, and Southgate (1990). The roller model calculates wave forces based on radiation stress with the equation of Longuet-Higgens and Stewart (1964) (equation 4.1).

$$S_{xx} = \underbrace{\left(\frac{c_g}{c}\left(1+\cos^2(\alpha)\right)-\frac{1}{2}\right)E}_{\text{Longuet-Higgens and Stewart (1964)}} + \underbrace{2\cos^2(\alpha)E_r}_{\text{Nairn et al. (1990)}} \tag{4.1}$$

where c_g is group velocity (ms^{-1}); c is wave velocity (ms^{-1}); α is wave direction (rad); E is wave energy (Nm^{-1}); and E_r is roller energy (Nm^{-1}), which is based on an energy balance. The wave (body) forces are then calculated according to equation 4.2a (y-direction is assumed to be uniform, ie. $\partial/\partial y = 0$):

$$F_w = -\frac{\partial S_{xx}}{\partial x} - F_r \tag{4.2a}$$

$$F_r = \frac{D_r}{c}\cos(\alpha) \tag{4.2b}$$

$$D_r = 2\beta g\frac{E_r}{c} \tag{4.2c}$$

where F_r is the roller force; D_r is roller energy dissipation, which is also calculated by the roller model; and β is a user-defined coefficient of approximately 0.1.

4.1.2 TRITON

TRITON is a 2DH (depth-averaged) short wave-resolving Boussinesq-type wave model (Borsboom, Doorn, Groeneweg, & Van Gent, 2000, 2001; Groeneweg, Doorn, Borsboom, & van Gent, 2002) which was coupled to Delft3D by Wenneker et al. (2011). A Boussinesq-type wave model is computational expensive and can only be used for small time and spatial domains. The reason to accept larger modelling times is because Boussinesq-type models are better in modelling non-linear effects – of which wave breaking is an important example. TRITON calculates wave (body) forces as follows (see Wenneker et al. (2011) for full explanation):

$$F_w = \rho\bar{H}\left(\frac{\partial\hat{u}}{\partial t} + (\hat{u}\nabla)\,\hat{u} + g\nabla\bar{\zeta}\right) \tag{4.3}$$

where $\bar{H}$ is wave-averaged water depth (m); $\hat{u}$ is depth-averaged velocity (ms^{-1}); ∇ is horizontal gradient operator ($\partial/\partial x, \partial/\partial y$); and $\bar{\zeta}$ is mean water level (m). Roller energy in TRITON is related to roller area following Svendsen (1984b). The roller force is then calculated following the same manner as the roller model, but giving a slightly different outcome:

$$F_r = \rho g\sin\beta\cdot\overline{\delta} \tag{4.4}$$

where $\sin\beta$ is the slope of the wave front, comparable to the user-defined β for the roller model; and $\overline{\delta}$ is the phase-averaged roller thickness.

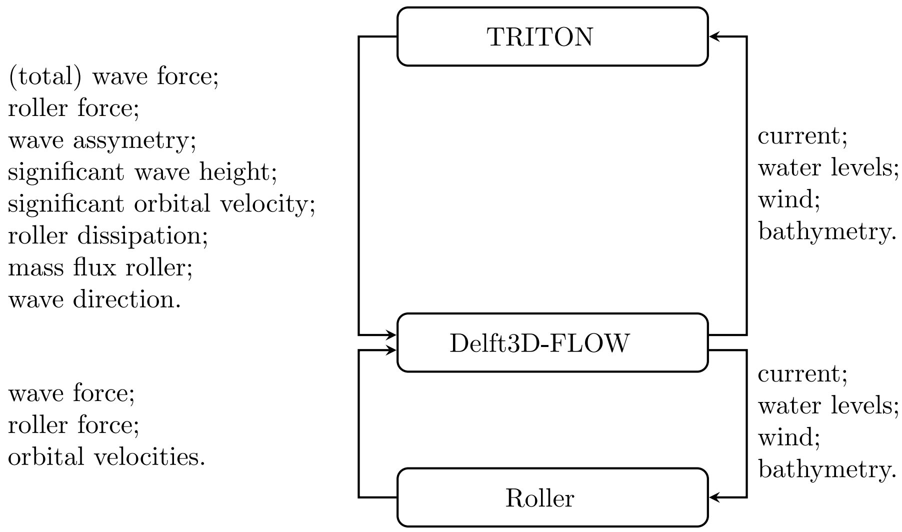

Figure 4.1: *Communication of results between wave-drivers and Delft3D-FLOW (Wenneker et al., 2011; Deltares, 2012)*

4.1.3 Communication

As mentioned earlier, information needs to be shared between the wave-driver and flow module. When running Delft3D, it will be done online, meaning that the wave-driver runs parallel to Delft3D-FLOW and information is shared constantly. The communication between wave-driver and Delft3D-FLOW is done through a so called communication file, which is then imported into Delft3D-FLOW. The communication is visualised in figure 4.1.

4.2 Delft3D-FLOW

Delft3D-FLOW is a wave-averaged hydrostatic flow model, for a detailed explanation of its working, please consult Lesser, Roelvink, van Kester, and Stelling (2004), Lesser (2009), and Deltares (2012).

4.2.1 Generalised Lagrangian Mean

Until now, the decomposition of flow into mean, wave, and turbulent parts was presented as a simple operation. However, in reality, it is a difficult one, since fluid particles do not move in straight lines (Eulerian point of view) but rather in complicated paths (Lagrangian point of view). In order to improve calculations the so called Generalised Lagrangian Mean (GLM) method was implemented in Delft3D, which is a hybrid Eulerian-Langrangian approach (Walstra, Roelvink, & Groeneweg, 2000). GLM-velocities are calculated following:

$$U = u + u_s \tag{4.5}$$

where U is cross-shore, horizontal GLM velocity (ms^{-1}); u is Eulerian velocity (ms^{-1}); and u_s is Stokes' drift (ms^{-1}). Full explanation of GLM is outside the scope of this thesis, more general information about GLM can be found in Groeneweg (1999) and for its implementation in Delft3D, see Walstra et al. (2000).

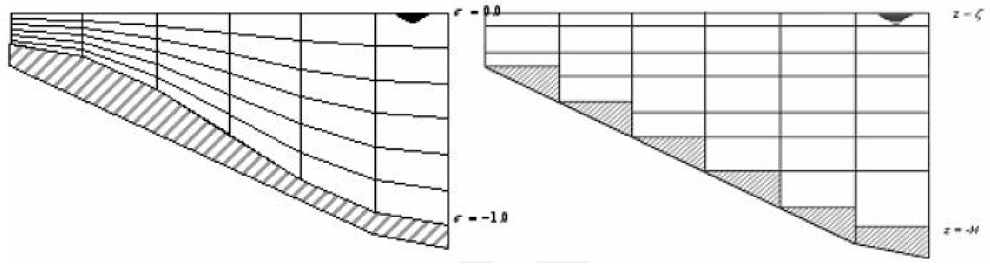

Figure 4.2: *Sigma-layers (left) compared to z-layers (right) (Deltares, 2012)*

4.2.2 Shallow-water equations

Delft3D-FLOW solves the unsteady shallow-water equations in two (depth-averaged) or three dimensions (Lesser et al., 2004). The used equations include: continuity (equation 4.6), horizontal momentum (equation 4.7, only x-direction is shown), and turbulence closure model (see section 4.2.4).

$$\frac{\partial \zeta}{\partial t} + \frac{\partial (d+\zeta)u}{\partial x} + \frac{\partial (d+\zeta)v}{\partial y} + \frac{\partial \omega}{\partial \sigma} = (d+\zeta)(q_{in} - q_{out}) \tag{4.6}$$

$$\begin{aligned} &\overbrace{\frac{\partial u}{\partial t}}^{(1)} + \overbrace{u\frac{\partial u}{\partial x} + v\frac{\partial u}{\partial y}}^{(2a)} + \overbrace{\frac{w}{d+\zeta}\frac{\partial u}{\partial \sigma}}^{(2b)} - \overbrace{fv}^{(3)} = \\ &-\underbrace{g\frac{\partial \zeta}{\partial x}}_{(4)} + \underbrace{\nu_H\left(\frac{\partial^2 u}{\partial x^2} + \frac{\partial^2 v}{\partial y^2}\right)}_{(5)} + \underbrace{\frac{1}{(d+\zeta)^2}\frac{\partial}{\partial \sigma}\left(\nu_t^{3D}\frac{\partial u}{\partial \sigma}\right)}_{(6)} + \underbrace{M_x}_{(7)} \end{aligned} \tag{4.7}$$

where the right hand side of equation 4.6 represents a sink or source term. In equation 4.7, component one is unsteady acceleration; component two represents convective acceleration; component three is Coriolis force; component four is pressure term; component five represents the imbalance of horizontal Reynolds stresses; component six represents the turbulence closure model; and component seven represents contributions due to external sources or sinks of momentum, wave effects – for instance wave forces – are calculated by the wave driver and therefore considered external by Delft3D-FLOW (Deltares, 2012). Delft3D-FLOW uses the σ-coordinate system for its calculations. The σ-coordinate scales with depth, such that the bottom is always at $\sigma = -1$ and the water level is at $\sigma = 0$ (figure 4.2). The transformation from z-coordinate (location in physical space) to σ is as follows (Mooiman, 2012):

$$\sigma = \frac{z - \zeta}{d + \zeta} \tag{4.8}$$

where z is the vertical coordinate in physical space (m); ζ is free surface elevation above the reference plane (m); and d is depth below reference plane (m).

Because of the shallow water assumption made in Delft3D-FLOW, the vertical momentum equation is reduced to hydrostatic pressure (equation 4.9), disregarding vertical accelerations. This is acceptable in coastal areas, where vertical accelerations are assumed to be small and thus hydrodynamic pressure is negligible (Deltares, 2012).

$$\frac{\partial P}{\partial \sigma} = -\rho g h \tag{4.9}$$

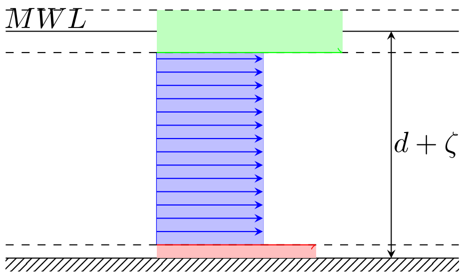

Figure 4.3: *Three-layer concept as applied for wave forcing*

4.2.3 Wave influences

Three-layer concept

De Vriend and Stive (1987) divide the water column into three different parts: (i) the surface layer, wave trough to crest; (ii) centre layer, below wave trough and above bottom boundary layer; and (iii) bottom boundary layer. Delft3D-FLOW also carries out this procedure (see figure 4.3). The division is based on the fact that different processes occur on different locations in the water column and the RANS-equation is not valid above wave trough level, as explained in appendix A. For instance, mass flux and wave breaking only occur in the surface layer, where forcing due to wave Reynolds stresses and sediment transport mainly occur in the bottom boundary layer (Arcilla, 1989).

The surface layer – in which the wave forcing due to breaking originates – is modelled as a shear stress at the top of the centre layer (Lesser et al., 2004). This is based on work by Stive and Wind (1986) who applied it as a boundary condition in order to determine the undertow. The region between wave trough and crest is thus not modelled itself, but the effects on the water column can be calculated nonetheless, compensating for momentum decay above trough level, as well as mass flux. Note that when wave-averaging the centre layer is extended to mean water level (Svendsen, 2006). As will be discussed in section 4.2.3 wave forces are distributed over the centre layer. The bottom layer is the area were streaming takes place, which is added as an additional shear stress acting across the thickness of bottom wave boundary layers. Other bottom processes are also modelled in this area.

Wave and roller forces

The wave and roller forces are communicated from the wave-driver to Delft3D-FLOW, as explained in section 4.1. In Delft3D-FLOW the roller force is applied as a shear stress at mean water level, thus at the top of the centre region in figure 4.3. The wave (body) force is assumed to be uniform over depth and is distributed accordingly over the water column. Note that the procedure for wave forces is different when SWAN is used as a wave-driver. First of all, SWAN gives the option to calculate wave forcing based on dissipation to reduce spurious currents. Second, SWAN gives to option to separate the forcing components into parts applied at the top or bottom of the water column (Lesser, 2009). These options are not available for the roller model or TRITON.

Wave Reynolds stress

The wave Reynolds stress is considered only through the effect of streaming. Wave Reynolds stresses above the bottom boundary layer are not considered in Delft3D-FLOW and they are only calculated in the bottom boundary layer ($d + \zeta - \delta \leq z \leq d + \zeta$) with the following equation (see Deltares (2012) and Walstra et al. (2000)):

$$\frac{\partial \overline{\tilde{u}\tilde{w}}}{\partial z} = -\frac{D_f k \cos\phi}{\omega\delta}\left(1 - \frac{d + \zeta - z'}{\delta}\right) \tag{4.10}$$

4.2.4 Turbulence and eddy viscosity

Turbulence occurs 'sub-grid' (meaning the space and time grid is too coarse (Deltares, 2012)) and can thus not be solved in numerical models. Because of this turbulence closure problem, the Boussinesq hypothesis (equation 4.11) is introduced in order to solve the RANS-equation (2.5a). This hypothesis states that turbulence can be modelled as being an additional viscosity and introduces the concept of eddy viscosity (ν_t), which was already briefly discussed in section 2.3.2 and showed up in equation 4.7.

$$\tau'_{ij} = -\rho\overline{u'_j u'_i} = \rho\nu_t\left(\frac{\partial u_i}{\partial x_j} + \frac{\partial u_j}{\partial x_i}\right) \tag{4.11}$$

In order to determine the magnitude of the eddy viscosity, a turbulence model is needed. The $k - \epsilon$ model (Jones & Launder, 1972) is among the four closure models available in Delft3D and arguably the most used. The other available models are constant coefficient, the algebraic eddy viscosity closure model and the $k - L$ model. The k stands for turbulent kinetic energy (TKE) and ϵ for energy dissipation. In order to calculate eddy viscosity, TKE and dissipation need to be known (equation 4.12) (Wilcox, 1993).

$$\nu_t = c_\mu \frac{k^2}{\epsilon} \tag{4.12}$$

where c_μ is a calibration coefficient. The full $k - \epsilon$ model equations are obtained from the Navier-Stokes equation with a closure hypotheses for turbulent diffusion, production and dissipation (Arcilla, 1989) and are given by:

$$\underbrace{\frac{\partial k}{\partial t}}_{(1)} + \underbrace{u\frac{\partial k}{\partial x} + v\frac{\partial k}{\partial y} + \frac{\omega}{d+\zeta}\frac{\partial k}{\partial \sigma}}_{(2)} = \underbrace{\frac{1}{(d+\zeta)^2}\frac{\partial}{\partial \sigma}\left(D_k\frac{\partial k}{\partial \sigma}\right)}_{(3)} + \underbrace{P_k}_{(4a)} + \underbrace{P_{kw}}_{(4b)} + \underbrace{B_k}_{(5)} - \underbrace{\epsilon}_{(6)} \tag{4.13a}$$

$$\underbrace{\frac{\partial \epsilon}{\partial t}}_{(1)} + \underbrace{u\frac{\partial \epsilon}{\partial x} + v\frac{\partial \epsilon}{\partial y} + \frac{\omega}{d+\zeta}\frac{\partial \epsilon}{\partial \sigma}}_{(2)} = \underbrace{\frac{1}{(d+\zeta)^2}\frac{\partial}{\partial \sigma}\left(D_\epsilon\frac{\partial \epsilon}{\partial \sigma}\right)}_{(3)} + \underbrace{P_\epsilon}_{(4a)} + \underbrace{P_{\epsilon w}}_{(4b)} + \underbrace{B_\epsilon}_{(5)} - \underbrace{c_{2\epsilon}\frac{\epsilon^2}{k}}_{(6)} \tag{4.13b}$$

$$D_k = \frac{\nu_{mol}}{\sigma_{mol}} + \frac{\nu_{3D}}{\sigma_k} \tag{4.14a}$$

$$D_\epsilon = \frac{\nu_{3D}}{\sigma_\epsilon} \tag{4.14b}$$

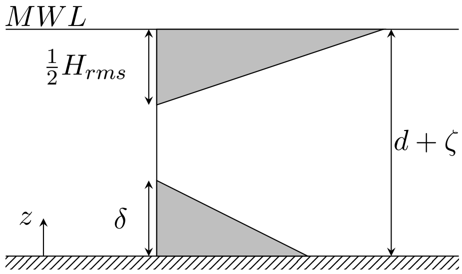

Figure 4.4: *Vertical distribution of turbulent kinetic energy production (Walstra et al., 2000)*

where for both equations 4.13a and 4.13b term one is the local derivative; term two represents advection; term three is the combination of viscous and diffusive transport; term four are production terms, where 4b is induced by waves, shown in equations 4.15, 4.16a, 4.16b and 4.17, also see figure 4.4 (Walstra et al., 2000); term five is bouyancy; and term six is a sink term. σ in equations 4.14a and 4.14b stands for the Prandtl-Schmidt number, which in the case of the $k-\epsilon$ model is 1 for k and 1.3 for ϵ.

$$P_k = \nu_{3D}\frac{1}{(d+\zeta)^2}\left[\left(\frac{\partial u}{\partial\sigma}\right)^2\left(\frac{\partial v}{\partial\sigma}\right)^2\right] \tag{4.15}$$

$$P_kw(z') = \frac{4D_w}{H_{rms}}\left(1-\frac{2z'}{H_{rms}}\right) \qquad \text{for } z' \qquad \leq \frac{1}{2}H_{rms} \tag{4.16a}$$

$$P_kw(z') = \frac{2D_f}{\delta}\left(1-\frac{d+\bar{\zeta}-z'}{\delta}\right) \qquad \text{for } d+\bar{\zeta}-\delta \qquad \leq d+\bar{\zeta} \tag{4.16b}$$

where δ is bottom boundary layer thickness.

$$P_\epsilon(z') = c_{1\epsilon}\frac{\epsilon}{k}P_k(z') \tag{4.17}$$

where $c_{1\epsilon}$ is a calibration constant of around 1.44.

The $k-\epsilon$ model only calculates the so called 3D turbulence, which assumes isotropic distribution. From the data analysis (section 3.7.2) it became clear that horizontal turbulence is larger than the vertical component and turbulence is thus not isotropic. The same is true for eddy viscosities and Delft3D copes with this by assuming horizontal viscosity is the sum of (i) molecular viscosity, (ii) 2D-viscosity, and (iii) 3D-viscosity (Deltares, 2012). Where the 2D-viscosity is assumed to occur on sub-grid scale (SGS) which is computed by a Horizontal Large Eddy simulation (HLES) and subsequent SGS-turbulence model. 3D-viscosity is calculated by the turbulence closure model. A possible background eddy viscosity is defined by user-input.

$$\nu_H = \nu_{SGS} + \nu_{3D} + \nu_H^{back} \tag{4.18a}$$

$$\nu_V = \nu_{mol} + max(\nu_V^{back}, \nu_{3D}) \tag{4.18b}$$

4.3 Conclusions

In this chapter the modelling formulations from TRITON, roller model and Delft3D-FLOW have been reviewed. The roller model – a phase-averaged wave-driver – calculates wave forces based on radiation stress with Longuet-Higgens and Stewart (1964) with an additional roller contribution. TRITON – a phase-resolving wave-driver – calculates wave force slightly different, but the basics are the same. The wave-drivers run online, which means they run at the same time as Delft3D-FLOW and constantly share information. Especially TRITON shares a lot of information with FLOW, for the roller model this is only the wave forces, roller force, and orbital velocities.

Delft3D-FLOW is a phase-averaged hydrostatic flow model and thus solves the shallow-water equations. This is done in a Generalised Lagrangian Mean reference frame to improve calculations. It uses a three-layer concept of which the influences of the surface and bottom layers on the centre part is taken into account with shear stresses at respectively top and bottom of this centre layer. Wave forces are calculated by the wave drivers and inserted into the momentum equation as an external source. The wave force is assumed uniform over depth, and distributed accordingly. The roller force is applied as a shear stress at meant water level. The wave Reynolds stress is only considered in the bottom boundary layer, and is thus disregarded in the remaining water column.

Turbulence is taken into account with the Boussinesq-approximation and is thus modelled as an additional viscosity. In the process, eddy viscosity is introduced which is calculated with the $k-\epsilon$ model. Two producers of turbulent kinetic energy are assumed, wave breaking at the top of the water column and bottom friction at the bottom of the water column.

Chapter 5

Model validation & assessment

This chapter is about the validation of the model results compared to data extracted from Boers (2005). We have validated wave forces, roller forces, turbulent kinetic energy, and undertow. On top of that, the differences between using a phase-averaged and phase-resolving wave driver will be assessed. The objective of this chapter is thus two-fold:

1. to assess how well the wave-averaged Delft3D-model is able to simulate mean-flow dynamics;
2. to assess what the differences are in output between using a phase-averaged or phase-resolving wave-driver.

The chapter starts with the model set-up in Delft3D (section 5.1). Then the model calibration and errors found in the roller model are discussed (section 5.2). The validation can be found in section 5.3 and assessment of the results is found in section 5.4. The chapter ends with conclusions in section 5.5.

5.1 Model set-up

5.1.1 Computational grid

The grid used by Delft3D consists of 152 m-locations (cross-shore); 4 n-locations (along-shore); and 15 k-locations (vertical). Note that this is more than visible in the grid; this is related to numerical calculations. The horizontal grid is shown in figure 5.1 (top) and is spaced 0.2 m in x-direction and 5 m in y-direction. The vertical profile (figure 5.1 (bottom)) consists of σ-layers, as discussed in section 4.2.2. The layers are spaced as follows, from bottom to top: 2%, 3%, 4%, 6%, 8%, 10%, 11%, 12%, 11%, 10%, 8%, 6%, 4%, 3%, 2%.

5.1.2 Initial and boundary conditions

The initial condition consists of the water level only, which is set at 0 m (so at 0.75 m in y-coordinates). On the offshore boundary, the water level is set as harmonic boundary condition with 0 m amplitude and 0 phase at both begin and end; so it does not change in time. The reflection parameter α is set to 100 s^2. The boundaries perpendicular to the coast are set as harmonic Neumann boundary conditions, also here the amplitude and phase are set to 0 at both beginning and end.

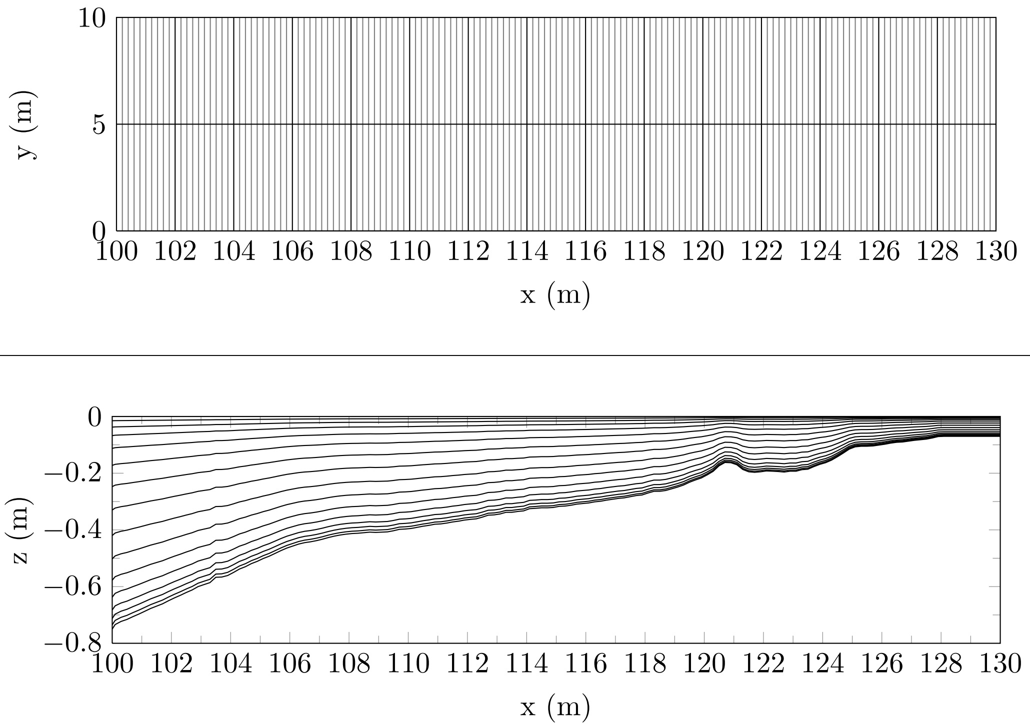

Figure 5.1: *Horizontal (top) and vertical (bottom) grids as used in Delft3D. Only separation of σ-layers is shown in vertical grid.*

5.1.3 Wave and parameter settings

The wave settings for the roller model are defined in the wavecon-file. For both Boers-1B and Boers-1C the direction of the waves is set at 270°, meaning they come from the left. For Boers-1B the wave height is 0.206 m with a period of 2.03 s; for Boers-1C this is 0.103 m and 3.33 s, respectively. In TRITON waves are created by applying a time-series at the offshore boundary, this time-series is taken from the Boers (2005) measurements. As a result, it can thus model an irregular wave-series.

Most parameter setting is left unchanged from those used in Wenneker et al. (2011); and are shown in table 5.1. The exception is the saving of data time-steps Δt_{map} and Δt_{his}, which are reduced tenfold. This is possible since we are modelling a small case with limited time span.

5.2 Calibration

Delft3D-FLOW is used in combination with two different wave drives: the roller model and TRITON. All have been discussed in chapter 4. The coupled systems will be named as follows: Roller-FLOW for the coupled system of the roller model and Delft3D-FLOW; and TRITON-FLOW for TRITON combined with Delft3D-FLOW.

5.2.1 Roller model

The roller model has been calibrated first on wave height and second on setup/setdown. This is done by changing five parameters, as shown in table 5.2. The effects of the

Table 5.1: *Model settings Delft3D-FLOW and TRITON*

Parameter	Description	Boers-1B	Boers-1C
	Delft3D-FLOW / roller model		
Δx_{D3D}	grid cell size (m)	0.2	0.2
Δt_{D3D}	time step (s)	0.6	0.6
Δt_{map}	time step map file (s)	3	3
Δt_{his}	time step history file (s)	0.6	0.6
	TRITON		
Δx_T	grid cell size (m)	0.05	0.05
Δt_T	time step (s)	0.025	0.025

Table 5.2: *Calibration parameters for roller model*

Parameter	Description	Boers-1B	Boers-1C
$ALFAC$	wave dissipation factor	0.8	0.9
$GAMMA$	wave breaking parameter	0.75	-
$BETD$	slope of wave front	0.1	0.1
$FWEE$	bottom friction factor	0.1	0.04
$FLAM$	breaker delay in wave lengths	-1.5	-1.5

different parameters are shown in Walstra (2000). For wave height, the results are shown in figure 5.2. Especially Boers-1B showed some problematic areas to reproduce: the start of the wave flume, where breaking does not start as soon as for measurements; and near the breaker bar, where the sudden drop in wave height is difficult to reproduce. Boers-1C is better approximated and shows no large problems.

Inspection of roller model output brought to light that wave forces were put to zero and thus absent from the results (also see Van der Weerd (2012)). This meant setdown was missing in the output, setup still occurred as a result of roller forces. After wave forces were inserted into a test model, setdown did occur, but at the offshore boundary an offset of the water level of a couple of millimetres was seen in the model output, see figure 5.3. This should be impossible since normally the boundary condition forces the water level to be zero; the hypothesis is that a non-zero wave force at the offshore boundary causes the problems. Because of time-constraints, this could not be addressed in time. However, we hypothesise that this offset has minor influences on the output and the model is still useful. In order to see if this is correct, the offset is assessed before proceeding with the model validation.

In order to simulate the effects of the offset in Delft3D, the fully tested old model (so no wave forces) is used twice: the first time with normal settings and the second time with an increased water depth of 6 mm – all other settings remain unchanged. Wave height influences many hydrodynamic phenomena and is thus important to assess, furthermore the phenomena used in the validation will also be checked, so roller force, turbulent kinetic energy, and undertow. The effects of the offset are shown in figure 5.4. For all the considered hydrodynamic phenomena, the influences by the water level offset are minor. Therefore it is assumed that the offset created by wave forces has a negligible

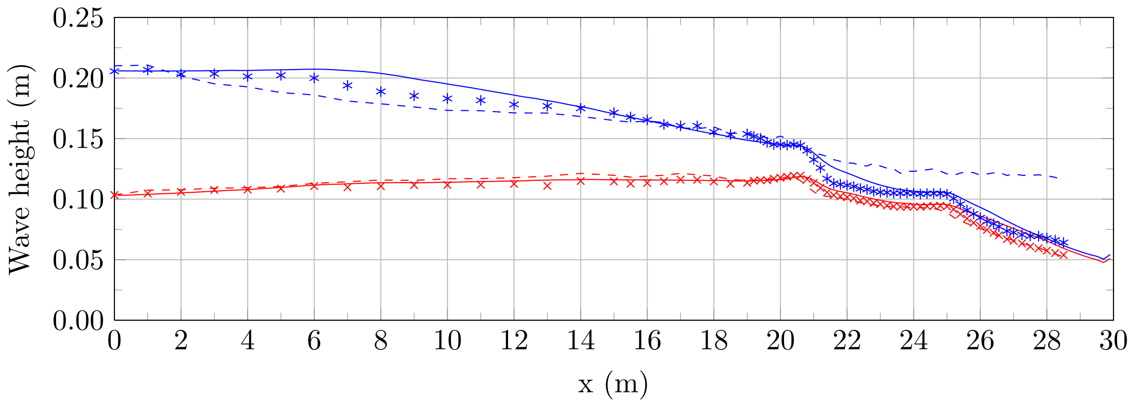

Figure 5.2: *Results of wave height calibration (blue is Boers-1B, red is Boers-1C) for both roller model (solid) and TRITON (dashed), compared to measured values (marks)*

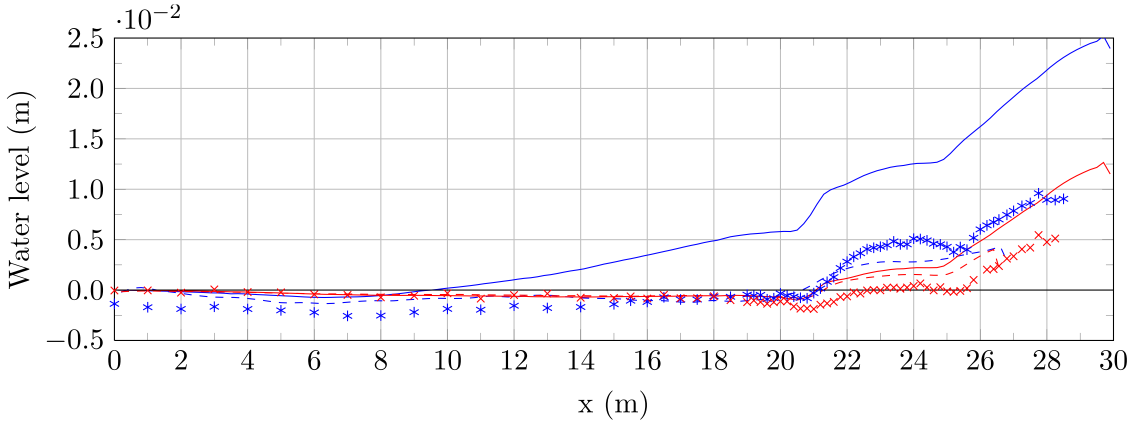

Figure 5.3: *Results of water level calibration (blue is Boers-1B, red is Boers-1C) for both roller model (solid) and TRITON (dashed), compared to measured values (marks). A correction for the offset has been applied to set the offshore boundary to 0. Correction for Boers-1B was 3.2 mm, for Boers-1C 7.3 mm.*

influence on the output.

5.2.2 TRITON

In the paper by Wenneker et al. (2011) two closure hypotheses were tested for the relation between roller thickness as computed by TRITON and actual roller thickness. The first hypothesis is a linear relationship between δ (actual roller thickness) and δ^* (roller thickness by TRITON) (equation 5.1) and the second is a breaker delay hypothesis (equation 5.2). The results from the different hypotheses was that for Boers-1B the best results for undertow were obtained with breaker delay and $f_\delta = 7.5$ and for Boers-1C with breaker delay and $f_\delta = 2.5$. These are also the settings that will be used in this validation.

$$\delta = f_\delta \delta^* \tag{5.1}$$

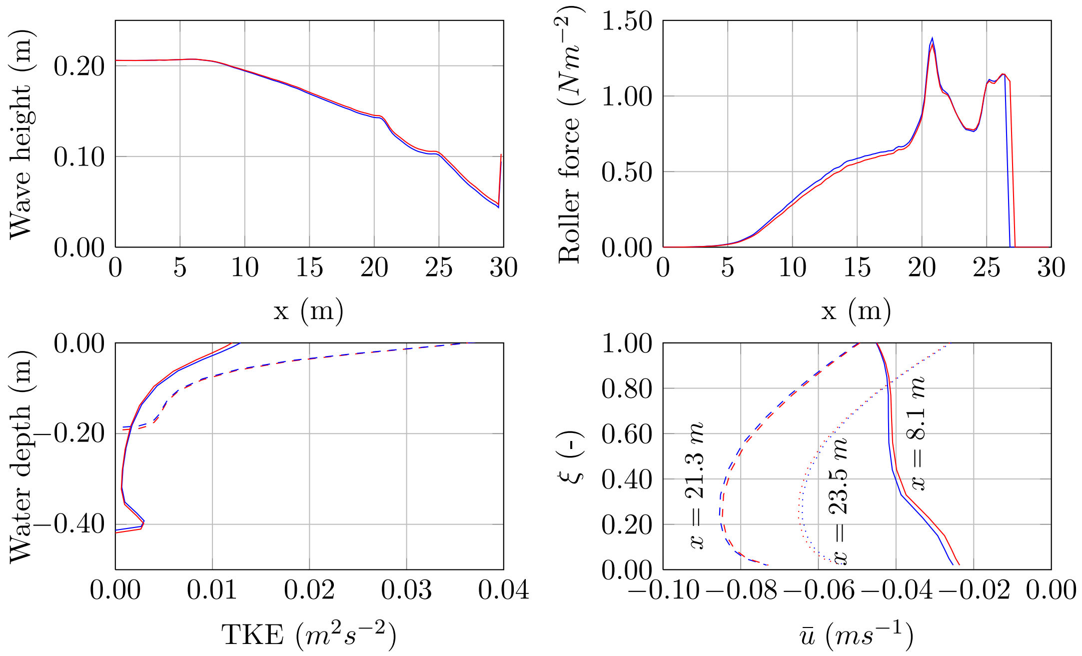

Figure 5.4: *Differences in wave height, roller force, turbulent kinetic energy, and undertow for no offset (blue) and an offset of 6 mm (red).*

$$\delta(x) = f_\delta \frac{1}{L_{delay}} \int_{x-L_{delay}}^{x} \delta^*(s)\,\mathrm{d}s \tag{5.2}$$

$$L_{delay}(x) = \sqrt{gh(x)}T_{sw} \tag{5.3}$$

where L_{delay} is a measure for the length over which the delay takes place and is calculated with equation 5.3; f_δ is a tunable constant; and T_{sw} is a representative value for the short-wave period at the wave boundary. Since this thesis is about hydrodynamics and compares results with a fixed bottom laboratory test, the morphological calculations in Delft3D are turned off. The settings for TRITON and Delft3D are not changed from

Table 5.3: *Calibration parameters in TRITON*

Parameter	Description	Boers-1B	Boers-1C
f_p	parameter breakermodel	10	10
ϕ_{ini}	parameter breakermodel	25	20
ϕ_{end}	parameter breakermodel	9	8
$t_{1/2}$	parameter breakermodel	$T_p/20$	$T_p/20$
f_δ	factor between true and TRITON roller thickness	7.5	2.5
N_f	order of filter	8	8
T_{sep}	separation-period (s)	3.3	5.0
T_{lw}	long-wave period (s)	10.0	11.9
T_{delay}	delay time (s)	4.0	6.0

the model by Wenneker et al. (2011) (see table 5.3).

5.3 Validation

5.3.1 Wave forces

Wave forces are extracted from the map-file and – in the case of TRITON – wave-averaged (the roller model is already wave-averaged). The time-step for the map-file is three seconds, which is relatively large compared to wave period. However, a quick investigation showed that reducing the time-step to 0.6 seconds has negligible effects on the extracted wave forces and they are therefore assumed to be correct. Figure 5.5 shows the measured and calculated wave forces for both Boers-1B (a to c) and Boers-1C (d to f). Only wave forces near the breaker bar are shown, since in the remainder of the wave flume they are minor. The first large difference between calculated and measured wave forces is magnitude: which is a lot smaller for both the roller model and TRITON. This is unexpected since the equation of Longuet-Higgens and Stewart (1964) (which is also used by the wave-drivers) approximated wave forces a lot better in the data analysis. A possible reason for this difference may lay in grid size, which for Delft3D is 20 cm and measurements on the breaker bar around 10 cm. This difference is however not that large that one would expect averaging would cause such a large difference. Another possibility is that dissipation is underestimated, this should then be visible in an overestimation of wave height. This is true for TRITON in Boers-1B (figure 5.2), where wave breaking at the first breaker bar is underestimated. In figure 5.5c this can be seen by the absence of a large positive wave force at around $x = 21\ m$. However, the other cases show acceptable approximations of wave height but wave forces are still too small. The last possibility that was investigated was the fact that in measurements effects of the boundary and roller could be present. It is assumed that the roller force is only present above wave trough level, this is potentially a wrong assumption. However, summation of wave (body) and roller forces still cannot explain the difference in magnitude, although it should be noted roller forces are also too small. At this time, the differences between measured and modelled wave force magnitudes cannot be sufficiently explained and is worth looking into in future research.

From the low wave forces one would expect an underestimation of setup levels. In reality, quite the opposite is true, where setup levels for Roller-FLOW are greatly overestimated and levels by TRITON-FLOW are quite good. Note that setup values shown in figure 5.3 are the ones calculated by Delft3D-FLOW (so based on radiation stress from TRITON). Setup values plotted in Wenneker et al. (2011) were calculated from free surface data from TRITON, which showed different results. The reason why setup values from Delft3D-FLOW are shown is that these are important for the mean-flow, not the ones from TRITON.

Not taking the offset into account, the wave setup is still overestimated by Roller-FLOW (figure 5.3). The origin of this problem is unknown, but might be related to the wave force problem discussed before. If no wave forces are used (so the old model with the wave force errors), setup values are approximated quite well. However, if the wave force problem really is to blame is speculation and has not been tested. Problems may also be related to mean bed shear stresses (equation 2.10), but measured mean bed shear stresses show both positive and negative values depending on the experiment (Boers, 2005), making it difficult to determine if models are correct. From equation 2.10

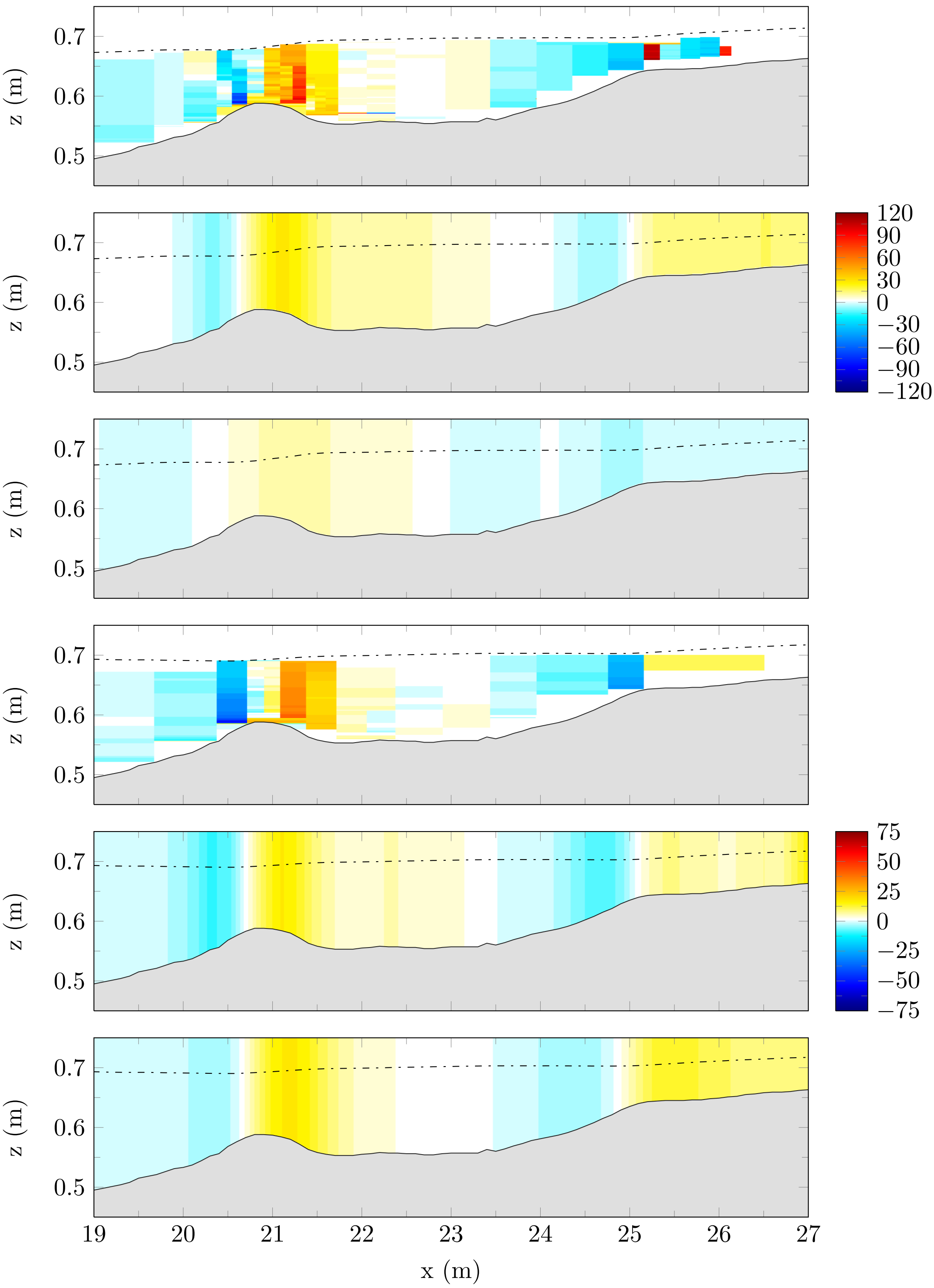

Figure 5.5: *Comparison of (a,d) measured wave forces (Nm^{-3}); (b,e) results from Roller-Delft3D; and (c,f) results from TRITON-Delft3D. (a) to (c) are Boers-1B and (d) to (f) are Boers-1C. Onshore directed wave forces are positive, offshore directed negative.*

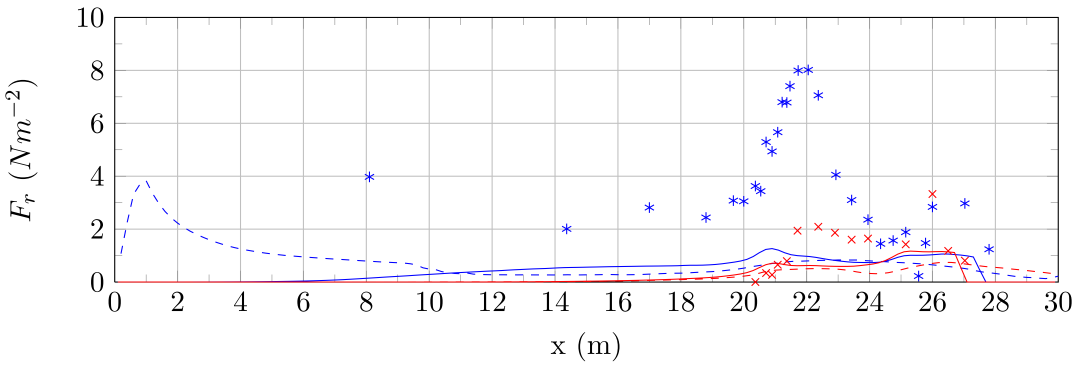

Figure 5.6: *Comparison of measured roller forces (marks) and calculated ones by roller model (solid) and TRITON (dashed) for both Boers-1B (blue) and Boers-1C (red).*

it is to be expected that negative bed shear stresses increase setup-levels. Modelled bed shear stresses by Roller-FLOW are with the exception of the first 5-10 meters negative, possibly explaining the difference. Modelled bed shear stresses for TRITON-FLOW are positive, and might explain the better approximation of setup-levels.

As discussed before, Roller-FLOW setup levels start with an offset and for Boers-1B start to increase earlier than the measurements because of a sharper decline in wave height (thus energy dissipation, figure 5.2). This process continues up until the breaker bar where the increase of setup levels is modelled quite well. Setdown in the surf zone trough (or to be precise: decreasing setup levels) hardly occur for Roller-FLOW since no reshoaling takes place. This is because breaking continues further into the surf zone trough for the model (also see wave forces, figure 5.5). The resulting modelled setup levels at the end of the wave flumes are greatly overestimated because of a superposition of the problems describe here. For Boers-1C, results are better but also here the setdown in the surf zone trough is not modelled correctly.

TRITON-FLOW does not suffer from the offset as the roller model does. Results are good until the breaker bar; after which also TRITON-FLOW is not able to properly model the setdown. For Boers-1C, results are quite good with a small overestimation because of the absence of setdown. This is related to the switch between negative to positive wave forces, which occurs slightly too early for the models, and the roller forces that increase too early as well. Wrong prediction of the breaking point is the main cause for this problem (figure 5.2). For Boers-1B results are worse and setup levels are underestimated because of an underestimation of breaking at the breaker bar, as can be seen in the wave heights.

5.3.2 Roller force

The roller forces are shown in figure 5.6. The roller energy was estimated from measurements through the mass flux by Boers (2005). After this, roller energy was converted to roller forces; this means they were also modelled. The procedure is shown in section 4.3 of Boers (2005) and is based on linear wave theory. Both model systems underestimate roller forces significantly. The pattern is somewhat similar, but even that is doubtful. It should be noted that TRITON was calibrated on undertow, rather than roller force, ie. the roller force was changed in order to properly model the undertow. The roller model seems to perform slightly better near the breaker bar, but even here values are significantly smaller. It can thus be concluded that roller forces are modelled very poorly with the current settings. However, it should be mentioned that the roller force is used for calibration of wave height and setup; and in the case of TRITON also the undertow.

5.3.3 Turbulent kinetic energy

Section 3.7 discussed the vertical turbulent kinetic energy profiles. The TKE was calculated with Roller-FLOW and TRITON-FLOW of which the results are presented in figure 5.7. Since TKE is calculated by Delft3D-FLOW, similar profiles are to be expected and differences are thus related to different input from the wave-drivers.

Results by Roller-FLOW for Boers-1B are acceptable in the shoaling zone, but overestimate TKE just before breaking. Values after the breaker bar and in the surf zone trough are well approximated, but on the second breaker bar and at the end of the wave flume ($x > 25\ m$) turbulence is greatly overestimated, possibly because of the small water depth with which Delft3D seems to have some trouble modelling (note that TRITON only shows minor breaking at the region and therefore gives different results). The shape of the profile is more curved with Roller-FLOW than is seen in measurements, especially near the bottom it seems turbulence production is overestimated at all locations. This is possibly a result of an overestimation of dissipation through friction (see equation 4.16b); which is itself related to an overestimation of orbital velocities at the bed.

TRITON-FLOW performs slightly better at most locations, especially at the end of the wave flume where results still match measurements. This seems odd, since wave height at this location is greatly overestimated by TRITON-FLOW, which means less dissipation and an underestimation of TKE high in the water column is to be expected. Bottom production seems to be modelled better with TRITON-FLOW than Roller-FLOW, possibly due to a better estimation of the orbital bed velocity (also see figure 5.8) and thus dissipation through friction. The orbital bed velocity can however not be compared, since Roller-FLOW does not give it as output. Just before the first breaker bar crest, TRITON-FLOW suffers from the same problems as Roller-FLOW.

Results for Boers-1C are very similar, although at times approximations by Roller-FLOW are slightly better than TRITON-FLOW before the breaker bar; TRITON-FLOW gives better results just after the first breaker bar.

5.3.4 Undertow

The measurements and calculations of the undertow are shown in figure 5.8. For both Boers-1B and Boers-1C, Roller-FLOW overestimates the undertow, with the exception of the lower water column just onshore of the first breaker bar in Boers-1B. A magnitude overestimation points to an overestimation of breaker-generated mass flux above wave trough level, which would be visible through decreasing wave height (wave energy dissipation) and roller force (larger surface rollers). TRITON-FLOW better predicts undertow, and it is therefore expected that the roller mass flux is also better approximated. Since the mass flux is not given as output, it is impossible to verify this. The mass flux is calculated by TRITON and transferred to Delft3D-FLOW; where for Roller-FLOW Delft3D-FLOW calculates the mass flux. For TRITON-FLOW, the only problems occur just after the first breaker bar where the undertow in the lower water column is underestimated for Boers-1B, although it should be noted that results from

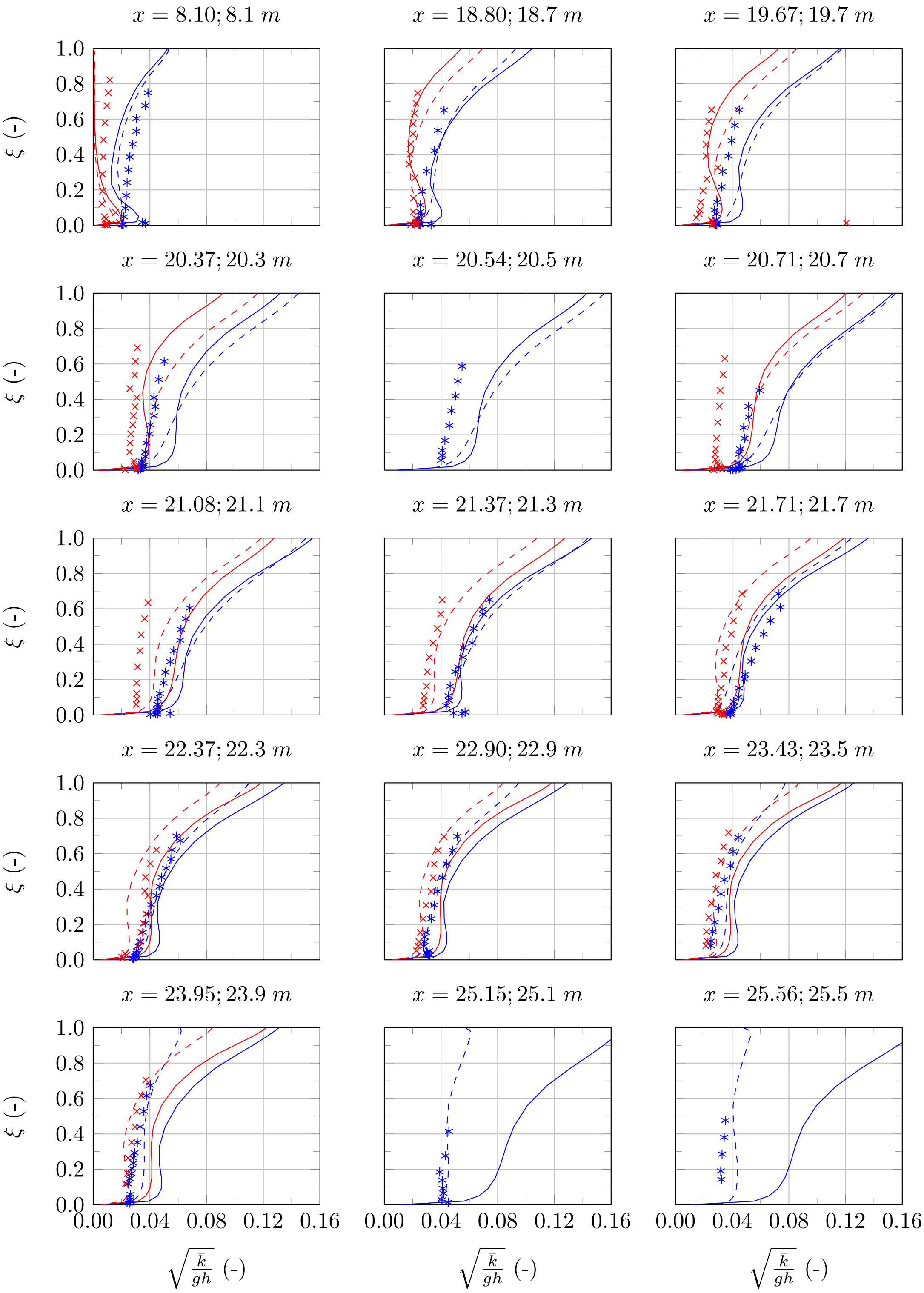

Figure 5.7: *Comparison of measured turbulent kinetic energy for Boers-1B (∗) and Boers-1C (×); calculated TKE by Roller-FLOW for Boers-1B (——); and Boers-1C (——) and TRITON-FLOW for Boers-1B (- - -) and Boers-1C (- - -). The first x-value is from the measurements and the second from the location of the observation point in Delft3D-FLOW.*

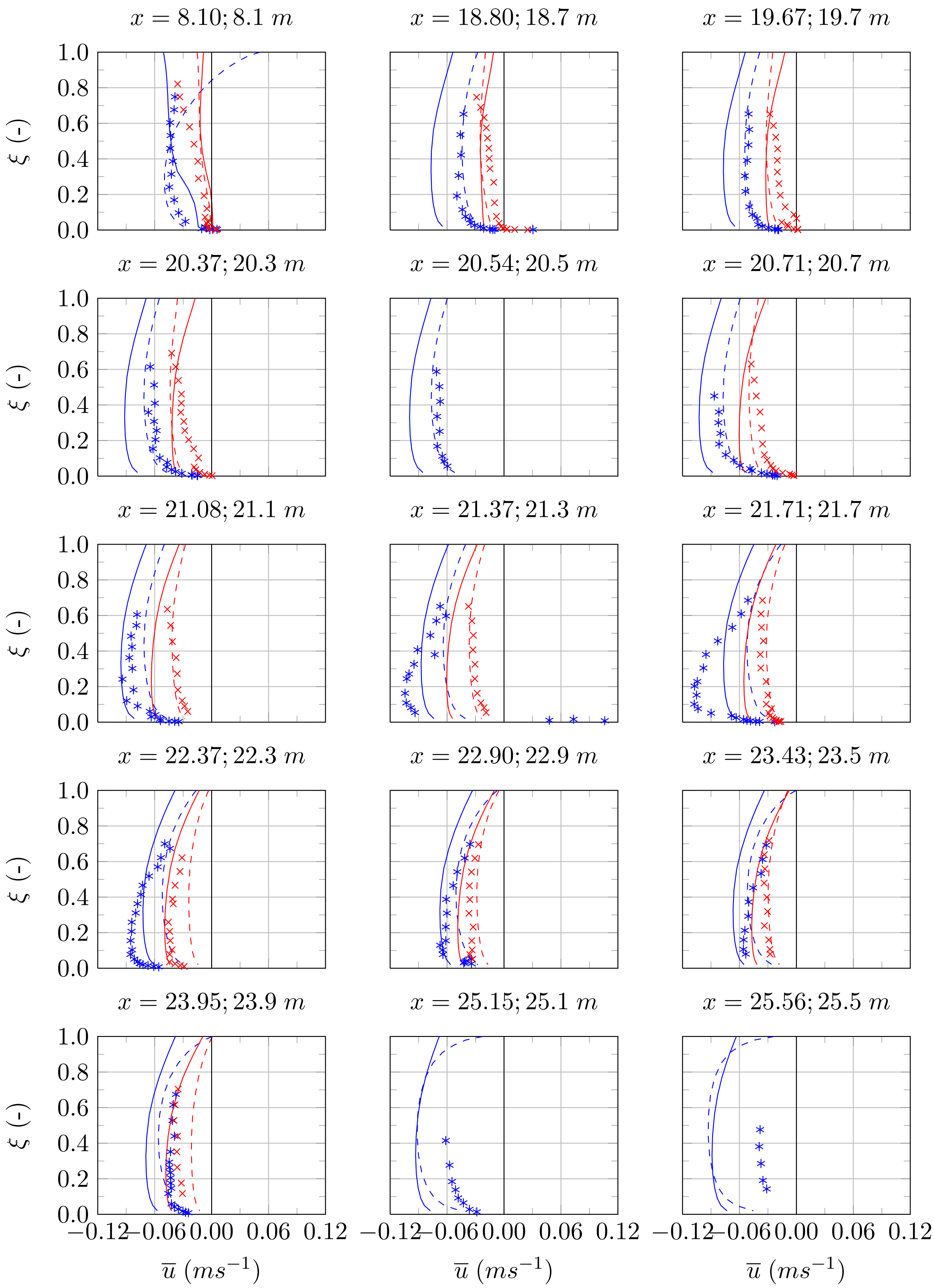

Figure 5.8: *Comparison of measured undertow for Boers-1B (∗) and Boers-1C (×); calculated undertow by Roller-FLOW for Boers-1B (——) and Boers-1C (——); and TRITON-FLOW for Boers-1B (- - -) and Boers-1C (- - -). The first x-value in the title is from the measurements and the second from the location of the observation point in Delft3D-FLOW.*

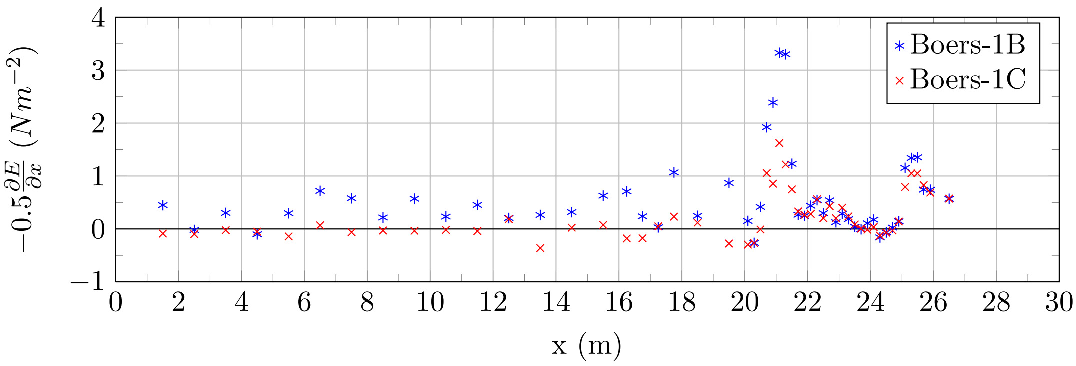

Figure 5.9: *Surface shear stress due to radiation stress between wave trough and crest for Boers-1B and Boers-1C, calculated from measurements.*

Wenneker et al. (2011) suggest the magnitude could be fixed by calibrating the roller force.

The vertical structure of the undertow at most locations is not properly modelled neither by Roller-FLOW nor TRITON-FLOW. TRITON-FLOW does perform best, especially close to the bottom, where measurements become less negative or even positive and just after the breaker bar where the measured undertow shows a 'belly-profile' ($x = 21 - 22\ m$). The 'belly-profile' is not obvious in measurements from Boers-1C, which is probably a result of smaller roller forces. The superior near bed velocities from TRITON-FLOW could possibly be explained by the differences in bed shear stresses, as discussed before.

5.4 Assessment

5.4.1 Surface shear stresses

Since wave forces below wave trough have a virtually uniform profile, they do not significantly affect the undertow profile. Roller forces, which are concentrated at the surface layer, do cause a change in the undertow profile. The roller force – modelled as a shear stress – drags the top of the undertow profile towards the coast. Since the mass flux above wave trough still needs to be balanced, the undertow in the lower water column will have to become more negative. A larger roller force is thus expected to cause a greater curvature of the undertow profile. In Boers-1B measurements, a peak in roller force is found between $x = 21 - 23\ m$ with a maximum at around $x = 22\ m$ (figure 5.6). Around $x = 22\ m$, high curvature of the measured undertow profile can be seen (figure 5.8), other areas that show higher roller forces also show larger curvatures of the undertow profile. In modelled undertow profiles this is less pronounced, possibly because roller forces are small to begin with and only show small deviations.

During the comparison of measured radiation stress to analytical formulations (section 3.3.2) we saw that in order to properly model radiation stresses below wave trough level there needs to be a split of radiation stresses below and above wave trough level. The radiation stresses above wave trough level (E_D in Mellor (2008)) are to be modelled as a shear stress at the surface. Just like the roller force, this E_D would lead to a larger curvature of the undertow profile. Since Delft3D does not separate the radiation stress components, this surface shear stress is missing in the model results and might explain why the undertow profiles are not sufficiently curved. The additional shear stress due to E_D is shown in figure 5.9. It can be seen that especially around $x = 20.5 - 21.5\ m$ this E_D-contribution is significant and of the same order of magnitude as the roller force. In this area, we can also see an underestimation of the curvature of the undertow in figure 5.8. Therefore, we assume E_D at least partly explains this deficiency.

5.4.2 Turbulent kinetic energy and eddy viscosity

The turbulent kinetic energy profiles have their effects on the undertow profile through eddy viscosity, as shown in equation 4.12. Dissipation values (ϵ) were not extracted from measurements and thus no eddy viscosity profiles can be created through equation 4.12. However, since turbulent velocities were measured, there is another way to determine eddy viscosity profiles and that is through the Boussinesq-hypothesis, as shown in equation 4.11. In this case, we use an adaptation of this equation, which looks like:

$$-\rho\overline{u'w'} = \rho\overline{\nu_t}\frac{\partial\overline{u}}{\partial z} + \overline{\tilde{\nu_t}\frac{\partial\tilde{u}}{\partial z}} \tag{5.4}$$

The last component of equation 5.4 is unknown and cannot be determined. However, it is assumed that outside the bottom boundary layer this component can be neglected. And thus the (wave-averaged) eddy viscosity is calculated from measurements with:

$$\overline{\nu_t} = -\frac{\overline{u'w'}}{\frac{\partial\overline{u}}{\partial z}} \tag{5.5}$$

Figure 5.10 presents eddy viscosities at x-locations for Boers-1B. The resulting eddy viscosities also show negative values (not shown in figure 5.10). The negative eddy viscosities show no apparent pattern and appear randomly across the water column. Therefore, we follow Rodi (1993) who states that they have no physical meaning (note that negative eddy viscosities could have a physical meaning in special cases (Davies & Villaret, 1999)). The origin of negative eddy viscosities high in the water column seems to lie in $\partial\overline{u}/\partial z$, which varies around zero higher in the water column. On a theoretical basis, it is to be expected that the undertow in this area shows a positive vertical derivative instead of a negative one. In other words, we expect the undertow velocities to decrease because of shoreward directed surface shear stresses. However, since changes are minor, a small measurement error could lead to a negative derivative and thus a negative eddy viscosity, see figure 5.12. Lower in the water column – at the edge of the bottom boundary layer – the switch of signs for turbulent Reynolds stress and undertow derivative do not occur at the same distance from the bed, also here measurement errors are the assumed origin of negative eddy viscosities.

When we compare the results in figures 5.10 and 5.11, we can see that only eddy viscosities at $x = 23.43\ m$ are close to those modelled. However, we do not have full confidence in the eddy viscosities extracted from data because they show doubtful patterns and because of the negative values, as discussed above. We can thus not say if Delft3D models eddy viscosities properly.

One might expect different TKE-profiles to lead to different undertow profiles, but this is only partly true. From equations 4.13a and 4.13b, it becomes clear that turbulence and dissipation are linked. This leads to similar eddy viscosity profiles for Roller-FLOW and TRITON-FLOW (figure 5.11). The main effect of TKE is on eddy viscosity

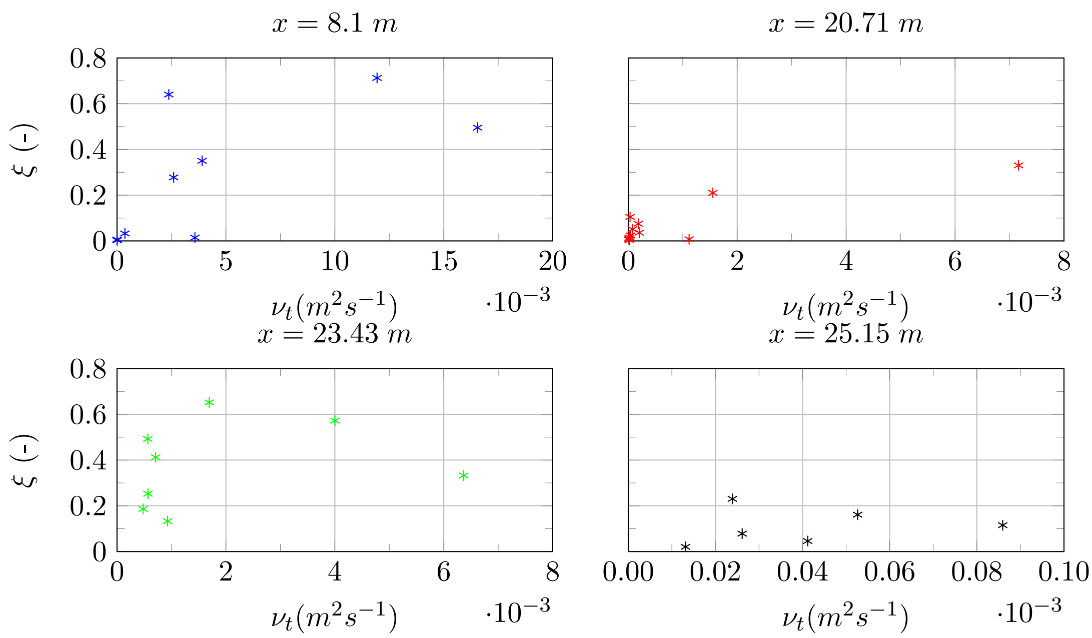

Figure 5.10: *Eddy viscosities extracted from Boers (2005), Boers-1B*

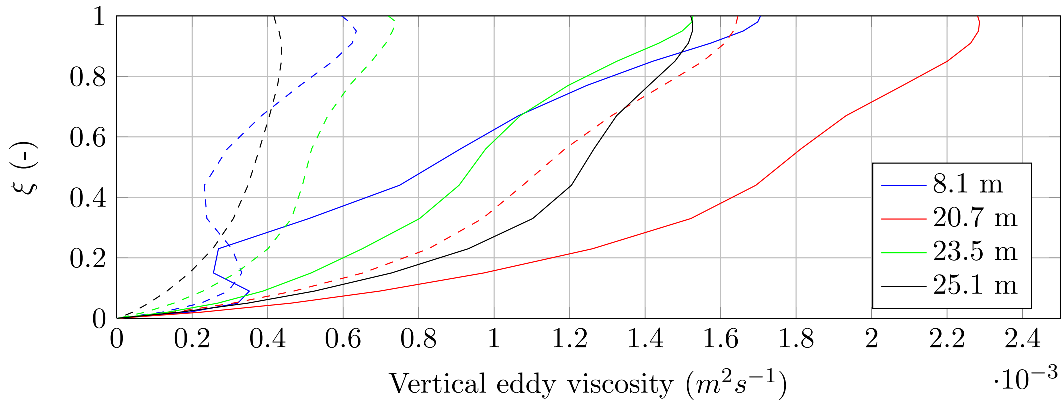

Figure 5.11: *Comparison of vertical eddy viscosity between roller model (solid) and TRITON (dashed) for Boers-1B*

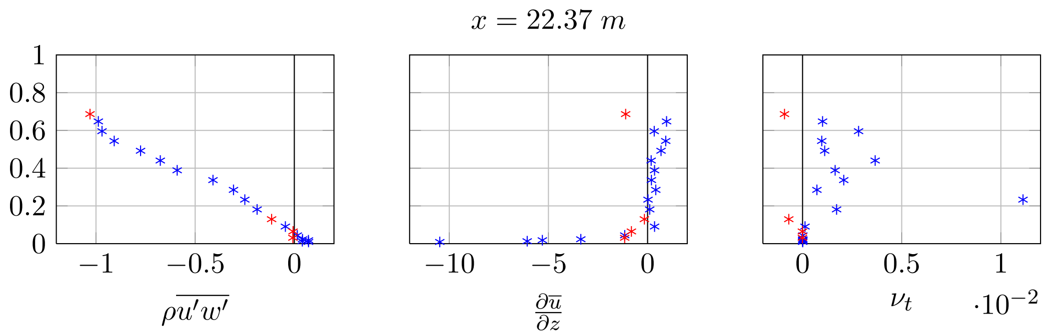

Figure 5.12: *The different components of eddy viscosity (left and mid) and the resulting eddy viscosities (right) for Boers-1B, x = 22.37 m. Red marks show the locations where negative eddy viscosities are found.*

Table 5.4: *Explanation of curvature of undertow profile*

x (m)	Eddy viscosity		Roller force		Curvature
	Roller	TRITON	Roller	TRITON	
8.1	Much higher	Much lower	Low	High	TRITON way more
20.7	High	Low	High	Low	Similar
23.5	Much higher	Much lower	Equal	Equal	TRITON slightly more
25.1	Much higher	Much lower	Little high	Little low	TRITON way more

magnitude. The effect of eddy viscosity magnitude on undertow becomes apparent when combining it with the roller force. As discussed in section 2.3.2, viscosity is a measure for the resistance against deformation, ie. high viscosity means less curvature of the undertow profile through roller force. The combination of eddy viscosity and roller force can explain the curvature of the undertow profile in the upper water column directly, and indirectly on the lower part through mass flux, as discussed before. This is shown in table 5.4. High viscosity and high roller force cancel each other out, low viscosity and high roller force amplify the curvature of the undertow.

5.4.3 Phase-averaged vs. phase-resolving

To assess if a phase-resolving wave-driver improves the model performance of mean-flow dynamics we compare the results as presented in the previous sections. Wave heights were found to be modelled best by Roller-FLOW, since TRITON-FLOW performed surprisingly poor after the first breaker bar for Boers-1B where wave heights were overestimated. TRITON-FLOW approximated setup values well, although for Boers-1B it suffered from the lack of wave breaking after the first breaker bar. Roller-FLOW suffered from an offset of the water level, but even when not taking this into account, setup values were overestimated for both Boers-1B and Boers-1C. Modelled wave forces in both models were found to be significantly smaller than those found in measurements. The reason for this is unknown. Roller forces too were found to be too small for both models, although this is likely a result of calibration to improve other processes like wave height and wave setup.

TKE-levels before the breaker bar are modelled similarly by both models and show acceptable agreements with measurements. For Boers-1B, TRITON-FLOW performs better after the first breaker bar, where Roller-FLOW overestimates TKE-levels more significantly. In the surf zone trough both models perform equally, which is surprising because TRITON-FLOW does not show good approximations for wave breaking in this area for Boers-1B. Looking at the vertical profile, we see that Roller-FLOW is more heavily curved at the bottom than TRITON-FLOW and measurements. This is thought to be related to overestimations of flow velocities near the bed by Roller-FLOW.

For the modelling of the undertow we see that TRITON-FLOW performs better in the shoaling zone for Boers-1B, but not so much just after the first breaker bar. This too, seems to be related to the poor performance of wave breaking. For Boers-1C, TRITON-FLOW gives better approximations than Roller-FLOW at virtually all locations. And perhaps most importantly for sediment transport is the fact that near bed flow velocities are modelled better than Roller-FLOW which overestimates flow velocities everywhere.

All in all, we can conclude that TRITON-FLOW outperforms Roller-FLOW on mean-flow dynamics in most areas. However, the practicality of TRITON-FLOW is questionable. The grid size was small and model time short; nevertheless computational time for TRITON-FLOW was 4-5 hours, for Roller-FLOW this was only 10 minutes. For large cases TRITON-FLOW may simply be to slow. Future improvements in computational power and efficiency of TRITON-calculations may make computational times more manageable; thus increasing the practicality of TRITON-FLOW.

5.5 Conclusions

During the calibration process, errors related to wave forces were found in the roller model that complicated analysis of the results. The effects of the resulting offset throughout the wave flume were assessed and were found to have a negligible small influence on the processes that were validated. Calibration results for TRITON were better than the roller model, which mainly suffers from an overestimation of setup levels.

Modelled wave forces were found to be significantly smaller than those gathered from measurement data. Three different reasons were considered: (i) averaging over larger areas, reducing peak values; (ii) underestimation of wave energy dissipation; and (iii) effects of the bottom boundary and roller. Although these reasons could (potentially) explain part of the difference, no satisfying explanation could be given for the total differences in magnitudes. From the underestimated wave forces, setup levels would be expected to also be underestimated, but this was not the case. It is worth to investigate this in future research.

The modelled roller forces were compared to roller forces determined by Boers (2005) from mass fluxes and were also found to be greatly underestimated. The roller model showed slightly better results than TRITON, but even these were far from satisfying. Also, TRITON's roller forces were calibrated for a better fit of the undertow and thus the better approximation by the roller model should not be seen as a direct advantage of this model.

In most areas, turbulent kinetic energy levels were found to be approximated quite well. The only area where both models overestimated TKE-levels was just before the breaker bar. The curvature of the profiles was found to be higher than is visible in measurements. This is thought to have two reasons: (i) an overestimation of turbulence production by bottom friction; and (ii) an underestimation of turbulence mixing, which would straighten-out the profiles of turbulent kinetic energy.

Undertow profiles were best modelled by TRITON-FLOW and the only problems were found near the breaker bar where velocities in the lower water column are underestimated. This is thought to be related to the curvature of the profile and thus the underestimation of roller forces by the model. Roller-FLOW overestimated undertow velocities on most location, which is considered to be an effect of the overestimation of mass flux by breaking waves. Since TRITON communicates the resulting roller mass flux with Delft3D-FLOW, this is assumed to be an advantage of the phase-resolving nature of TRITON. At times it is however difficult to see if the modelled undertow is wrong compared to data because of curvature or magnitude, and thus because of roller force or roller mass flux.

An assessment of the results showed curvature of the undertow profile in the higher water column to be related to a combination of roller force and eddy viscosity. A high roller force creates a more extreme curvature of the undertow profile, where high eddy viscosity levels resist the deformation of the flow and thus lead to less curvature. This conclusion is only drawn qualitatively and not quantitatively. A higher curvature would lead to smaller negative velocities high in the water column, but to higher negative velocities in the lower water column. Especially the magnitudes in the lower water column are important for (suspended) sediment transport and determining the correct roller force could thus be important for proper sediment transport modelling.

Mean-flow dynamics was found to be better approximated by TRITON-FLOW than Roller-FLOW on most topics and at most locations. Most importantly, TRITON-FLOW performed best in reproducing undertow velocities and curvature of the undertow profile, notably near the bed. At this point in time, the practicality of TRITON-FLOW is questioned, since it took significantly longer to finish the calculations, 4-5 hours for TRITON-FLOW against 10 minutes for Roller-FLOW. However, in the future computational times may become more manageable – increasing the practicality of TRITON-FLOW.

Chapter 6

Discussions, conclusions, and recommendations

The objective of this research was "to increase the understanding of mean-flow dynamics in the surf zone and to assess how well the wave-averaged Delft3D-model is able to simulate mean-flow dynamics". To achieve this goal we analysed laboratory data from Boers (2005) and subsequently modelled the wave flume in Delft3D with both a phase-averaged and phase-resolving wave driver. Discussion points about this research can be found in section 6.1. In section 6.2 the research questions as posed in section 1.3 are answered and a synthesis is given. Recommendations for future research are given in section 6.3.

6.1 Discussions

6.1.1 Measurement data

Although the data set of Boers (2005) is extensive and detailed, as with any data set, some discussion points can be made. For starters, the experiments from Boers (2005) were small-scale and for turbulent kinetic energy profiles differences were seen that were assumed to be related to the scale of the experiments. The effects of scale are unknown and it is therefore difficult to say if the profiles found in this thesis will be similar in large-scale experiments or field observations. Vertical profiles are not thought to be significantly altered by scale, but subtle differences in hydrodynamics could turn out to be important for sediment transport.

Ensemble averaging has been used to decompose the flow. As discussed before, only a small amount of ensembles were available (maximum of eleven) where according to Govender et al. (2002) at least 20 are necessary for mean flow and 40 for turbulent velocities. A quick investigation showed that mean and orbital flows were approximated well, despite the small amount of ensembles. Turbulence velocities varied more heavily and since the filter procedure by Boers (2005) could not be reproduced, values were different from Boers (2005). Still, it is very well possible that the flow was erroneously decomposed and could perhaps also explain why non-zero values for $\bar{w}$. Although this changes magnitudes of mean-flow dynamics, it is not expected to significantly alter the vertical profiles since errors that are introduced are small and are expected to appear on random locations, not with a certain profile.

Some differences were visible between the breaker types, but they were minor compared to what was expected from literature. Possible reasons for this are that Boers-1C was only weakly plunging and the wave sizes were small. Also, we only looked into the Boers (2005) data and did not include other data sets with similar breaker types to compare and see if differences are not just accidental.

6.1.2 Analysis

Although flow velocity measurements had a high density, for wave forces this data was still crude because of the x-derivative and near the break bar changes occur over a small distance. This crudeness makes it difficult to carry out a proper analysis and although differences were found, some fall in the range of uncertainty. The analytical patterns were calculated in MATLAB and only took local conditions into consideration. Advective and diffusive processes were neglected, which make the analysis more difficult since results are not smoothed as is the case with measurements and model results.

Similar problems occurred when considering the forcing by the RANS-components. Because of the detailed measurements, the z-derivative is sensitive to small measurement inaccuracies which lead to highly fluctuating values. During the analysis, results were handled with care and insight into trend-profiles was used to get a better understanding what was logical and what not.

In Wenneker et al. (2011) the roller force was calibrated to improve the undertow. Since this procedure was not carried out for the roller model, this makes it more difficult to compare the results of the wave drivers. Furthermore, it may cause the overestimation of the possibilities of TRITON since calibration is not possible when no measurements are available.

6.1.3 Modelling

During the modelling with the roller model, problems related to wave forces were found. In the normal version wave forces were falsely set to zero. This was fixed in a test-version, but in this version an offset of the water level over the whole wave flume was found. Although the effects of an offset were found to be small we are not sure if the roller model suffers from other related problems since it was just a test-version. For instance, Van der Weerd (2012) found numerical instabilities for some cases. Therefore, it is advisable to check if a new fully tested version gives the same results as found in this thesis.

The model results were only validated with data from Boers (2005); so conclusions drawn here are strictly speaking only valid for this data set. Possibly, other data sets lead to different conclusions and insights. However, since the data set of Boers (2005) was gathered in a controlled environment, contained detailed measurements and no large inexplicable differences were seen between the cases we think that the Boers (2005) data set gives a good approximation of reality.

6.1.4 Relevance to sediment transport

Sediment transport was not considered directly in this thesis, since it was not part of the Boers (2005) data. However, with the knowledge gained from this research some expectations can be formulated. For sediment transport both the undertow and turbulent kinetic energy (TKE) are assumed to be important. From the model assessment we saw that near the breaker bar the curvature of the undertow profile was not well approximated by the models. We assume this to be related to the underestimation of the roller force and the inclusion of the surface concentrated radiation stress term E_D into the body force rather than applying it as a surface shear stress. Increased undertow velocities in the lower water column could lead to higher current related sediment transport rates near the bed. In addition, suspended sediment transport higher in the water column would decrease since in this area velocities decrease. Undertow velocities at the bed were overestimated, which lead to overestimations of TKE too. We think that fixing the undertow velocities at the bed, will improve TKE approximations.

Looking at processes in the boundary layer, it seemed that wave forcing due to radiation stress gradients is not thought to be important and the z-derivative of Reynolds stresses was found to dominate in this area. Since wave Reynolds stresses (the largest contributor to the z-derivative of Reynolds stresses in the bottom boundary layer) are included in Delft3D-FLOW, no significant improvements are expected.

6.2 Conclusions

6.2.1 Research questions

What are the physical processes governing cross-shore mean-flow dynamics in the surf zone and what are the assumed vertical profiles of the RANS-components in literature?

Wave breaking is an important process in the surf zone. In total there are four different breaker types; of which only spilling and plunging are considered in this thesis. The breaking sequence is similar for spilling and plunging breakers; the only difference being scale of the processes involved. This sequence is a complicated order of events and is only understood qualitatively, not quantitatively. In the breaking process, a surface roller is formed which increases the mass, momentum, and energy fluxes towards the coast and is therefore important for mean-flow dynamics.

The physical processes in the surf zone were considered with the Reynolds-averaged Navier-Stokes equations. The wave-induced mean-flows are forced by gradients in radiation stress (wave force), and Reynolds stresses. Molecular viscosity is considered to have negligible effects. In literature, depth-dependent surf zone radiation stresses are considered to be uniform over depth. The mean-flow Reynolds stress ($\rho\overline{\bar{u}\bar{w}}$) is considered to be non-existent, wave Reynolds stress ($\rho\overline{\tilde{u}\tilde{w}}$) to be mostly uniform over depth, or from earlier literature non-existent above the bottom boundary layer (BBL). Turbulent Reynolds stress ($\rho\overline{u'w'}$) are assumed to linearly decrease from a maximum at water level to near-zero above the BBL, and to increase again in the BBL.

What are the vertical profiles of depth-dependent radiation stresses, wave forces, Reynolds stresses, and turbulent kinetic energy in the Boers (2005) data, and how important are the forcing components for the mean-flow?

Since Boers (2005) data above wave trough level showed questionable results, only the data below wave trough were considered. Vertical profiles of depth-dependent radiation stress were found to be mostly uniform over depth, although some deviations were discovered in the boundary layer on the breaker bar. The horizontal orbital velocity component is the dominant term in radiation stress. Radiation stress profiles for Boers-1C (weakly plunging) showed a greater uniformity than Boers-1B (spilling), but this is thought to be a result of shallower relative water depth, not necessarily breaker type. Depth-dependent wave forces were also found to be virtually uniform on all locations.

Mean-flow Reynolds stresses were found, contrary to what linear wave theory predicts. No clear profile was found and these Reynolds stresses are thought to be a result of measurement errors. Wave Reynolds stresses showed a trapezium shape with the maximum value close to the bottom and zero at the bed. The sign is dependent on bottom slope: a negative slope leads to negative values, a positive slope to positive ones. Turbulent Reynolds stresses were mostly negative and decreased linearly in magnitude from water level to bottom.

The magnitude of the forcings resulting from the different RANS-components was subsequently analysed. It was found the the Reynolds stresses produce a comparable forcing as radiation stress above the BBL, but with an opposite sign. The forcings due to radiation stress and Reynolds stresses thus largely cancel each other out. Therefore, the resulting change in mean-flow is small, as to be expected since undertow velocities are minor. Inside the BBL, the forcing due to Reynolds stresses is dominant; with the wave Reynolds stress being the largest contributor.

Turbulent kinetic energy (TKE) shows a linearly decreasing profile with the maximum at water level, where wave breaking is the main producer of TKE. Larger values were also found near the bed, due to friction generated turbulence. Plunging breakers show greater uniformity than spilling breakers.

From the resulting vertical distributions and comparisons with previous research, we can conclude a natural profile is important to approximate a real surf zone. The barred beach leads to a change of sign in wave Reynolds stresses and difference in magnitudes for negative wave forces and turbulence. Furthermore, the forcing by wave forces and Reynolds stresses is thought to amplify each other, rather than work against one-another in the case of a breaker bar.

How well are depth-dependent radiation stresses, wave forces, and wave Reynolds stresses represented by analytical equations?

Depth-dependent radiation stress profiles below wave trough are best represented by the equation of Mellor (2008) (M08). In the shoaling zone values are slightly overestimated, but at the breaker bar and surf zone trough results are well approximated. The improvement of M08 was found to be a result of the separate consideration of E_D, – representing the surface concentrated radiation stress between wave trough and crest. Since this term is also present in Longuet-Higgens and Stewart (1964) (LHS) and vertical dependence of M08 in the surf zone is negligible, a simple separation of the LHS-components gives the same result as M08. Wave forces from measurements are crude; making detailed analysis slightly harder. Both LHS and M08 show the same wave force pattern which closely resembles that of the measurements. However, it is not possible to say which one performs best.

The analytical equation of Zou et al. (2006) closely approximated measured wave Reynolds stresses above the BBL. The equation leaves the possibility open for calibrating wave breaking effects, but this did not seem to be necessary for most locations.

How is mean-flow dynamics in the surf zone modelled in a coupled system of wave-driver and Delft3D-FLOW?

Delft3D-FLOW is a wave-averaged hydrostatic model and therefore needs a wave-driver to calculate wave and roller forces. Two wave-drivers are considered: the roller model and TRITON who both calculate wave forces in a similar manner. The inclusion of rollers is done in a slightly different manner, leading to a different approximation of the roller force. Information between the wave-driver and Delft3D-FLOW is communicated with the help of a communication file, which is imported into Delft3D-FLOW. TRITON shares significantly more information with Delft3D-FLOW than the roller model does.

The water column in Delft3D-FLOW is divided into three different areas: a bottom, centre, and surface area which are considered more or less separately. The centre layer is the main body of the water column and the effects of the surface and bottom layer are taken into account by applying a shear stress at respectively the top and bottom of the centre layer. Wave forces are calculated by the wave-drivers and inserted into the momentum equation as an external source. The wave force is assumed to be uniform over depth, and distributed accordingly. The roller force is applied as a shear stress at mean water level.

The turbulence closure problem is solved by applying the Boussinesq-approximation which assumes that turbulence can be modelled as an additional viscosity. For this, eddy viscosity is introduced which is calculated with a $k - \epsilon$ model.

How well is mean-flow dynamics in the surf zone modelled by Delft3D and what are the differences when a phase-averaged or phase-resolving wave driver is used?

Modelled wave forces were found to be significantly smaller than those extracted from measurement data. No satisfactory explanation could be given and future research should look into this. Also, the expected underestimated setup levels were not seen in measurements. Roller forces too, were smaller than those gathered from measurements, although in all fairness they were modelled too.

Turbulent kinetic energy levels just before the breaker bar were overestimated by both models, but other areas were approximated well. The curvature of the vertical profiles was found to be too high. This high curvature is thought to be related to an overestimation of bottom turbulence production and an underestimation of turbulence mixing by the models.

The coupled system TRITON-FLOW modelled the undertow best, and only underestimated velocities in the lower water column on the breaker bar. Roller-FLOW overestimated undertow velocities on most locations which is thought to be a result of an overestimation of the mass flux above wave trough level. Curvature of the undertow profile could be explained by a combination of roller force and eddy viscosity. A high roller force and low eddy viscosity, leads to a strong curvature high in the water column. Since the mass flux above wave trough still needs to be balanced, the offshore velocities in the lower water column have to increase. Therefore, the curvature of the undertow is considered important for sediment transport. However, this is not modelled properly by either models; although TRITON-FLOW shows some better results.

The computational time of TRITON-FLOW (4-5 hours) was significantly longer than Roller-FLOW (10 minutes); which means practicality of TRITON-FLOW is doubtful.

However, with increasing computational power and increased efficiency in Boussinesq-wave drivers, it might become more efficient in the future.

6.2.2 Synthesis

Returning to the objective, we can conclude on what areas our knowledge about mean-flow dynamics in the surf zone and its modelling have increased. Depth-dependent wave forces were found to be mostly uniform; suggesting that wave forces are not very important for the undertow. The depth-dependent radiation stress as formulated by the analytical equation of M08 improved radiation stress approximations compared to the standard depth-integrated formulation of LHS divided over depth. We believe this to be a result of the separate consideration of radiation stress above wave trough level (E_D), which is applied as a shear stress rather than being distributed over the water column. If this improved wave forces was difficult to say. Since this E_D-component is modelled as a shear stress, this component is important for the undertow and leads to stronger curvatures of its profile.

The x-derivative of radiation stresses and the z-derivative of Reynolds stresses were found to have comparable magnitudes above the BBL. However, Delft3D only considers wave Reynolds stresses inside the BBL. The analytical equation of Zou et al. (2006) gave good results and could be implemented in Delft3D. Inside the BBL, the z-derivative of Reynolds stresses was found to dominate over wave forces, with the wave Reynolds stress as largest contributor.

TRITON-FLOW was found to outperform Roller-FLOW in most areas of mean-flow dynamics. Especially, undertow velocities and curvature of the undertow profile near the bed were better approximated. However, the practicality of TRITON-FLOW is questioned because of the large computational times.

6.3 Recommendations

Extension of data analysis

In this thesis hydrodynamics were wave-averaged before being analysed. As suggested by Ting and Kirby (1994), correlation between orbital and turbulent intensities could play an important role in wave-driven sediment transport. Other correlations could possibly also affect mean-flow dynamics and sediment transport, but for this the data analysis should consider the differences during the wave phase. This obviously complicates matters, and is not of great interest for models like Delft3D which are phase-averaged (although effects might be parameterised), but might be of interest to phase-resolving models like TRITON.

During the assessment of the undertow, it became clear that the curvature of the undertow profile could be explained by a combination of roller force and eddy viscosity. Although eddy viscosities were extracted, we did not have confidence in the results. Determining eddy viscosities through the use of dissipation levels might give better results. It is possible to extract dissipation from measurement data, but it is unknown if this is also the case for Boers (2005). If possible, eddy viscosity could be properly quantified and the undertow profiles could be explained more extensively.

Extension of modelling

During this thesis a start was made with modelling and validation of the model results. From the data analysis and model assessment it became clear that separating the radiation stress terms below wave trough from those above wave trough level (to be modelled as a shear stress) could potentially improve the undertow. We believe this is not too difficult since the radiation stress above wave trough level could be seen as an extra term of the roller force.

The modelled wave forces were found to be considerably smaller than those extracted from measurement data. Despite efforts to find the reason for this, no satisfying answer was found. Therefore, it is advised to carry out a detailed analysis of the modelling procedure and derivation of these wave forces. Combined with a further analysis of wave forces from data – so also look at wave forces without wave breaking, without bottom friction, etc. – this might give a reason for this problem.

Related to the item above, is the need for an improved roller model which could give better approximations of roller forces. Roller forces are now heavily calibrated and based on empirical constants. Changing this, could possibly lead to better approximations of the roller force, and subsequently better undertow. In Wenneker et al. (2011) it was shown that with certain calibration roller forces could be modelled well, and lead to a good approximation of the undertow. However, this was never true for the whole wave flume. An improved roller model should fix this.

Wave Reynolds stresses are at the moment only considered in the bottom boundary layer. In the data analysis they were found to exist throughout the wave flume because of the sloping bed. Since the forcing due to wave Reynolds stress is comparable to that of wave forces, it is advised to include them in Delft3D-FLOW and see if this improves model results. The equation of Zou et al. (2006) performed well, and could be a candidate for implementation.

Wave-averaged bed shear stresses were found to have opposite signs for Roller-FLOW and TRITON-FLOW; which possibly explains the poor results in wave setup for Roller-FLOW. Since measurements did not show a clear pattern, it was not possible to determine which model performed best. An assessment of the calculation of bed shear stresses is advised in combination with the modelling of setup values.

In this thesis, only the data from Boers (2005) was used for validation. To see if model adaptations lead to a general improvement of the models, validation of more cases is necessary, preferably with field cases. Furthermore, understanding the relationship between the driving terms and the undertow is at times difficult to comprehend. To get a better understanding of the effects of the different driving terms, one could carry out a sensitivity/modelling study of the different components on the undertow. A way to do this, is to turn subprocesses on and off. From the modelling results, it became clear that both the curvature of the undertow profile and magnitude are not always modelled well. Carrying out this additional analysis may give clarity which terms affect the curvature and which the magnitude.

Improvements of the undertow are good, but eventually we like it to lead to improved morphological calculations. Therefore, the effect of the improved undertow (assuming it does improve) on sediment transport should be modelled and investigated, too. This should be combined with an assessment of the performance of phase-averaged and phase-resolving wave-drivers. Possibly, the improved undertow in TRITON-FLOW is not very important for sediment transport. Although it must be mentioned, that TRITON includes more sophisticated sediment transport modules than the roller model does since it can also calculate wave skewness, etc.

Additional related research

Data between wave trough and crest was disregarded in this thesis because they showed doubtful patterns at times. It is unknown if any data set exists which does have useful data in this area. But since the area between wave trough and crest is not well understood it could give new insights into wave breaking, roller formation, surface shear stresses, and other related processes. Studies with detailed FEM-models could also help us increase our understanding.

The equation of Mellor (2008) shows promise for further research. Depth-dependence in the surf zone was negligible for cross-shore radiation stress, and Mellor (2008) may not be necessary to improve results, as discussed above. Depth-dependence in deep and intermediate water depths is significant and here Mellor (2008) could show significant improvements, something which is suggested by results presented in Sheng and Liu (2011). However, caution is advised, since areas outside the surf zone may suffer from spurious currents as discussed in Bennis et al. (2011).

References

Aagaard, T., Black, K. P., & Greenwood, B. (2002). Cross-shore suspended sediment transport in the surf zone: a field-based parameterization. *Marine Geology*, *185*, 283-302.

Aagaard, T., & Masselink, G. (1999). *The Surf Zone*, in Handbook of Beach and Shoreface Morphodynamics, ed. A.D. Short, pp. 72-118. Chichester, England: Wiley & Sons Ltd.

Arcilla, A. S. (1989). Hydrodynamic analysis of the surf zone. *International journal for numerical methods in engineering*, *27*, 87-101.

Ardhuin, F., Jenkins, A. D., & Belibassakis, K. A. (2008). Comments on "The three-dimensional current and surface wave equations". *Journal of Physical Oceanography*, *38*, 1340-1350.

Basco, D. R. (1985). A qualitative description of wave breaking. *Journal of Waterway, Port, Coastal and Ocean Engineering*, *111*(2), 171-188.

Battjes, J. A. (1974). Surf similarity. *Proceedings of 14th Coastal Engineering Conference*, 466-480.

Battjes, J. A. (1988). Surf-zone dynamics. *Annual Review of Fluid Mechanics*, *20*, 257-293.

Bennis, A.-C., Ardhuin, F., & Dumas, F. (2011). On the coupling of wave and three-dimensional circulation models: choice of theoretical framework, practical implementation and adiabatic tests. *Ocean Modelling*, *40*, 260-272.

Boers, M. (1996). *Simulation of a surf zone with a barred beach. Part 1: Wave heights and wave breaking* (Tech. Rep. No. 96-5). Delft, The Netherlands: Division of Hydraulic and Geotechnical Engineering, TU Delft.

Boers, M. (2005). Surf zone turbulence (Doctoral dissertation, Technical University Delft). *Communications on Hydraulic and Geotechnical Engineering*.

Borsboom, M., Doorn, N., Groeneweg, J., & Van Gent, M. (2000). A Boussinesq-type wave model that conserves both mass and momentum. *Proc. 27th ICCE Conference, Sydney*, 148-161.

Borsboom, M., Doorn, N., Groeneweg, J., & Van Gent, M. (2001). Near-shore wave simulations with a Boussinesq-type model including breaking. *Proc. Coastal Dynamics 2001, Lund, Sweden*, 759-768.

Christensen, E. D., Walstra, D.-J., & Emerat, N. (2002). Vertical variation of the flow across the surf zone. *Coastal Engineering*, *45*, 169-198.

Davidson-Arnott, R. (2010). *Introduction to coastal processes and geomorphology.* Cambridge, United Kingdom: Cambridge University Press.

Davies, A. G., & Villaret, C. (1999). Eulerian drift induced by progressive waves above rippled and very rough beds. *Journal of Geophysical Research*, *104*(C1), 1465-1488.

De Serio, F., & Mossa, M. (2006). Experimental study on the hydrodynamics of regular breaking waves. *Coastal Engineering*, *53*, 99-113.

De Vriend, H. J., & Kitou, N. (1990). Incorporation of wave effects in a 3D hydrostatic mean current model. *Proceedings of the 22nd international conference on coastal engineering*, 1005-1018.

De Vriend, H. J., & Stive, M. J. F. (1987). Quasi-3D modelling of nearshore currents. *Coastal Engineering*, *11*, 565-601.

Deigaard, R. (1993). A note on the three-dimensional shear stress distribution in a surf zone. *Coastal Engineering*, *20*, 157-171.

Deigaard, R., & Fredsøe, J. (1989). Shear stress distribution in dissipative water waves. *Coastal Engineering*, *13*, 357-378.

Deltares. (2012). *Delft3D-FLOW user manual.* Delft, The Netherlands: Author.

Dyhr-Nielsen, M., & Sørensen, T. (1970). Some sand transport phenomena on coasts with bars. *Proceedings of 12th Coastal Engineering Conference*, 855-866.

Galvin, C. J. (1968). Breaker type classification on three laboratory beaches. *Journal of Geophysical Research*, *73*(12), 3651-3659.

Govender, K. (1999). Velocity, vorticity and turbulence measurements in the surf zone (Doctoral dissertation, University of Natal). *Department of Physics*.

Govender, K., Mocke, G. P., & Alport, M. J. (2002). Video-imaged surf zone wave and roller structures and flow fields. *Journal of Geophysical Research*, *107*(C7), 9-1 - 9-21.

Grasmeijer, B. T. (2002). Process-based cross-shore modelling of barred beaches (Doctoral dissertation, University Utrecht). *Netherlands Geographical Studies*, *302*.

Groeneweg, J. (1999). Wave-current interactions in a generalized Lagrangian mean formulation (Doctoral dissertation, Technical University Delft). *Communications on Hydraulic and Geotechnical Engineering*, *99-5*.

Groeneweg, J., Doorn, N., Borsboom, M., & van Gent, M. (2002). Boussinesq-type modeling of measured wave breaking on a circular shoal. *Proc. 29th ICCE, ASCE, Cardiff*, 495-507.

Haas, K. A., & Warner, J. C. (2009). Comparing a quasi-3D to a full 3D nearshore circulation model: SHORECIRC and ROMS. *Ocean Modelling*, *26*, 91-103.

Holthuijsen, L. H. (2007). *Waves in oceanic and coastal waters.* Cambridge, United Kingdom: Cambridge University Press.

Horikawa, K. (1988). *Nearshore dynamics and coastal processes.* Tokyo, Japan: University of Tokyo Press.

Jones, W. P., & Launder, B. E. (1972). The prediction of laminarization with a two-equation model of turbulence. *Int. J. Heat Mass Transfer*, *15*, 301-314.

Kraus, N. C., & Horikawa, K. (1990). *Nearshore sediment transport*, in The Sea, vol. 9B: Ocean Engineering Science, eds. B. Le Mehauté and D. Hanes, pp. 775-814. New York, United States: Wiley & Sons, Inc.

Kumar, N., Voulgaris, G., & Warner, J. C. (2011). Implementation and modification of a three-dimensional radiation stress formulation for surf zone and rip-current applications. *Coastal Engineering*, *58*, 1097-1117.

Lesser, G. R. (2009). An approach to medium-term coastal morphological modelling (Doctoral dissertation, Delft University of Technology / UNESCO-IHE Institute for Water Education). *CRC Press/Balkema*.

Lesser, G. R., Roelvink, J. A., van Kester, J. A. T. M., & Stelling, G. S. (2004). Development and validation of a three-dimensional morphological model. *Coastal Engineering*, *51*, 883-915.

Longuet-Higgens, M. S., & Stewart, R. W. (1960). Changes in the form of short gravity waves on long waves and tidal currents. *Journal of Fluid Mechanics*, *8*(4), 565-583.

Longuet-Higgens, M. S., & Stewart, R. W. (1961). The changes in amplitude of short gravity waves on steady non-uniform currents. *Journal of Fluid Mechanics*, *10*(4), 529-549.

Longuet-Higgens, M. S., & Stewart, R. W. (1962). Radiation stress and mass transport in gravity waves, with application to 'surf beats'. *Journal of Fluid Mechanics*, *13*(4), 481-504.

Longuet-Higgens, M. S., & Stewart, R. W. (1964). Radiation stresses in water waves: a physical discussion, with applications. *Deep-sea Research*, *11*, 529-562.

Mellor, G. L. (2003). The three-dimensional current and surface wave equations. *Journal of Physical Oceanography*, *33*, 1978-1989.

Mellor, G. L. (2005). Some consequences of the three-dimensional current and surface wave equations. *Journal of Physical Oceanography*, *35*, 2291-2298.

Mellor, G. L. (2008). The depth-dependent current and wave interaction equations: a revision. *Journal of Physical Oceanography*, *38*, 2587-2596.

Mellor, G. L. (2011). Wave radiation stress. *Ocean Dynamics*, *61*, 563-568.

Mellor, G. L. (2012). Waves, circulation and vertical dependence. *4th International Workshop on Modelling the Ocean*, 1-24.

Mocke, G. P. (2001). Structure and modeling of surf zone turbulence due to wave breaking. *Journal of Geophysical Research*, *106*(C8), 17039-17057.

Mooiman, J. (2012). *Delft3D-FLOW: Description of numerical implementation.* Delft, The Netherlands: Deltares.

Nairn, R. B., Roelvink, J. A., & Southgate, H. N. (1990). Transition zone width and implications for modelling surfzone hydrodynamics. *Coastal Engineering Proceedings*, *22*, 68-81.

Nielsen, P. (1992). *Coastal bottom boundary layers and sediment transport.* Singapore, Singapore: World Scientific Publishing.

Reeve, D., Chadwick, A., & Fleming, C. (2004). *Coastal engineering: processes, theory and design practice.* Abingdon, England: Spon Press.

Rivero, F. J., & Arcilla, A. S. (1995). On the vertical distribution of $< \tilde{u}\tilde{w} >$. *Coastal Engineering*, *25*, 137-152.

Rodi, W. (1993). *Turbulence models and their application in hydraulics: A state-of-the-art review.* Rotterdam, The Netherlands: A.A. Balkema.

Roelvink, J. A., & Reniers, A. J. H. M. (2012). *A guide to modelling coastal morphology.* Singapore: World Scientific Publishing.

Ruessink, B. G. (2010). Observations of turbulence within a natural surf zone. *Journal of Physical Oceanography*, *40*, 2696-2712.

Schwartz, M. L. (2005). *Encyclopedia of Coastal Science.* Dordrecht, The Netherlands: Springer.

Scott, C. P., Cox, D. T., Maddux, T. B., & Long, J. W. (2005). Large-scale laboratory observations of turbulence on a fixed barred beach. *Measurement Science and Technology*, *16*, 1903-1912.

Scott, C. P., Cox, D. T., Shin, S., & Clayton, N. (2004). Estimates of surf zone turbulence in a large-scale laboratory flume. *Coastal Engineering*, *14*, 379-392.

Sheng, Y. P., & Liu, T. (2011). Three-dimensional simulation of wave-induced circulation: Comparison of three radiation stress formulations. *Journal of Geophysical Research*, *116*, 1-17.

Smith, J. A. (2006). Wave-current interactions in finite depth. *Journal of Physical Oceanography*, *36*, 1403-1419.

Sobey, R. J., & Thieke, R. J. (1989). Mean flow circulation equations for shoaling and breaking waves. *Journal of Engineering Mechanics*, *115*(2), 285-303.

Stive, M. J. F., & Wind, H. G. (1982). A study of radiation stress and set-up in the nearshore region. *Coastal Engineering*, *6*, 1-25.

Stive, M. J. F., & Wind, H. G. (1986). Cross-shore mean flow in the surf zone. *Coastal Engineering*, *10*, 325-340.

Svendsen, I. A. (1984a). Mass flux and undertow in a surf zone. *Coastal Engineering*, *8*, 347-365.

Svendsen, I. A. (1984b). Wave heights and set-up in a surf zone. *Coastal Engineering*, *8*, 303-329.

Svendsen, I. A. (1987). Analysis of surf zone turbulence. *Journal of Geophysical Research*, *92*(C5), 5115-5124.

Svendsen, I. A. (2006). *Introduction to nearshore hydrodynamics*. Singapore, Singapore: World Scientific Publishing.

Svendsen, I. A., & Lorenz, R. S. (1989). Velocities in combined undertow and longshore currents. *Coastal Engineering*, *13*, 55-79.

Svendsen, I. A., Madsen, P. A., & Buhr Hansen, J. (1978). Wave characteristics in the surf zone. *Proceedings of the 16th International Conference on Coastal Engineering*.

Thornton, E. B., Galvin, J. J., Bub, F. L., & Richardson, D. P. (1976). Kinematics of breaking waves. *Proceedings of 15th Conference on Coastal Engineering*, 461-476.

Ting, F. C. K. (2001). Laboratory study of wave and turbulence velocities in a broad-banded irregular wave surf zone. *Coastal Engineering*, *43*, 183-208.

Ting, F. C. K., & Kirby, J. T. (1994). Observation of undertow and turbulence in a laboratory surf zone. *Coastal Engineering*, *24*, 51-80.

Ting, F. C. K., & Kirby, J. T. (1995). Dynamics of surf-zone turbulence in a strong plunging breaker. *Coastal Engineering*, *24*, 177-204.

Ting, F. C. K., & Kirby, J. T. (1996). Dynamics of surf-zone turbulence in a spilling breaker. *Coastal Engineering*, *27*, 131-160.

Torres-Freyermuth, A., Losada, I. J., & Lara, J. L. (2007). Modeling of surf zone processes on a natural beach using Reynolds-Averaged Navier-Stokes equations. *Journal of Geophysical Research*, *112*, 1-20.

Umeyama, M. (2005). Reynolds stresses and velocity distributions in a wave-current coexisting environment. *Journal of Waterway, Port, Coastal and Ocean Engineering*, *131*, 203-212.

Van der Weerd, A. J. (2012). *Wave-driven dynamics of shoreward propagating accretionary waves in the nearshore*. Enschede, The Netherlands: University of Twente.

Van Rijn, L. C., Tonnon, P. K., & Walstra, D. J. R. (2011). Numerical modelling of erosion and accretion of plane sloping beaches at different scales. *Coastal Engineering*, *58*, 637-355.

Walstra, D. J. R. (2000). *Unibest-TC: Userguide*. Delft, The Netherlands: WL Delft Hydraulics.

Walstra, D. J. R., Roelvink, J. A., & Groeneweg, J. (2000). Calculation of wave-driven currents in a 3D mean flow model. *Proc. of the 27th Coastal Eng. Conf.*, Sydney, Australia.

Wang, J., & Shen, Y. (2010). Modeling oil spills transportation in seas based on unstructured grid, finite-volume, wave-ocean model. *Ocean Modelling*, *35*, 332-344.

Warner, J. C., Sherwood, C. R., Signell, R. P., Harris, C. K., & Arango, H. G. (2008). Development of a three-dimensional, regional, coupled wave, current, and sediment-transport model. *Computers & Geosciences*, *34*, 1284-1306.

Wenneker, I., Van Dongeren, A., Lescinski, J., Roelvink, D., & Borsboom, M. (2011). A Boussinesq-type wave driver for a morphodynamical model to predict short-term morphology. *Coastal Engineering*, *58*, 66-84.

Wilcox, D. C. (1993). *Turbulence modelling for CFD.* La Cañada, California, United States: DCW Industries, Inc.

Xia, H., Xia, Z., & Zhu, L. (2004). Vertical variation in radiation stress and wave-induced current. *Coastal Engineering*, *51*, 309-321.

Yoon, H.-D., & Cox, D. T. (2010). Large-scale laboratory observations of wave breaking turbulence over an evolving beach. *Journal of Geophysical Research*, *115*, 1-16.

Zou, Q., Bowen, A. J., & Hay, A. E. (2006). Vertical distribution of wave shear stress in variable water depth: theory and field observations. *Journal of Geophysical Research*, *111*, 1-17.

List of Tables

List of Figures

Appendix A

Reynolds averaging

In order to describe turbulent flows, the Navier-Stokes equation is wave-averaged to give an approximate solution. The flow is first decomposed into different parts, a process known as Reynolds decomposition, as shown in equation A.1. In which $\overline{u_i}$ is the mean flow; $\tilde{u}_i$ the orbital flow; and u'_i the turbulent flow. The components are decomposed in such a way that by definition the wave-averaged values (represented by an overline) of orbital and turbulent components are zero ($\overline{\tilde{u}_i} = 0$ and $\overline{u'_i} = 0$). Before we start with the calculations, it must be noted that wave-averaging above wave trough level is problematic, since in this area there is water only part of the time (and thus $\overline{\tilde{u}_i} \neq 0$). Therefore, strictly speaking, the equations used here are not valid above wave trough level (Svendsen, 2006). Applying the three-layer concept (section 4.2.3) gives us the ability to define the flow up until the mean water level.

The NS-equation is rewritten into the tensor notation for clarity and completeness (equation A.2).

$$(u_i, p) = (\overline{u_i} + \tilde{u}_i + u'_i, \overline{p} + \tilde{p} + p') \tag{A.1}$$

$$\frac{\partial u_i}{\partial t} + \frac{\partial}{\partial x_j}(u_j u_i) = g_i - \frac{1}{\rho}\frac{\partial p}{\partial x_i} + \nu\left(\frac{\partial^2 u_i}{\partial x_j^2}\right) \quad i, j = 1, 2 \tag{A.2}$$

Subsituting equation A.1 into A.2, and phase-averaging leads to the Reynolds-averaged Navier-Stokes (RANS) equation, noting that $\overline{\frac{\partial u_i}{\partial x}} = \frac{\partial \overline{u_i}}{\partial x}$ for non-fluctuating integral boundaries:

$$\begin{gathered}\frac{\partial \overline{(\overline{u_i} + \tilde{u}_i + u'_i)}}{\partial t} + \frac{\partial}{\partial x_j}\overline{(\overline{u_j} + \tilde{u}_j + u'_j)(\overline{u_i} + \tilde{u}_i + u'_i)} = \\ g_i - \frac{1}{\rho}\frac{\partial \overline{(\overline{p} + \tilde{p} + p')}}{\partial x_i} + \nu\left(\frac{\partial^2 \overline{(\overline{u_i} + \tilde{u}_i + u'_i)}}{\partial x_j^2}\right)\end{gathered} \tag{A.3}$$

Rewriting and removing obsolete parts (because of the definition of the Reynolds decomposition, most terms are zero below mean water level, as explained above) gives:

$$\begin{gathered}\frac{\partial}{\partial t}\left(\overline{\overline{u_i}} + \cancelto{0}{\overline{\tilde{u}_i}} + \cancelto{0}{\overline{u'_i}}\right) + \frac{\partial}{\partial x_j}\Big(\overline{\overline{u_j}\,\overline{u_i}} + \cancelto{0}{\overline{\overline{u_j}\tilde{u}_i}} + \cancelto{0}{\overline{\overline{u_j}u'_i}} + \cancelto{0}{\overline{\tilde{u}_j\overline{u_i}}} + \overline{\tilde{u}_j\tilde{u}_i} + \cancelto{0}{\overline{\tilde{u}_j u'_i}} + \\ \cancelto{0}{\overline{u'_j\overline{u_i}}} + \cancelto{0}{\overline{u'_j\tilde{u}_i}} + \overline{u'_j u'_i}\Big) = g_i - \frac{1}{\rho}\frac{\partial}{\partial x_i}\left(\overline{\overline{p}} + \cancelto{0}{\overline{\tilde{p}}} + \cancelto{0}{\overline{p'}}\right) + \nu\left[\frac{\partial^2}{\partial x_j^2}\left(\overline{\overline{u_i}} + \cancelto{0}{\overline{\tilde{u}_i}} + \cancelto{0}{\overline{u'_i}}\right)\right]\end{gathered} \tag{A.4}$$

$$\frac{\partial \overline{u_i}}{\partial t} + \frac{\partial}{\partial x_j}\left(\overline{u_j u_i} + \overline{\tilde{u}_j \tilde{u}_i} + \overline{u_j' u_i'}\right) = g_i - \frac{1}{\rho}\frac{\partial \overline{p}}{\partial x_i} + \nu\left(\frac{\partial^2 \overline{u_i}}{\partial x_j^2}\right) \tag{A.5}$$

To give a more familiar form of the equations, they are written back into the normal Cartesian notation. This changes equation A.5 into equations A.6a and A.6b:

$$x: \frac{\partial \overline{u}}{\partial t} + \frac{\partial}{\partial x}\left(\overline{u^2} + \overline{\tilde{u}^2} + \overline{u'^2}\right) + \frac{\partial}{\partial z}\left(\cancelto{0}{\overline{w}\overline{u}} + \overline{\tilde{w}\tilde{u}} + \overline{w'u'}\right) = \cancelto{0}{g_x} - \frac{1}{\rho}\frac{\partial \overline{p}}{\partial x} + \nu\left(\frac{\partial^2 \overline{u}}{\partial x^2} + \frac{\partial^2 \overline{u}}{\partial z^2}\right) \tag{A.6a}$$

$$z: \frac{\partial \overline{w}}{\partial t} + \frac{\partial}{\partial x}\left(\cancelto{0}{\overline{w}\overline{u}} + \overline{\tilde{w}\tilde{u}} + \overline{w'u'}\right) + \frac{\partial}{\partial z}\left(\overline{w^2} + \overline{\tilde{w}^2} + \overline{w'^2}\right) = g_z - \frac{1}{\rho}\frac{\partial \overline{p}}{\partial z} + \nu\left(\frac{\partial^2 \overline{w}}{\partial x^2} + \frac{\partial^2 \overline{w}}{\partial z^2}\right) \tag{A.6b}$$

Appendix B

Derivation of radiation stress

We continue with equation 2.3a, of which only the cross-shore, horizontal direction (x) is considered. As in the whole thesis, also here $\frac{\partial}{\partial y}$ is assumed to be zero. Taking the assumption of incompressible flow (equation B.1) and writing the viscosity terms as stresses (equation B.2) for convenience, we get:

$$\frac{\partial u}{\partial x} + \frac{\partial w}{\partial z} = 0 \tag{B.1}$$

$$\tau = \mu \left(\frac{\partial u}{\partial x} + \frac{\partial u}{\partial z} \right) \tag{B.2}$$

$$\frac{\partial}{\partial t}(\rho u) + \frac{\partial}{\partial x}\left(\rho u^2\right) + \frac{\partial}{\partial z}(\rho w u) = -\frac{\partial}{\partial x}(p) + \frac{\partial}{\partial x}(\tau_{xx}) + \frac{\partial}{\partial z}(\tau_{zx}) \tag{B.3}$$

Integrating over depth, where $-h_0$ represents bed level and ζ free surface level, leads to:

$$\begin{aligned} &\overbrace{\int_{-h_0}^{\zeta} \frac{\partial}{\partial t}(\rho u)\,\mathrm{d}z}^{(1)} + \overbrace{\int_{-h_0}^{\zeta} \frac{\partial}{\partial x}\left(\rho u^2\right)\,\mathrm{d}z}^{(2)} + \overbrace{\int_{-h_0}^{\zeta} \frac{\partial}{\partial z}(\rho w u)\,\mathrm{d}z}^{(3)} = \\ &\qquad \underbrace{\int_{-h_0}^{\zeta} \frac{\partial}{\partial x}(-p)\,\mathrm{d}z}_{(4)} + \underbrace{\int_{-h_0}^{\zeta} \frac{\partial}{\partial x}(\tau_{xx})\,\mathrm{d}z}_{(5)} + \underbrace{\int_{-h_0}^{\zeta} \frac{\partial}{\partial z}(\tau_{zx})\,\mathrm{d}z}_{(6)} \end{aligned} \tag{B.4}$$

To make calculations easier, we would like to take the derivative after the whole water column has been vertically integrated. For this, the Leibniz rule is applied. In this context, the Leibniz rule is applied as in equation B.5. The Leibniz rule is applied on terms (1), (2), (4) and (5), terms (3) and (6) are simply integrated.

$$\int_{-h_0}^{\zeta} \frac{\partial f(x,z)}{\partial x}\,\mathrm{d}z = \frac{\partial}{\partial x}\int_{-h_0}^{\zeta} f(x,z)\,\mathrm{d}z - \left[f(x,\zeta)\frac{\partial \zeta}{\partial x}\right]_{\zeta} - \left[f(x,-h_0)\frac{\partial h_0}{\partial x}\right]_{-h_0} \tag{B.5}$$

For sake of clarity, the different terms are shown separately:

$$
\begin{aligned}
(1) =& \rho\frac{\partial}{\partial t}\int_{-h_0}^{\zeta} u \,\mathrm{d}z - \left[\rho u \frac{\partial \zeta}{\partial t}\right]_{\zeta} - \left[\rho u \frac{\partial h_0}{\partial t}\right]_{-h_0} && \text{(B.6a)}\\
(2) =& \frac{\partial}{\partial x}\int_{-h_0}^{\zeta} \left(\rho u^2\right) \mathrm{d}z - \left[\rho u^2 \frac{\partial \zeta}{\partial x}\right]_{\zeta} - \left[\rho u^2 \frac{\partial h_0}{\partial x}\right]_{-h_0} && \text{(B.6b)}\\
(3) =& \rho\left[wu\right]_{\zeta} - \rho\left[wu\right]_{-h_0} && \text{(B.6c)}\\
(4) =& \frac{\partial}{\partial x}\int_{-h_0}^{\zeta} (-p) \,\mathrm{d}z - \left[(-p) \frac{\partial \zeta}{\partial x}\right]_{\zeta} - \left[(-p) \frac{\partial h_0}{\partial x}\right]_{-h_0} && \text{(B.6d)}\\
(5) =& \frac{\partial}{\partial x}\int_{-h_0}^{\zeta} (\tau_{xx}) \,\mathrm{d}z - \left[\tau_{xx} \frac{\partial \zeta}{\partial x}\right]_{\zeta} - \left[\tau_{xx} \frac{\partial h_0}{\partial x}\right]_{-h_0} && \text{(B.6e)}\\
(6) =& \left[\tau_{zx}\right]_{\zeta} - \left[\tau_{zx}\right]_{-h_0} && \text{(B.6f)}
\end{aligned}
$$

Applying the kinematic boundary conditions as shown in equations B.7 and B.8, term (3) changes to (equation B.9):

$$
w_{\zeta} = \frac{\partial \zeta}{\partial t} + u\frac{\partial \zeta}{\partial x} \tag{B.7}
$$

$$
w_{-h_0} = -u\frac{\partial h_0}{\partial x} \tag{B.8}
$$

$$
(3) = \rho u_{\zeta}\frac{\partial \zeta}{\partial t} + \rho u_{\zeta}^2\frac{\partial \zeta}{\partial x} + \rho u_{-h_0}^2\frac{\partial h_0}{\partial x} \tag{B.9}
$$

Now, it can be seen that term (3) cancels out parts of terms (1) and (2) (grayed-out parts in equation B.10). Next, we take the atmospheric pressure at 0 (we assume it does not change, so it does not affect the momentum equation) and move the pressure integral to the LHS, resulting in:

$$
\begin{gathered}
\rho\frac{\partial}{\partial t}\int_{-h_0}^{\zeta} u \,\mathrm{d}z - \left[\rho u \frac{\partial \zeta}{\partial t}\right]_{\zeta} - \left[\rho u \frac{\partial h_0}{\partial t}\right]_{-h_0} + \frac{\partial}{\partial x}\int_{-h_0}^{\zeta} \left(\rho u^2 + p\right) \mathrm{d}z - \\
\left[\rho u^2 \frac{\partial \zeta}{\partial x}\right]_{\zeta} - \left[\rho u^2 \frac{\partial h_0}{\partial x}\right]_{-h_0} + \rho u_{\zeta}\frac{\partial \zeta}{\partial t} + \rho u_{\zeta}^2\frac{\partial \zeta}{\partial x} + \rho u_{-h_0}^2\frac{\partial h_0}{\partial x} = \\
- \cancelto{0}{\left[(-p) \frac{\partial \zeta}{\partial x}\right]_{\zeta}} - \left[(-p) \frac{\partial h_0}{\partial x}\right]_{-h_0} + \\
\frac{\partial}{\partial x}\int_{-h_0}^{\zeta} (\tau_{xx}) \,\mathrm{d}z - \left[\tau_{xx} \frac{\partial \zeta}{\partial x}\right]_{\zeta} - \left[\tau_{xx} \frac{\partial h_0}{\partial x}\right]_{-h_0} + \left[\tau_{zx}\right]_{\zeta} - \left[\tau_{zx}\right]_{-h_0}
\end{gathered} \tag{B.10}
$$

The bottom and free surface terms on the RHS are combined after Svendsen (2006) (equations B.11 and B.12):

$$
R_x^s|\nabla F| = \left[(-p) \frac{\partial \zeta}{\partial x}\right]_{\zeta} + \left[\tau_{zx}\right]_{\zeta} - \left[\tau_{xx} \frac{\partial \zeta}{\partial x}\right]_{\zeta} \tag{B.11}
$$

$$
-R_x^B|\nabla B| = -\left[\tau_{zx}\right]_{-h_0} - \left[\tau_{xx} \frac{\partial h_0}{\partial x}\right]_{-h_0} \tag{B.12}
$$

where $|\nabla F| = \sqrt{1+\left(\frac{\partial \zeta}{\partial x}\right)^2}$ and $|\nabla B| = \sqrt{1+\frac{\partial h}{\partial x}}$. Next, we assume a mild slope so hydrostatic pressure at the bottom can be assumed $(\overline{p(-h_0)} = \rho g(\zeta + h_0))$ and $|\nabla B|$ to be 1, and the only bottom shear stress to be the bed shear stress, so we can write $-R_x^B|\nabla B| = -\tau_{b,x}$.

$$\begin{aligned} \rho\frac{\partial}{\partial t}\int_{-h_0}^{\zeta} u\,\mathrm{d}z - \left[\rho u(t,-h_0)\frac{\partial h}{\partial t}\right]_{-h_0} + \frac{\partial}{\partial x}\int_{-h_0}^{\zeta}\left(\rho u^2 + p\right)\,\mathrm{d}z = \\ \left[\rho g(\zeta + h_0)\frac{\partial h_0}{\partial x}\right]_{-h_0} + \frac{\partial}{\partial x}\int_{-h_0}^{\zeta}(\tau_{xx})\,\mathrm{d}z + R_x^s|\nabla F| - \tau_{b,x} \end{aligned} \tag{B.13}$$

Taking the time-averaged value, noting that $\overline{|\nabla F|} = 1$:

$$\rho\frac{\partial \overline{Q_x}}{\partial t} + \frac{\partial}{\partial x}\overline{\int_{-h_0}^{\zeta}(\rho u^2 + p)\,\mathrm{d}z} = \overline{\rho g(\zeta + h_0)\frac{\partial h_0}{\partial x}} + \frac{\partial}{\partial x}\overline{\int_{-h_0}^{\zeta}(\tau_{xx})\,\mathrm{d}z} + \overline{R_x^s} - \overline{\tau_{b,x}} \tag{B.14}$$

where Q is the volume flux. Since density is constant, the conservation of mass is equivalent to conservation of volume and thus it is possible to write $Q = \int_{-h_0}^{\zeta} u\,\mathrm{d}z$ Svendsen (2006). The first term on the RHS is rewritten as; with $h = h_0 + \overline{\zeta}$:

$$\begin{aligned} \rho g(\overline{\zeta} + h_0)\frac{\partial h_0}{\partial x} + \rho g h\frac{\partial \overline{\zeta}}{\partial x} - \rho g h\frac{\partial \overline{\zeta}}{\partial x} = \rho g h\frac{\partial h}{\partial x} - \rho g h\frac{\partial \overline{\zeta}}{\partial x} = \\ \frac{\partial}{\partial x}\left(\frac{1}{2}\rho g h^2\right) - \rho g h\frac{\partial \overline{\zeta}}{\partial x} \end{aligned} \tag{B.15}$$

Substituting equation B.15 into B.14, we get:

$$\rho\frac{\partial \overline{Q_x}}{\partial t} + \frac{\partial}{\partial x}\overline{\int_{-h_0}^{\zeta}(\rho u^2 + p)\,\mathrm{d}z} - \frac{\partial}{\partial x}\left(\frac{1}{2}\rho g h^2\right) = -\rho g h\frac{\partial \overline{\zeta}}{\partial x} + \frac{\partial}{\partial x}\overline{\int_{-h_0}^{\zeta}(\tau_{xx})\,\mathrm{d}z} + \overline{R_x^s} - \overline{\tau_{b,x}} \tag{B.16}$$

Just as in Svendsen (2006), it is noted that the basic equation as presented in equation B.3, is already turbulence averaged. Therefore, the flow is only divided into a mean-flow and fluctuating wave component. This leads to the following result:

$$\overline{\int_{-h_0}^{\zeta} u^2\,\mathrm{d}z} = \overline{\int_{-h_0}^{\zeta}(\overline{u} + \tilde{u})^2\,\mathrm{d}z} = \int_{-h_0}^{\overline{\zeta}}\left(\overline{u}^2\right)\,\mathrm{d}z + \overline{\int_{-h_0}^{\zeta}(\tilde{u}^2)\,\mathrm{d}z} + \overline{\int_{-h_0}^{\zeta} 2\left(\overline{u}\tilde{u}\right)\,\mathrm{d}z} \tag{B.17}$$

Substituting equation B.17 into B.16, rearranging some terms and noting that the time-averaged orbital velocity below wave trough is zero, results in:

$$\begin{aligned} \rho\frac{\partial \overline{Q_x}}{\partial t} + \rho\frac{\partial}{\partial x}\int_{-h_0}^{\overline{\zeta}}(\overline{u}^2)\,\mathrm{d}z + \rho\frac{\partial}{\partial x}\overline{\int_{-h_0}^{\zeta}(\tilde{u}^2 + p)\,\mathrm{d}z} - \frac{\partial}{\partial x}\left(\frac{1}{2}\rho g h^2\right) + \rho\overline{\int_{\zeta_t}^{\zeta}(2\overline{u}\tilde{u})\,\mathrm{d}z} = \\ -\rho g h\frac{\partial \overline{\zeta}}{\partial x} + \frac{\partial}{\partial x}\overline{\int_{-h_0}^{\zeta}(\tau_{xx})\,\mathrm{d}z} + \overline{R_x^s} - \overline{\tau_{b,x}} \end{aligned} \tag{B.18}$$

Now defining radiation stress as:

$$S_{xx} = \overline{\int_{-h_0}^{\zeta} (\rho \tilde{u}^2 + p) \, \mathrm{d}z} - \frac{1}{2}\rho g h^2 \tag{B.19}$$

The momentum equation can now be written as:

$$\begin{aligned}\overbrace{\rho \frac{\partial \overline{Q_x}}{\partial t}}^{(I)} + \overbrace{\rho \frac{\partial}{\partial x} \left(\int_{-h_0}^{\overline{\zeta}} (\overline{u}^2) \, \mathrm{d}z \right)}^{(II)} + \overbrace{\frac{\partial S_{xx}}{\partial x}}^{(III)} - \overbrace{\frac{\partial}{\partial x} \overline{\int_{-h_0}^{\zeta} (\tau_{xx}) \, \mathrm{d}z}}^{(IV)} + \overbrace{\rho \frac{\partial}{\partial x} \overline{\int_{\zeta_t}^{\zeta} (2\overline{u}\tilde{u}) \, \mathrm{d}z}}^{(V)} = \\ \underbrace{-\rho g h \frac{\partial \overline{\zeta}}{\partial x}}_{(VI)} + \underbrace{\overline{R_x^s}}_{(VII)} - \underbrace{\overline{\tau_{b,x}}}_{(VIII)}\end{aligned} \tag{B.20}$$

where term (I) and (II) stand for the acceleration of the time varying current with (I) expressing the time rate of change of momentum; and (II) expressing the gradient of the momentum flux. Term (III) is the gradient of radiation stress (known as wave force), which represents the wave effects on the momentum flux. Term (IV) is what Svendsen (2006) calls turbulent radiation stress, similar to (wave) radiation stress but now due to turbulent fluctuations. Term (V) is the convective acceleration associated with the net mass flux in the wave. Term (VI) represents the effects due to wave setup; term (VII) the stresses occurring at the free water surface, which we will collectively name free surface stress; and term (VIII) stresses occurring at the bottom, which was simplified into the bed shear stress.

Appendix C

Accuracy of data

As discussed in section 3.2, the amount of wave series used to determine the different velocity components was rather small. This could possibly negatively influence the accuracy of the data. In order to check if this poses a problem, the velocity components were determined with varying amounts of wave series. A highly fluctuating result, would lead to the conclusion that the accuracy of Boers (2005) data is poor. If the results are stable – so there are no large differences between the results of the amount of wave series – we assume the accuracy is good and the small amount of wave series does not significantly affect the results.

The data used in this thesis are those extracted by Boers (2005). However, in this analysis the data is recalculated from the raw data files; and because not everything could be reproduced, the procedure is less elaborate than carried out by Boers (2005). Boers (2005) also used filters which we were not able to use, because we lacked the proper programs. This mostly affects the turbulent velocities, for the mean and orbital this should not be a problem. The accuracy of the mean, orbital, and turbulent velocities are considered separately, where turbulent velocities are represented by turbulent kinetic energy. In figure C.1 the results are shown for three different locations to see if location affects the accuracy of the data.

The mean-flow velocity shows only small deviations from the values as determined by Boers (2005). 10 wave series give a better approximation than 5, but deviations are very small and therefore considered negligible. Orbital velocity shows slightly larger deviations, but these are still very small. At $x = 23.95$ m around $\xi = 0.3$, a large deviation can be seen, but this is considered to be an outlier that was filtered out by Boers (2005). For turbulent kinetic energy, large deviations can be seen. Results found by Boers (2005) are different because of filtering, which could not reproduced here. Differences between 5 and 10 wave series are also found near the breaker bar, where heavy breaking occurs. Results at $x = 8.10$ m are good. All in all, we can conclude that the accuracy of mean and orbital velocities is good; and turbulent velocities should be considered with care. Although the results for Boers (2005) do not show unexpected behaviours.

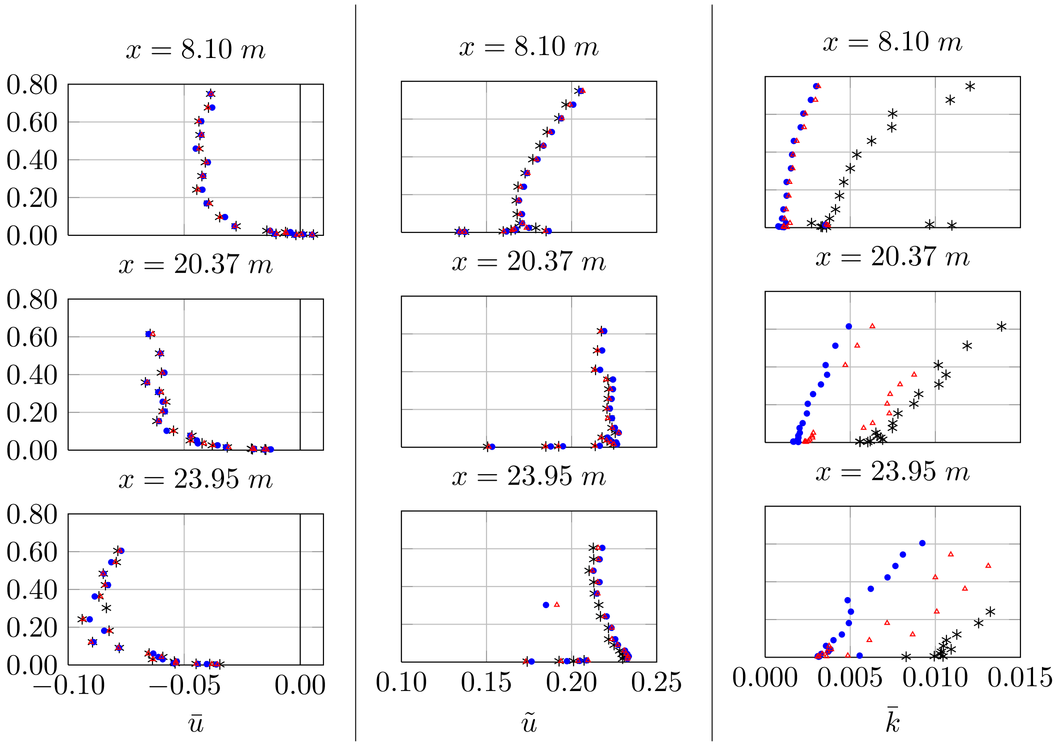

Figure C.1: *Comparison between derived velocities for 5 wave series (•); 10 wave series (▵); and the results as extracted by Boers (2005) (∗) for Boers-1B.*

Appendix D

Additional figures

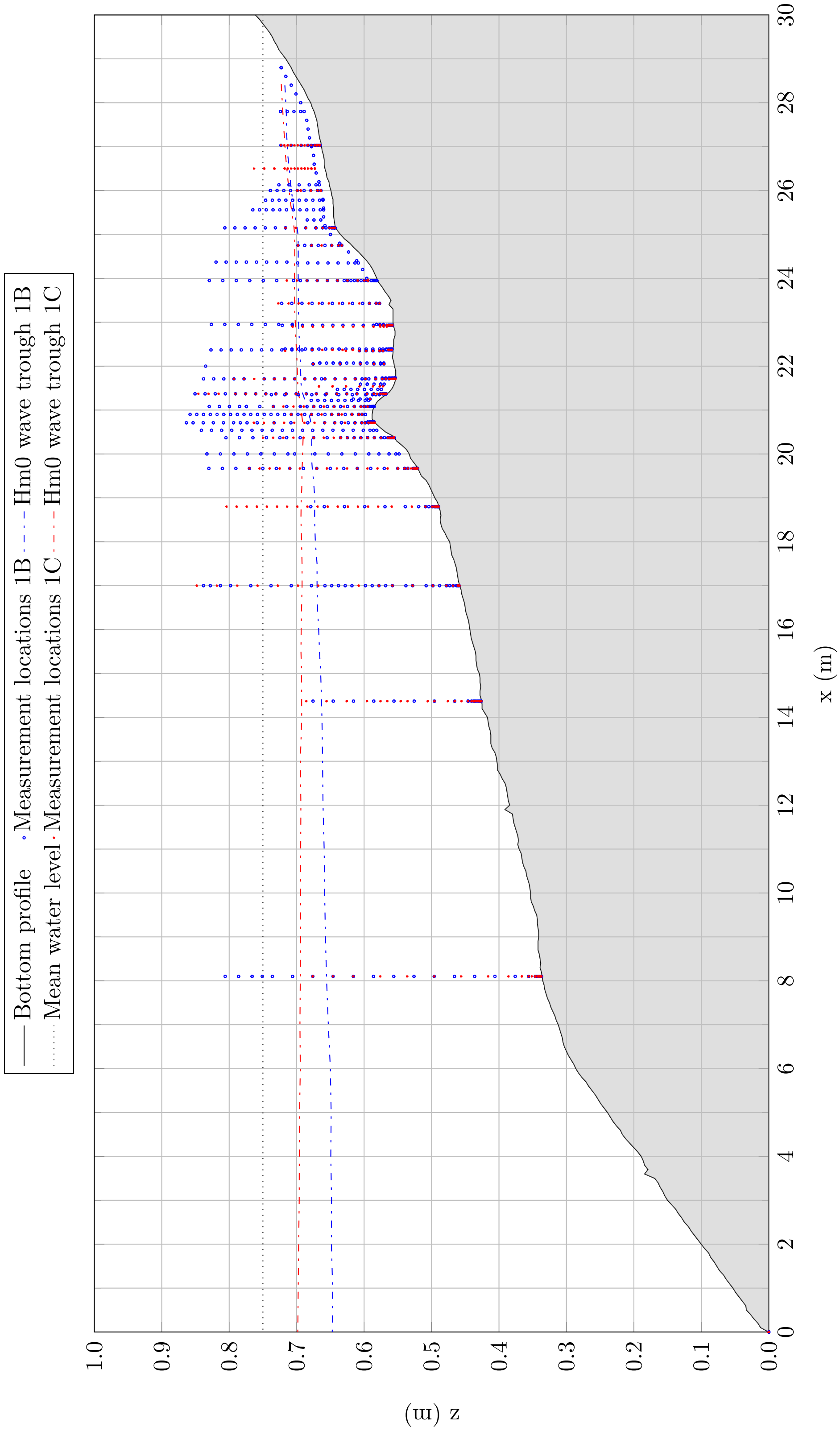

Figure D.1: *Locations of laser-Doppler velocimeters*

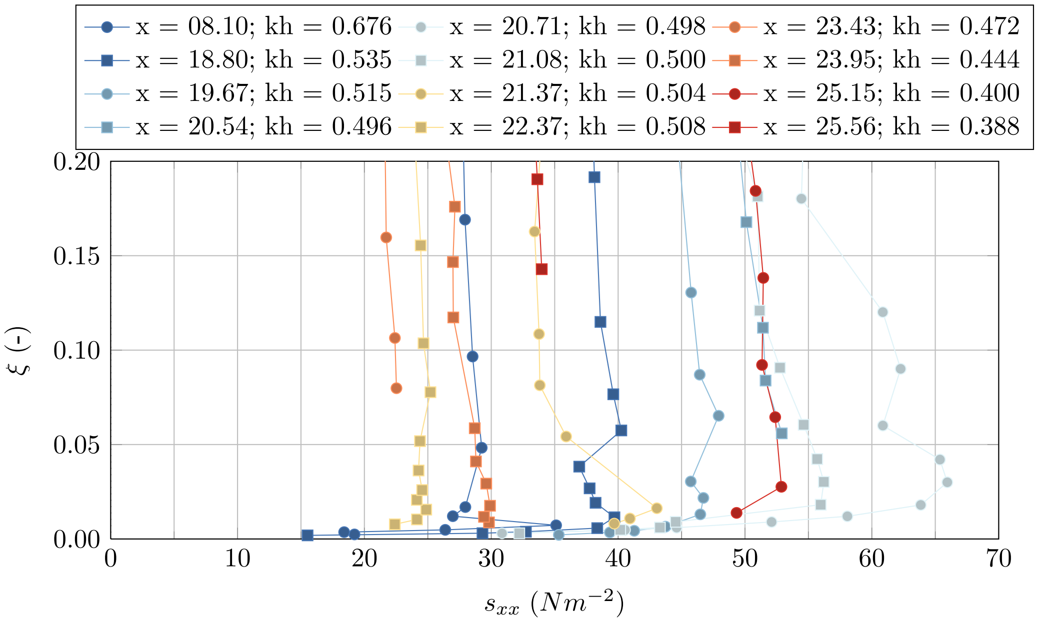

Figure D.2: *Vertical radiation stress profiles in the bottom boundary layer for Boers-1B*

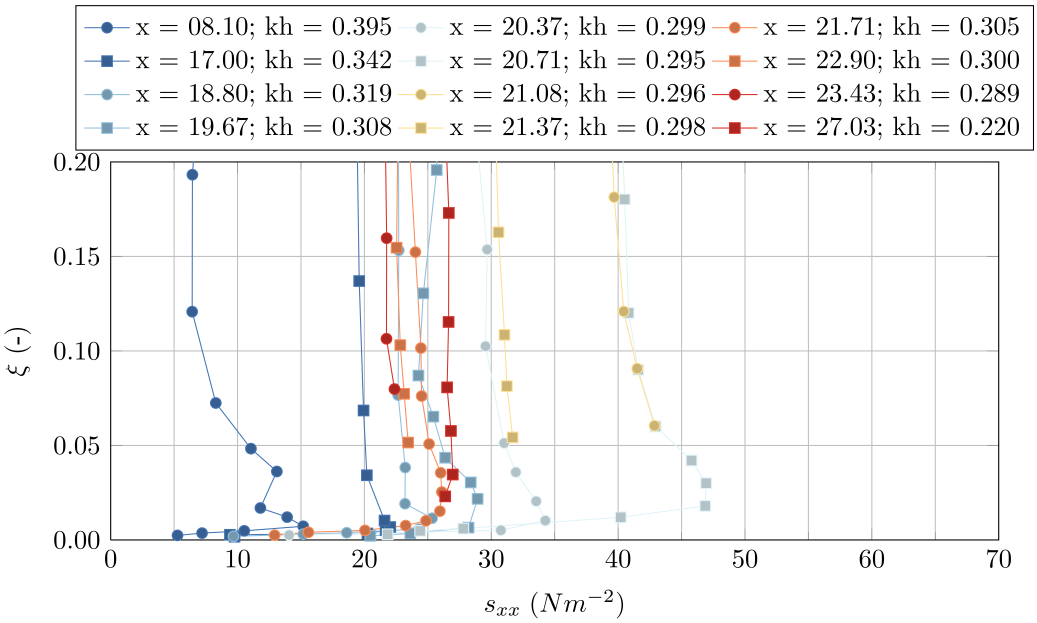

Figure D.3: *Vertical radiation stress profiles in the bottom boundary layer for Boers-1C*

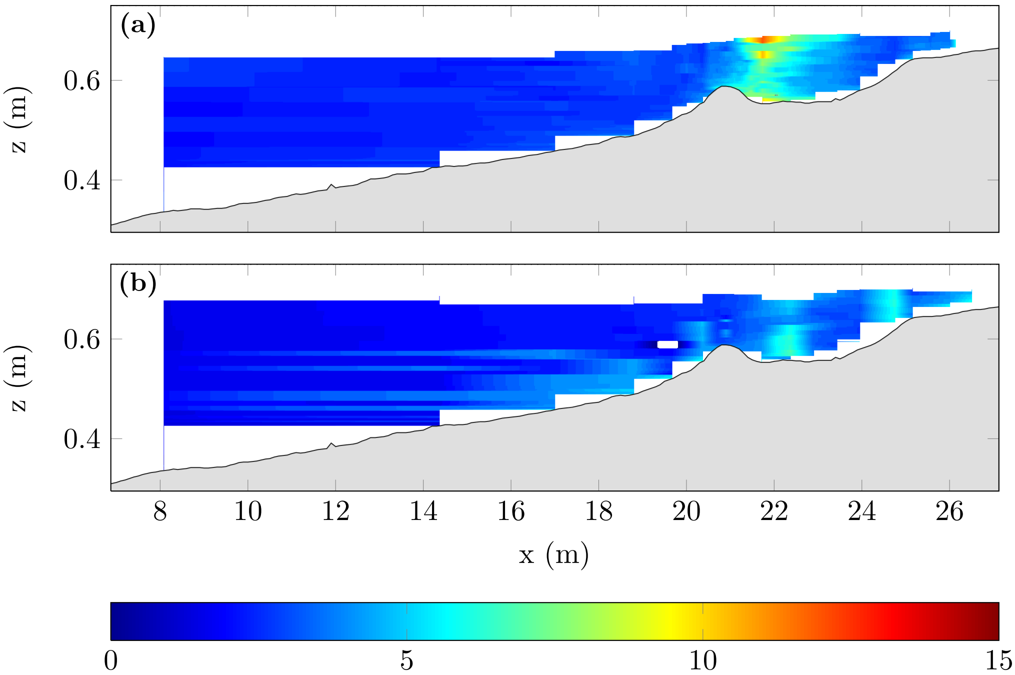

Figure D.4: *Relative size of turbulence part to wave part for both B and C*

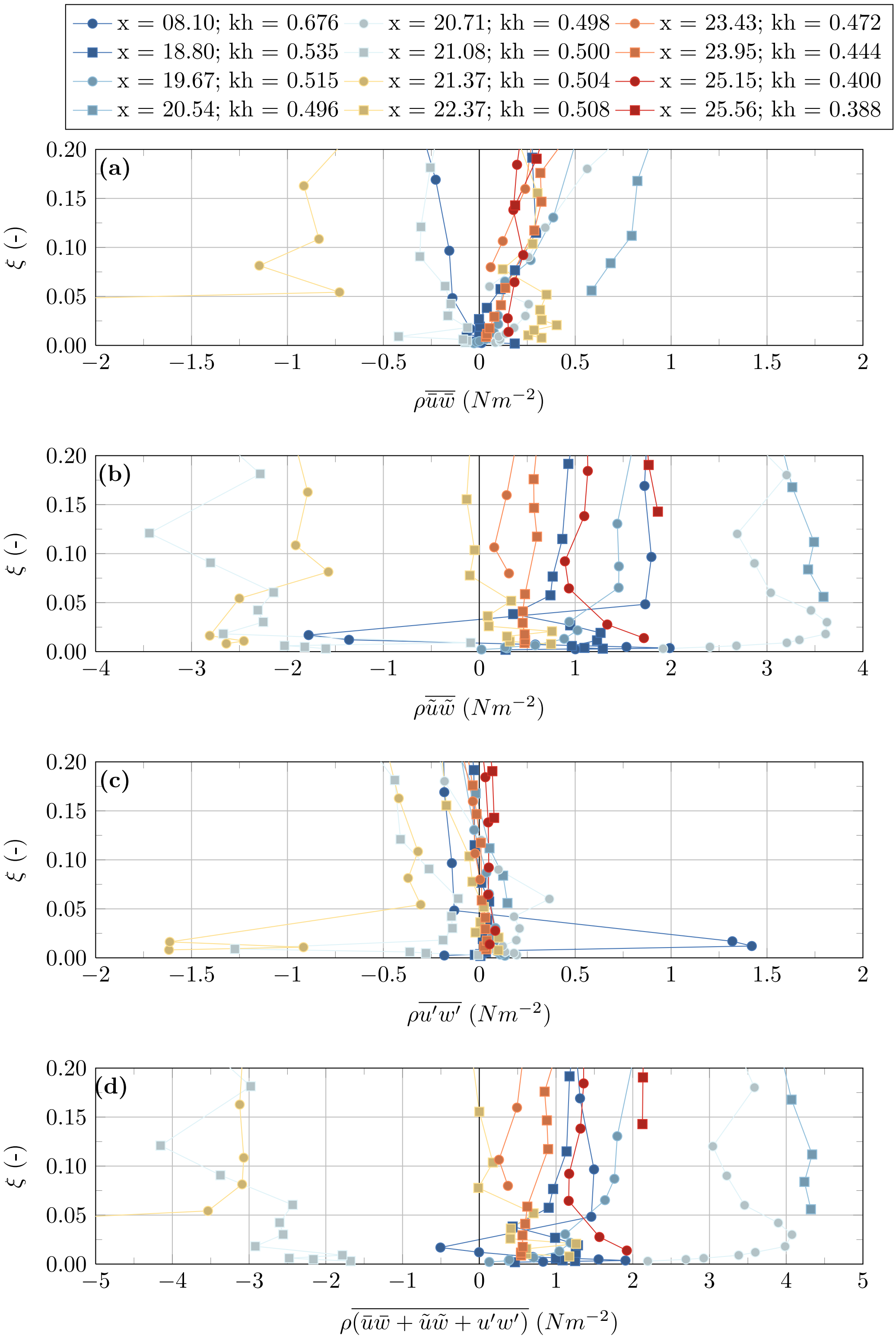

Figure D.5: *Vertical fluxes of horizontal momentum in the bottom boundary layer by (a) $\rho\overline{\bar{u}\bar{w}}$, (b) $\rho\overline{\tilde{u}\tilde{w}}$, (c) $\rho\overline{u'w'}$, (d) sum of previous three components for Boers-1B*

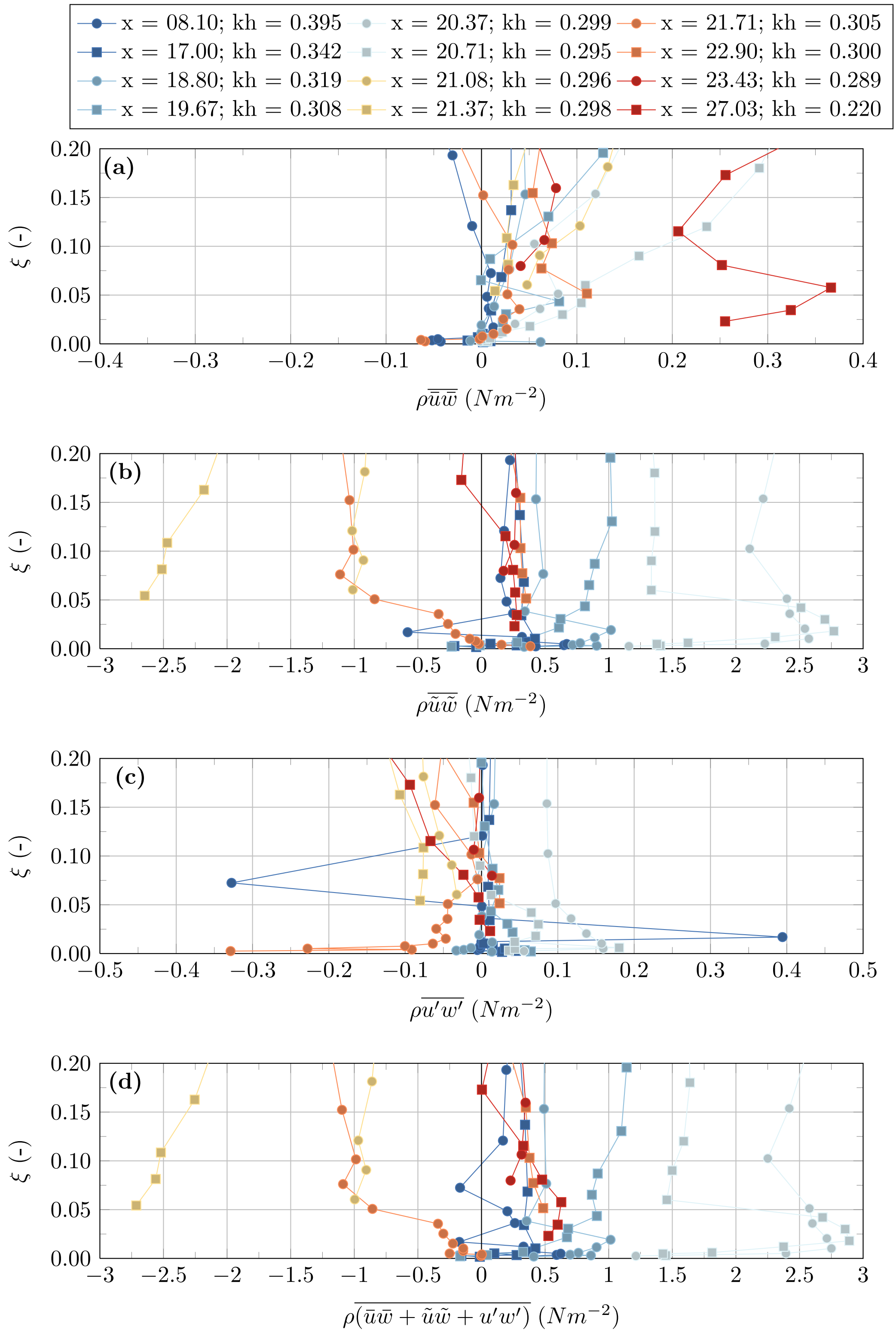

Figure D.6: *Vertical fluxes of horizontal momentum in the bottom boundary layer by (a) $\rho\overline{\bar{u}\bar{w}}$, (b) $\rho\overline{\tilde{u}\tilde{w}}$, (c) $\rho\overline{u'w'}$, (d) sum of previous three components for Boers-1C*

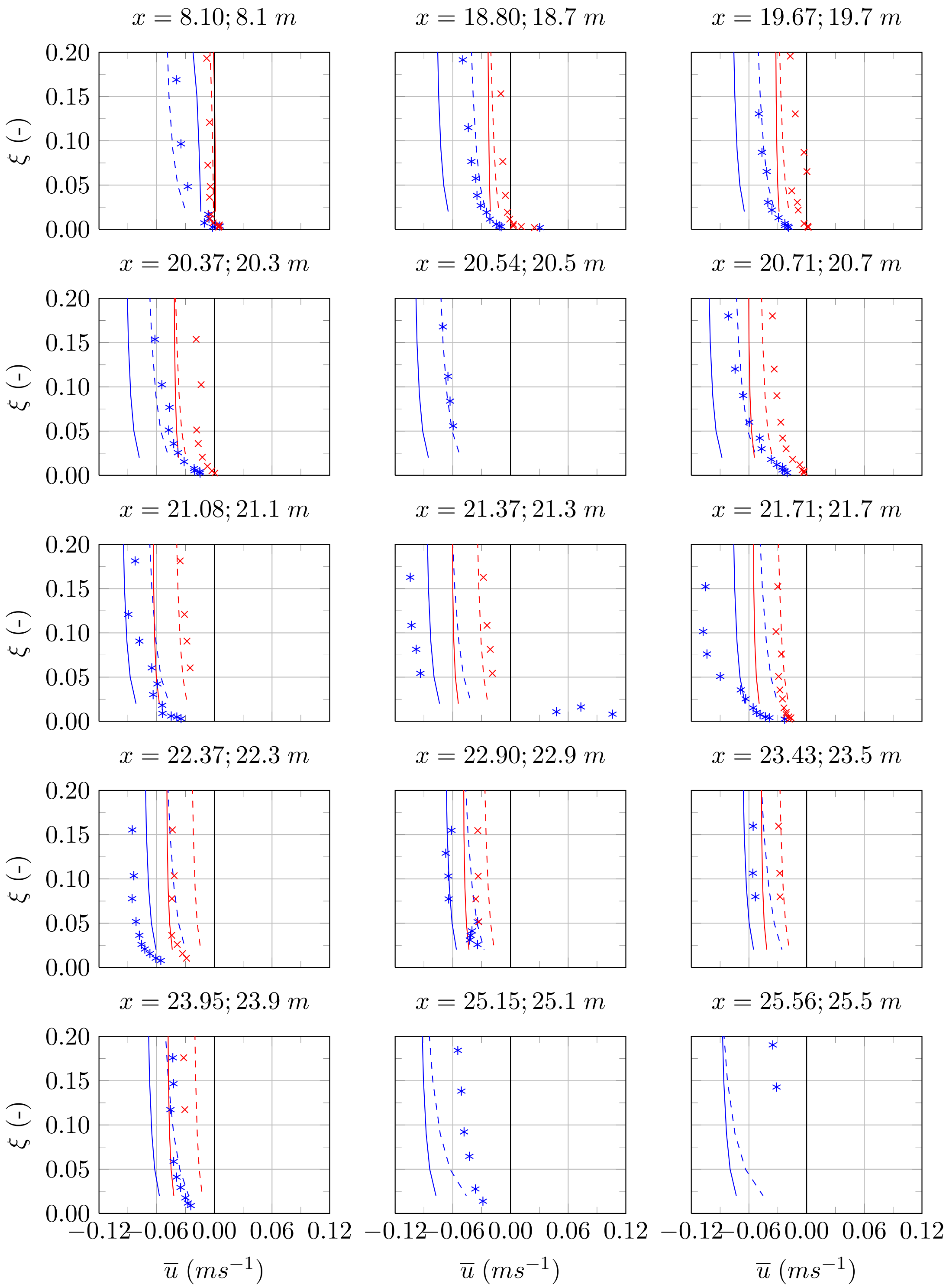

Figure D.7: *Comparison of measured undertow in the bottom boundary layer for Boers-1B (∗) and Boers-1C (×); calculated undertow by Roller-FLOW for Boers-1B (——) and Boers-1C (——); and TRITON-FLOW for Boers-1B (- - -) and Boers-1C (- - -). The first x-value in the title is from the measurements and the second from the location of the observation point in Delft3D-FLOW.*